SCUOLA
NORMALE
SUPERIORE

Faculty of Science
Course in Nanoscience
XXXIII cycle

Structural insights into human NAPE-PLD interactions

FIS/07

Candidate
Sara Chiarugi

Advisor
Dr. Gianpiero Garau

Supervisor
Prof. Gian Michele Ratto

2023/2024

Table of Contents

Foreword

This thesis is the result of my research activity carried out at NEST laboratory of the Scuola Normale Superiore in Pisa. I started my studies on the membrane-associated protein NAPE-PLD in 2018, in line with my interest in structural biology and the research endeavours of the Biostructures Lab of Gianpiero Garau I joined. This research was performed within a joint PhD program sponsored by Scuola Normale Superiore and Istituto Italiano di Tecnologia.

Abstract

The membrane-associated enzyme NAPE-PLD (N-acyl phosphatidylethanolamine specific-phospholipase D) generates the endogenous cannabinoid arachidonylethanolamide (anandamide) and other lipid signalling amides that play key roles in several physiological pathways, including appetite, lifespan, stress, and pain response. Earlier, our structural and biophysical studies showed that the interaction between the dimeric protein and bile acid cofactors turns the enzyme on. This discovery casted an interesting light on NAPE-PLD as a point where lipid amide signalling, and bile acid physiology converge. In the last years, the therapeutic potential of NAPE-PLD has come to light in the field of emotional behaviour, neurodegenerative and metabolic diseases, paving the way for the development of specific small molecule ligands. However, due to the delicate behaviour of this membrane target and its challenging crystallization process, no structure in complex with specific small molecules have been reported so far, making the process of ligand discovery extremely difficult.

Using the label-free technique of surface plasmon resonance, here we report the discovery of different classes of novel ligands that bind NAPE-PLD in the low micromolar range. We successfully managed to determine the first crystal structures of NAPE-PLD in complex with these molecules, providing useful insights into its function and modulation. Importantly, we first detected and validated by X-ray diffraction the interaction of the membrane target with the compound pyridoxal-5'-phosphate (PLP), which is the active form of vitamin B6, involved in the cellular metabolism of amino acids and lipids, as well as in the biosynthesis of neurotransmitters. In addition, we have successfully determined the structure of NAPE-PLD in complex with the thiazide diuretic hydrochlorothiazide (HCTZ), a drug that has been used for more than half a century to treat hypertension. Finally, we determined the complex structure with the compound naphthalenetrisulfonic acid. Our results characterize at atomic level the binding mode of these ligands and suggest the potential involvement of NAPE-PLD in the control of hypertension.

Abbreviations

2-AG	2-arachidonoyl-glycerol
ABHD4	α/β-hydrolase domain-containing protein 4
AEA	N-arachidonoylethanolamine
BA	Bile acid
CB1	Cannabinoid receptor of type-1
CB2	Cannabinoid receptor of type-2
CNS	Central nervous system
Cryo-EM	Cryo-Electron Microscopy
DAG	Diacylglycerol
DAGL	Diacylglycerol lipase
DCA	Sodium deoxycholate
DHEA	N-docosahexaenoylethanolamine
eCB	Endothelial cannabinoid receptor
ECS	Endocannabinoid system
FAAH	Fatty acid amide hydrolase
FPLC	Fast protein liquid chromatography
G3P	Glycerol-3-phosphate
GABA	γ-Aminobutyric acid
GDE	Glycerophosphodiesterase
GFSEC	Gel filtration size exclusion chromatography
GPCR	G protein-coupled receptor
GP-NAE	Glycerophospho-*N*-acylethanolamine
HCTZ	Hydrochlorothiazide

IPTG	Isopropyl β-D-1-thiogalactopyranoside
ITC	Isothermal titration calorimetry
LB	Luria Broth
LE	Ligand efficiency
LEA	N-linoleoylethanolamine
LPA	Lysophosphatidic acid
MAGL	Monoacylglycerol lipase
MBP	Maltose-binding protein
MCK	Multi-cycle kinetic method
MS	Mass spectrometry
MβLs	Metallo-β-lactamases
N3SA	Naphthalenetrisulfonic acid
NAAA	N-acylethanolamine-hydrolyzing acid amidase
NAEs	N-acylethanolamines
NAPE-PLD	N-acylphosphatidylethanolamine-hydrolyzing phospholipase D
NAPEs	N-acylphosphatidylethanolamines
NMR	Nuclear magnetic resonance
OEA	N-oleoylethanolamine
PA	Phosphatidic acid
PDB	Protein Data Bank
PE	Phosphatidylethanolamine
PEA	N-palmitoylethanolamine
PLAAT1-5	Phospholipase/acyltransferase 1-5
PLC	Phospholipase C
PLD	Phospholipase D

PLP	Pyridoxal-5'-phosphate
pNAE	Phospho-*N*-acylethanolamine
PPAR-α	Peroxisome proliferator-activated receptor-α
PTPN22	Protein tyrosine phosphatase non receptor type 22
RU	Resonance Unit
SEA	N-stearoylethanolamine
SHIP1	Phosphatidylinositol 3,4,5-trisphosphate 5-phosphatase 1
SPR	Surface plasmon resonance
TIR	Total internal reflection
TRPV	Transient receptor potential vanilloid channel
XRD	X-ray diffraction

Chapter 1

Introduction

1.1 Lipid signalling and the NAE family

Lipids are a diverse and ubiquitous group of compounds, which have many key biological functions, such as acting as structural components of cell membranes, serving as energy storage sources, and participating in many signalling pathways. Bioactive lipids regulate many cell functions and often exert their activities through activation of various proteins, such as G protein-coupled receptors (GPCRs), ion channel and nuclear receptor (Chiurchiù and Maccarrone, 2016). Based on the LIPID MAPS classification system, lipids have been divided into eight categories: fatty acyls, glycerolipids, glycerophospholipids, sphingolipids, sterol lipids, prenol lipids saccharolipids and polyketides (Fahy et al., 2005). Among the group of fatty acyls, the N-acylethanolamines (NAEs) are a class of naturally occurring lipid molecules with a plethora of biological activities and protective roles in inflammation, appetite, fertility, neurotransmission, stress and anxiety (Mock et al., 2023). These amides have long-chain fatty acyl (C12–C22, with 0 to 6 double bonds) joined with ethanolamine (figure 1.1). Among different bioactive NAEs, N-palmitoylethanolamine (PEA, C16:0), N-oleoylethanolamine (OEA, C18:1), N-stearoylethanolamine (SEA, C18:0), N-arachidonoylethanolamine (AEA, C20:4), N-linoleoylethanolamine (LEA, 18:2), and N-docosahexaenoylethanolamine (DHEA, 22:6), are present in a variety of organisms including animals and plants.

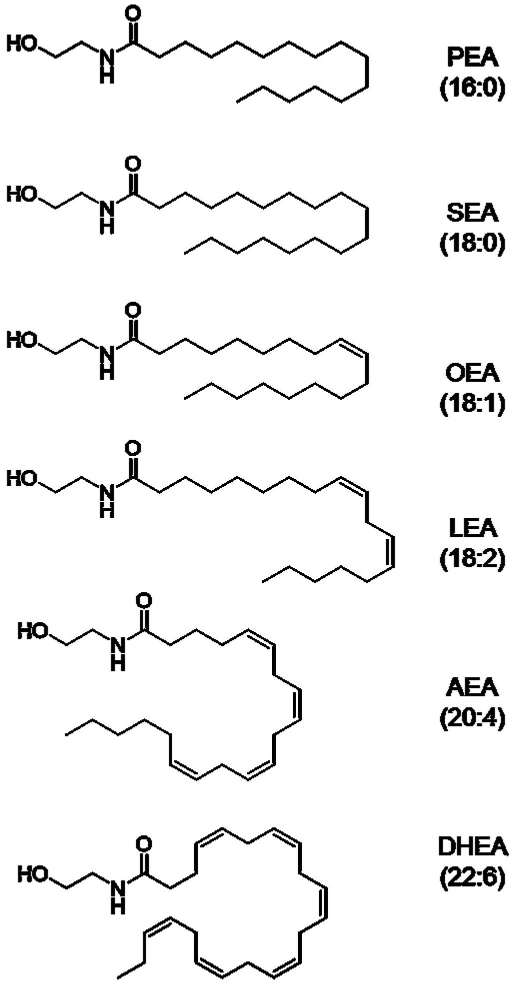

Figure 1.1 Chemical structures of N-acylethanolamines. Chemical structures of N-acylethanolamines. Abbreviations: PEA, N-palmitoylthanolamine; SEA, N-stearoylethanolamine; OEA, N-oleoylethanolamine; LEA, N-linoleoylethanolamine; AEA, N-arachidonoylethanolamine; DHEA, N-docosahexaenoylethanolamine.

PEA, OEA, SEA and LEA are quantitatively major NAEs in animal tissues. Usually AEA is a minor component in comparison with the others NAEs (Ueda et al., 2010). PEA binds to the nuclear receptor peroxisome proliferator-activated receptor-α (PPAR-α, Lo Verme et al., 2005), mediating anti-inflammatory (Didier et al., 2002), analgesic (Gabrielsson et al., 2016), anorexic (de Fonseca et al., 2001), anti-epileptic (Lambert et al., 2002) and neuroprotective (Hansen et al., 2010) actions. OEA shows analgesic and anti-inflammatory effects (Suardiàz et al., 2007), anorectic action, enhances fatty acid absorption in small intestine and stimulates lipolysis through PPAR-α (Fu et al., 2003). OEA also exerts neuroprotective actions (Gonzalez-Aparicio et al., 2014). SEA was reported to be pro-apoptotic (Maccarrone et al., 2002), anti-inflammatory (Dalle Carbonare et al., 2008) and anorectic (Terrazzino et al., 2004). Extensively studied among NAEs, AEA–is an endogenous agonist of the cannabinoid receptors CB_1 and CB_2 (Devane et al., 1992; Maccarrone et al., 2015), known to induce analgesia (Calignano et al., 1998; Cravatt et al., 2001), neuroprotection (Marsicano et al., 2003; Pacher et al., 2006), antianxiety (Kathuria et al., 2002), hypotension (Bàtkai et al., 2004) and stimulate appetite (Williams and Kirkham, 1999). AEA also exerts protective effects on neurotransmission, memory formation and fertility (Katona and Freund, 2012; Iannotti et al., 2016; Correa et al., 2016). Furthermore, LEA exerts anorectic and neuroprotective effects (Diep et al., 2011; Garg et al., 2011), DHEA promotes neurogenesis and synaptogenesis (Kim and Spector, 2018). The NAEs are mainly synthesized 'on demand' from precursor membrane lipids and usually have a short half-life (seconds to minutes). Specific enzymes modulate their levels in tissues (Ueda et al., 2010; Tsuboi et al., 2013).

1.1.1 NAE biosynthesis and degradation

In animal tissues, NAEs are mainly synthetized from membrane glycerophospholipids in response to cellular stimuli, stored inside the cell, and degraded by hydrolysis to free fatty acids and ethanolamine (Iannotti et al., 2016). The enzymes responsible for the formation and degradation of

NAEs play crucial roles in the tight regulation of bioactive lipids levels. In 1990, Schmid and co-workers confirmed “the transacylation-phosphodiesterase pathway” as the principal biosynthetic route of NAEs. In mammalian tissues, this biosynthetic route starts from glycerophospholipids following two enzyme reactions (Schmid et al., 1990; Hussain et al., 2017) (figure 1.2). The first step is the N-acylation of ethanolamine phospholipids by a Ca^{2+}-dependent *N*-acyltransferase, which produces N-acylphosphatidylethanolamines (NAPEs). The second step is the release of NAEs from NAPEs by a specific N-acylphosphatidylethanolamine-hydrolyzing phospholipase D (NAPE-PLD). Ensuing studies also revealed the possible presence of other indirect and multi-steps pathways for the formation of NAEs, independent from NAPE-PLD (Leung et al., 2006; Liu et al., 2008; Simon and Cravatt, 2010; Tsuboi et al., 2011; Ueda et al., 2013) (figure 1.2).

The major degradation pathway of NAEs is their hydrolysis to free fatty acids and ethanolamine (figure 1.2). The enzyme fatty acid amide hydrolase (FAAH) localized in the endoplasmic reticulum shows a major role in this process (Schmid et al., 1985; Cravatt et al., 1996). The lysosomal enzyme N-acylethanolamine-hydrolyzing acid amidase (NAAA) is preferentially active on the PEA-containing substrate (Ueda et al., 2001; Tsuboi at al., 2005).

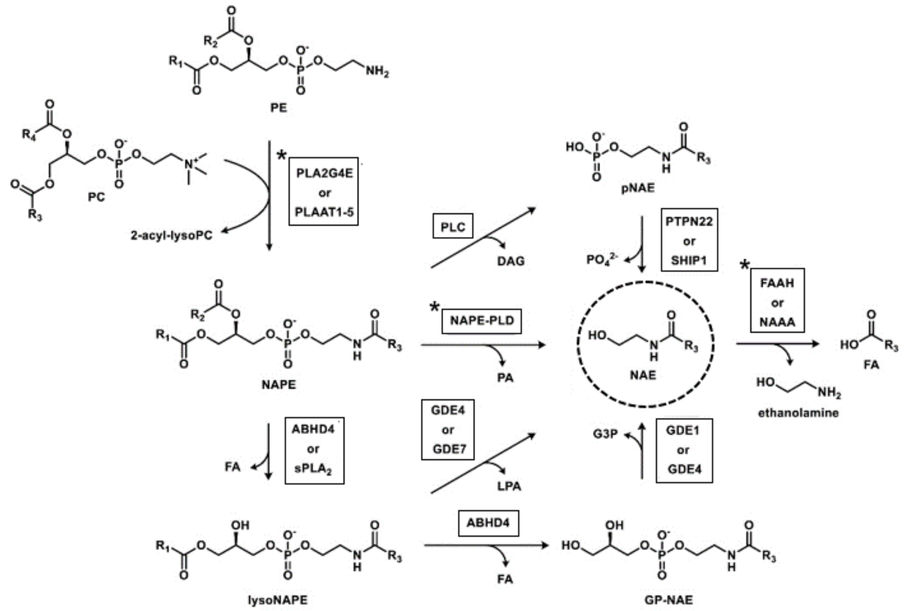

Figure 1.2. Metabolic pathway for NAEs biosynthesis and degradation. NAPE-PLD-dependent and –independent pathways to produce NAEs are reported. Asterisks indicate the enzymes included in the canonical pathway. Several enzymes, including α/β-hydrolase domain-containing protein (ABHD) 4, glycerophosphodiesterase (GDE) family proteins and PLC type enzymes, were proposed to constitute the NAPE-PLD-independent pathways. FAAH plays the central role in the degradation of bioactive *N*AEs, however also the lysosomal enzyme NAAA contributes to the fatty acid amides degradation.
PLAAT1-5, phospholipase/acyltransferase 1-5; ABHD4, α,β-hydrolase domain 4; GDE1,4 or 7, glycerophosphodiesterase 1,4 or 7; PLC, phospholipase C; PTPN22, protein tyrosine phosphatase non receptor type 22; SHIP1, phosphatidylinositol 3,4,5-trisphosphate 5-phosphatase 1; NAAA, *N*-acylethanolamine acid amidase; GP-NAE, glycerophospho-*N*-acylethanolamine; LPA, lysophosphatidic acid; PA, phosphatidic acid; DAG, diacylglycerol; G3P, glycerol-3-phosphate; pNAE, phospho-*N*-acylethanolamine. Adapted from Mock et al., 2023.

1.1.2 Physiological functions of NAEs

NAEs exert various physiological functions in biological systems interacting with different receptors. Among these, AEA is the major agonist of the cannabinoid receptors of type-1 (CB1) and type 2 (CB2), metabotropic G-protein coupled receptors of the endocannabinoid system (ECS) that are widely distributed throughout the mammalian body. The former are mainly located in the brain, the latter in the periphery. Due to this action of AEA, the enzymes involved in the biosynthesis and degradation of AEA and other

NAEs (e.g., ABDH4, GDE-1, NAPE-PLD, PTPN22, FAAH) are also part of endocannabinoid system (Figure 1.2).

Anyhow, different studies have revealed that other NAEs (e.g. PEA, OEA, LEA, SEA, DHEA), G-type receptors (e.g., GPR55, GPR119, GPR18) and ion channels as the transient receptor potential vanilloid (TRPV) channels (TRPV1 and TRPV2) are structurally and functionally related to the complex ECS (Iannotti and Vitale, 2021).

Here we report an overview of the main known physiological functions of NAEs:

- *Pain modulation and anti-inflammatory effects*: NAEs, such as AEA, OEA, and PEA have been extensively studied for their analgesic and anti-inflammatory effects. Anandamide can modulate pain perception by interacting with the cannabinoid receptors (e.g. CB1 and CB2 receptors), and by inhibiting the release of neurotransmitters involved in pain signalling, such as substance P and glutamate (Bouchet and Ingram, 2020). Piomelli's group demonstrated that the blockade of FAAH produced antinociception via a CB1 receptor dependent mechanism (Clapper et al., 2010). AEA also modulates inflammation via CB2 receptor activation and thus by reducing pro-inflammatory cytokines in cells (Maccarrone et al., 2015; Turcotte et al., 2015). Anandamide can also interact with the transient receptor potential vanilloid 1 (TRPV1) channel, localized at peripheral sensory neurons as well as in the central nervous system (CNS) (Zygmunt et al. 1999; Tòth et al., 2009; Martins et al., 2014; Marrone at al., 2017) and involved in pain sensation, particularly in response to heat and inflammation. The activation of TRPV1 by AEA was correlated to locomotor depression, hyperalgesia under inflammatory conditions, vasodilation and hypothermia (van der Stelt et al., 2005; Mock et al., 2023). Other NAEs, such as PEA and OEA, also have the ability to reduce inflammation and sensitization of pain receptors, thereby contributing to pain relief. The nuclear receptor PPAR-α was found to mediate their anti-inflammatory and analgesic effects (Hansen et al., 2010; O'Sullivan, 2016).

- *Neuroprotection*: NAEs have been shown to exhibit neuroprotective effects in various experimental models. They can protect neurons from damage caused by oxidative stress, inflammation, and excitotoxicity. NAEs also promote neuronal survival and enhance the maintenance of neural integrity, potentially contributing to the treatment of neurodegenerative diseases and brain injuries (Kasatkina et al., 2021). AEA was reported to promote neuroprotection and memory formation via brain CB1 receptor activation (van der Stelt et al., 2001; Marsicano et al., 2003; Morena et al., 2014). OEA, PEA, LEA were reported to exert neuroprotective actions via different mechanisms including PPAR-α activation (Hansen, 2010; O'Sullivan et al., 2016; Iannotti et al., 2016; Pérez-Martín et al., 2021). Exogenous administration of PEA showed to produce neuroprotection in various disease models (e.g. traumatic brain injury, Alzheimer's and Parkinson's disease) (Berger et al., 2004; Gonzalez-Aparicio et al., 2013; Esposito et al., 2014; Beggiato et al.; 2019; Beggiato et al. 2020; Landolfo et al., 2022).

- *Appetite and metabolism regulation*: among NAEs, OEA, LEA, and PEA were reported to be involved in feeding regulation, lipid metabolism and energy expenditure modulation. In particular, OEA acts as a satiety signal and can suppress appetite and food intake (de Fonseca et al., 2001). LEA and PEA are known to be involved in the reduction of food intake, while the endocannabinoid AEA is known to induce appetite (Hansen and Diep, 2009; Hansen, 2014). NAEs can also modulate lipid metabolism and energy expenditure. OEA is the well-studied member of the family, especially in the gastrointestinal system (Fu et al., 2007; Igarashi et al., 2023). It acts by activation of three different receptors including PPAR-α, the GPCR119 and TRPV1 (Fu et al., 2003; Wang et al., 2005; Oveisi et al., 2004; Piomelli, 2013). Most of the studies on OEA undertaken over the past 20 years have concentrated on its potential contribution to the development of potential treatments for obesity and eating disorders (de Fonseca et al., 2001; Laleh et al., 2018; Romano et al. 2023).

- *Cardiovascular health*: NAEs have been implicated also in cardiovascular health and regulation. They can influence blood pressure, heart rate, and vascular function. NAEs have vasodilatory properties, which contribute to the regulation of blood flow and cardiovascular homeostasis. Previous knowledge indicates that one of the most well-known actions of AEA and other NAEs (e.g. OEA, PEA) on the cardiovascular system is their ability to induce vasorelaxation by various mechanisms involving the endothelial cannabinoid receptors, CB1 and CB2, as well as TRPV1, PPARs receptors activation (Montecucco and Di Marzo, 2012; O'Sullivan, 2015; Stanley et al., 2016).

It is important to note that investigating the NAEs function continues to be an active area of research, in different physiological and pathological processes.

1.1.3 Modulation of NAEs metabolism

NAEs constitute a class of bioactive lipid molecules with crucial roles in various physiological processes. NAE signalling pathways can become dysregulated in specific pathological conditions, making the modulation of NAE levels a potential therapeutic strategy. This modulation involves controlling the enzymes and processes responsible for NAE synthesis, degradation, and transport. Due to the complex nature of NAEs interactions with multiple receptors, the optimal direction of modulating NAE levels (whether to enhance or reduce) can vary depending on the specific condition being targeted (Di Marzo, 2008). As mentioned above, NAEs such as AEA and PEA interact with various receptors in the body, including cannabinoid receptors (CB1 and CB2), PPARs, GPCRs, TRPV channels, which play roles in the regulating of pain, inflammation, immune response, and other key processes. Documented evidence suggests that reducing NAE levels could offer therapeutic benefits in conditions like obesity, metabolic disorders, and neurodegenerative diseases (Di Marzo, 2008). Recent research has described first-generation NAE biosynthesis inhibitors targeting enzymes such as NAPE-PLD and PLAAT (Castellani et al., 2017; Zhou et al., 2019; Aggarwal et al., 2020; Zhou et al., 2020; Mock et al., 2021; Mock et al., 2023). The decrease in NAE levels has been widely explored in the context of obesity and metabolic syndrome (Di Marzo and Matias, 2008; Piazza et al., 2017). Activation of CB1 receptors in adipocytes leads to increased glucose uptake, adipogenesis, and lipogenesis (Cota et al, 2003; Matias et al., 2016). Similarly, the activation of endocannabinoid receptors CB1 at hepatic level triggers fatty acid synthesis, which can lead to diet-induced obesity (Osei-Hyiaman et al., 2005). Thus, inhibition of NAE biosynthesis is being explored also as a therapeutic approach for obesity, as NAE signalling is often dysregulated in metabolic diseases (Mazier et al., 2015; Rakotoarivelo et al., 2021). High-fat diets have been observed to elevate circulating endocannabinoids, including AEA, accompanied by increased synthesis of NAE biosynthetic enzymes, particularly NAPE-PLD, in adipose tissue (Kuipers et al., 2019). These findings suggest that inhibiting NAPE-PLD may be a potential treatment for metabolic syndrome and obesity. However, recent studies have revealed the crucial role of adipose tissue NAPE-PLD in regulating whole-body metabolism, underscoring its importance in maintaining energy balance and metabolism under normal physiological conditions (Geurts et al., 2015). In mice without this functional synthesis pathway, alteration in the gut microbiome and browning programme were observed, as well as inflammation of the adipose tissue with development of obesity, insulin resistance and glucose intolerance. (Geurts et al., 2015). Intestinal deletion of NAPE-PLD produced mice hyperphagic upon high-fat diet exposure and developed obesity and steatosis. These results suggested that the intestinal NAPE-PLD is a key regulator of energy homeostasis and a metabolic sensor of dietary fat and highlighted the importance of intestinal NAE in the metabolic adaptations to a lipid-rich diet (Everard et al., 2019). Overall, these findings underlie the importance of tissue-specific differences in ECS regulation.

In addition, NAE signalling has also been widely investigated in the brain. It is involved in various processes, including memory formation, stress, anxiety, and inflammation (Lutz et al., 2015). Dysregulated brain NAE levels have been reported in neurological disorders. In the case of neurodegenerative diseases, elevated AEA levels in human cerebrospinal fluid have been linked to potential neuroprotection via CB1 or CB2 receptor activation due to the neuroinflammatory components of these diseases (Chiurchiù et al., 2018; Marchioni et al., 2018; Leuti et al., 2020). The potential benefits of reducing NAE levels in the central nervous system are still under investigation (Di Marzo et al., 2015; Morena et Hill, 2019). Recent research has unveiled potential biological functions of NAE biosynthetic enzymes in the brain. A frameshift variant of NAPE-PLD, which replaces the C-terminal metallo-beta-lactamase domain of the wild-type protein, has been identified as a risk factor for leukoencephalomyelopathy in several dog breeds (Minor et al., 2018). This suggests the involvement of NAPE-PLD in myelin homeostasis, potentially serving as a novel candidate gene for myelination disorders in humans (Minor et al., 2018).

Recently, improving the tone of NAEs with small molecule activators of NAPE-PLD have been proposed (Zarrow et al., 2023). Indeed, reduced NAPE-PLD expression has been observed in human coronary arteries with unstable atherosclerotic plaques, and defective efferocytosis has been linked to the enlargement of necrotic cores in these lesions. NAPE-PLD products, such as PEA and OEA, have been shown to enhance efferocytosis (Fu et al., 2005; Rinne et al., 2018). Therefore, enzyme activation through small molecules may serve as a therapeutic approach for cardiometabolic diseases (Zarrow et al., 2023).

In summary, increasing or reducing NAE levels can be beneficial depending on the desired therapeutic outcomes. However, further research is needed to fully understand the roles of NAEs in different conditions and to develop targeted strategies for modulating their levels effectively.

1.2 NAPE-PLD

1.2.1 Outline on NAPE-PLD characterization

NAPE-PLD is a membrane-associated phospholipase currently considered the sole mammalian enzyme directly generating NAEs from NAPEs (Okamoto et al., 2009). NAPE-PLD is unrelated to other mammalian phospholipases D (PLD1 and PLD2) (Stuckey and Dixon, 1999), and further differs from these enzymes in its ability to selectively hydrolyse NAPEs (Okamoto et al., 2004). Importantly, NAPE-PLD recognizes all NAPEs, irrespective of their *N*-acyl substituents (Wang et al., 2006), and is able therefore to produce NAEs with diverse biological activities. NAPE-PLD and its activity were first identified in rat heart (Schmid et al., 1983) and successively in other animal tissues (Liu et al., 2002; Natarajan et al., 1984; Petersen and Hansen, 1999; Sugiura et al., 1996; Ueda et al., 2001). It is widely expressed in many tissues including brain, intestine, heart, and kidney (Schmid et al., 1983; Petersen et al., 2000; Okamoto et al., 2004; Fu et al., 2007, Egertová et al., 2008).

Cloning of NAPE-PLD from human, rat, and mouse by Ueda's group enabled the characterization of this enzyme by molecular biology (Okamoto et al., 2004). NAPE-PLD is composed of 393 (human) – 396 (rat) amino acids, and its sequence is highly conserved among mammalian species (figure 1.3).

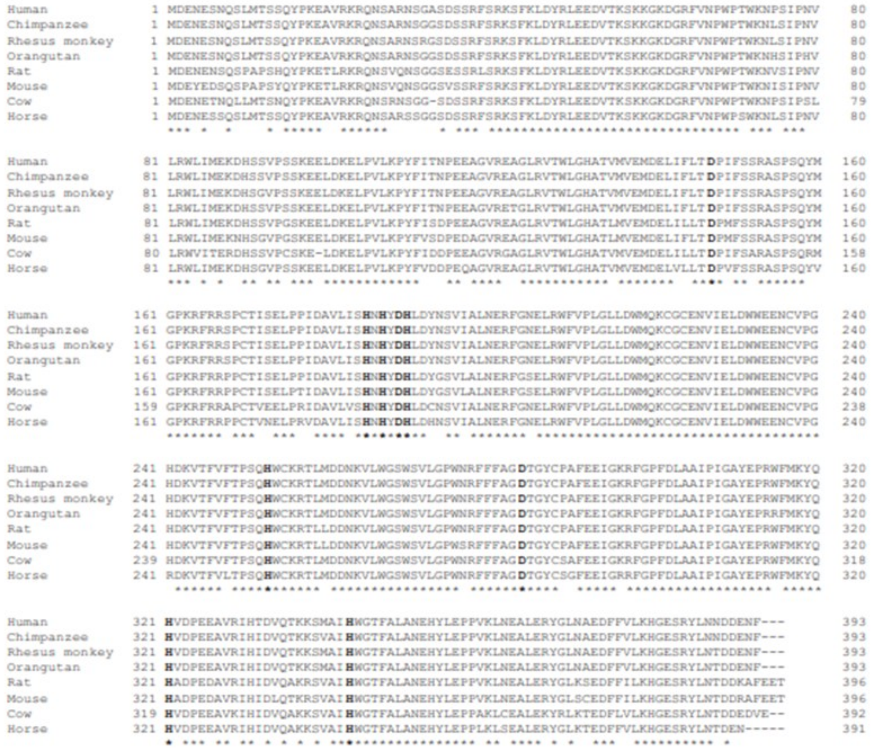

```
Human              1 MDENESNQSLMTSSQYPKEAVRKRQNSARNSGASDSSRFSRKSFKLDYRLEEDVTKSKKGKDGRFVNPWPTWKNPSIPNV    80
Chimpanzee         1 MDENESNQSLMTSSQYPKEAVRKRQNSARNSGGSDSSRFSRKSFKLDYRLEEDVTKSKKGKDGRFVNPWPTWKNLSIPNV    80
Rhesus monkey      1 MDENESNQSLMTSSQYPKEAVRKRQNSARNSRGSDSSRFSRKSFKLDYRLEEDVTKSKKGKDGRFVNPWPTWKNLSIPNV    80
Orangutan          1 MDENESNQSLMTSSQYPKEAVRKRQNSARNSGGSDSSRFSRKSFKLDYRLEEDVTKSKKGKDGRFVNPWPTWKNHSIPHV    80
Rat                1 MDENENSQSPAPSHQYPKETLRKRQNSVQNSGGSESSRLSRKSFKLDYRLEEDVTKSKKGKDGRFVNPWPTWKNVSIPNV    80
Mouse              1 MDEYEDSQSPAPSYQYPKETLRKRQNSVQNSGGSVSSRFSRKSFKLDYRLEEDVTKSKKGKDGRFVNPWPTWKNISIPNV    80
Cow                1 MDENETNQLLMTSNQYPKEAVRKRQNSRNSGG-SDSSRFSRKSFKLDYRLEEDVTKSKKGKDGRFVNPWPTWKNPSIPSL    79
Horse              1 MDENESSQSLMTSSQYPKEAVRKRQNSARSSGGSDSSRFSRKSFKLDYRLEEDVTKSKKGKDGRFVNPWPSWKNLSIPNV    80
                     *** *  *    * *****  ******      * *** ******************************* *** ***

Human             81 LRWLIMEKDHSSVPSSKEELDKELPVLKPYFITNPEEAGVREAGLRVTWLGHATVMVEMDELIFLTDPIFSSRASPSQYM   160
Chimpanzee        81 LRWLIMEKDHSSVPSSKEELDKELPVLKPYFITNPEEAGVREAGLRVTWLGHATVMVEMDELIFLTDPIFSSRASPSQYM   160
Rhesus monkey     81 LRWLIMEKDHSGVPSSKEELDKELPVLKPYFITNPEEAGVREAGLRVTWLGHATVMVEMDELIFLTDPIFSSRASPSQYM   160
Orangutan         81 LRWLIMEKDHSSVPSSKEELDKELPVLKPYFITNPEEAGVRETGLRVTWLGHATVMVEMDELIFLTDPIFSSRASPSQYM   160
Rat               81 LRWLIMEKDHSSVPGSKEELDKELPVLKPYFISDPEEAGVREAGLRVTWLGHATLMVEMDELILLTDPMFSSRASPSQYM   160
Mouse             81 LRWLIMEKNHSGVPGSKEELDKELPVLKPYFVSDPEDAGVREAGLRVTWLGHATLMVEMDELIFLTDPMFSSRASPSQYM   160
Cow               80 LRWVITERDHSSVPCSKE-LDKELPVLKPYFIDDPEEAGVRGAGLRVTWLGHATVMVEMDELILLTDPIFSARASPSQRM   158
Horse             81 LRWLIMEKDHSGVPSSKEELDKELPVLKPYFVDDPEQAGVREAGLRVTWLGHATVMVEMDELVLLTDPVFSSRASPSQYV   160
                     *** * *  ** ** *** ************   ** ****  *********** *******  **** ** ******

Human            161 GPKRFRRSPCTISELPPIDAVLISHNHYDHLDYNSVIALNERFGNELRWFVPLGLLDWMQKCGCENVIELDWMEENCVPG   240
Chimpanzee       161 GPKRFRRSPCTISELPPIDAVLISHNHYDHLDYNSVIALNERFGNELRWFVPLGLLDWMQKCGCENVIELDWMEENCVPG   240
Rhesus monkey    161 GPKRFRRSPCTISELPPIDAVLISHNHYDHLDYNSVIALNERFGNELRWFVPLGLLDWMQKCGCENVIELDWMEENCVPG   240
Orangutan        161 GPKRFRRSPCTISELPPIDAVLISHNHYDHLDYNSVIALNERFGNELRWFVPLGLLDWMQKCGCENVIELDWMEENCVPG   240
Rat              161 GPKRFRRPPCTISELPPIDAVLISHNHYDHLDYGSVLALNERFGSELRWFVPLGLLDWMQKCGCENVIELDWMEENCVPG   240
Mouse            161 GPKRFRRPPCTISELPTIDAVLISHNHYDHLDYGSVLALNERFGSELRWFVPLGLLDWMQKCGCENVIELDWMEENCVPG   240
Cow              159 GPKRFRRAPCTVEELPRIDAVLVSHNHYDHLDCNSVIALNERFGNELRWFVPLGLLDWMQKCGCENVIELDWMEENCVPG   238
Horse            161 GPKRFRRPPCTVNELPRVDAVLISHNHYDHLDHNSVIALNERFGNELRWFVPLGLLDWMQKCGCENVIELDWMEENCVPG   240
                     ******* ***  ***  **** *********  ** ******* ***********************************

Human            241 HDKVTFVFTPSQHWCKRTLMDDNKVLWGSWSVLGPWNRFFFAGDTGYCPAFEEIGKRFGPFDLAAIPIGAYEPRWFMKYQ   320
Chimpanzee       241 HDKVTFVFTPSQHWCKRTLMDDNKVLWGSWSVLGPWNRFFFAGDTGYCPAFEEIGKRFGPFDLAAIPIGAYEPRWFMKYQ   320
Rhesus monkey    241 HDKVTFVFTPSQHWCKRTLMDDNKVLWGSWSVLGPWNRFFFAGDTGYCPAFEEIGKRFGPFDLAAIPIGAYEPRWFMKYQ   320
Orangutan        241 HDKVTFVFTPSQHWCKRTLMDDNKVLWGSWSVLGPWNRFFFAGDTGYCPAFEEIGKRFGPFDLAAIPIGAYEPRRFMKYQ   320
Rat              241 HDKVTFVFTPSQHWCKRTLLDDNKVLWGSWSVLGPWNRFFFAGDTGYCPAFEEIGKRFGPFDLAAIPIGAYEPRWFMKYQ   320
Mouse            241 HDKVTFVFTPSQHWCKRTLLDDNKVLWGSWSVLGPWSRFFFAGDTGYCPAFEEIGKRFGPFDLAAIPIGAYEPRWFMKYQ   320
Cow              239 HDKVTFVFTPSQHWCKRTLMDDNKVLWGSWSVLGPWNRFFFAGDTGYCSAFEEIGKRFGPFDLAAIPIGAYEPRWFMKYQ   318
Horse            241 RDKVTFVLTPSQHWCKRTLMDDNKVLWGSWSVLGPWNRFFFAGDTGYCSGFEEIGRRFGPFDLAAIPIGAYEPRWFMKYQ   320
                      ****** *********** **************** ***********  ***** ****************** *****

Human            321 HVDPEEAVRIHTDVQTKKSMAIHWGTFALANEHYLEPPVKLNEALERYGLNAEDFFVLKHGESRYLNNDDENF---       393
Chimpanzee       321 HVDPEEAVRIHIDVQTKKSVAIHWGTFALANEHYLEPPVKLNEALERYGLNAEDFFVLKHGESRYLNNDDENF---       393
Rhesus monkey    321 HVDPEEAVRIHIDVQTKKSMAIHWGTFALANEHYLEPPVKLNEALERYGLNAEDFFVLKHGESRYLNTDDENF---       393
Orangutan        321 HVDPEEAVRIHIDVQTKKSMAIHWGTFALANEHYLEPPVKLNEALERYGLNAEDFFVLKHGESRYLNTDDENF---       393
Rat              321 HADPEDAVRIHIDVQAKRSVAIHWGTFALANEHYLEPPVKLNEALERYGLKSEDFFILKHGESRYLNTDDKAFEET       396
Mouse            321 HADPEDAVRIHIDLQTKRSVAIHWGTFALANEHYLEPPVKLNEALERYGLSCEDFFILKHGESRYLNTDDRAFEET       396
Cow              319 HVDPEEAVKIHIDVQAKKSVAIHWGTFALANEHYLEPPAKLCEALEKYRLKTEDFLVLKHGESRYLNTDDEDVE--       392
Horse            321 HVDPEEAVRIHIDVQAKKSVAIHWGTFALANEHYLEPPLKLSEALERYGLKTEDFFVLKHGESRYLNTDEN-----       391
                     * *** ** ** * * * * ****************** ** **** * *  ***  ********** *
```

Figure 1.3. Alignment of the amino acid sequences from cDNAs for NAPE-PLD orthologues of various mammals. Asterisks indicate identity shared by the sequences and dashes indicate lack of amino acid residues. Histidine and aspartic acid residues important for the catalytic activity are shown in bold. Adapted from Okamoto et al., 2009.

According to the NCBI database, amino acid identity of human NAPE-PLD with other mammalian orthologs was 99.0% (chimpanzee), 98.5% (rhesus monkey), 98.2% (orangutan), 93.1% (giant panda), 90.6% (rat), 90.6% (horse), 90.1% (cow) and 89.3% (mouse).

NAPE-PLD gene is assigned to chromosome 7q22 in human (Gene ID: 222236). The sequence of the NAPEPLD gene predicts a member of the metallo-β-lactamases (MβLs) (Wang et al., 2006), a protein superfamily that includes hydrolases involved in antibiotic resistance, DNA repair and RNA maturation (Garau et al., 2005).

1.2.2 Structure of NAPE-PLD

To understand how NAPE-PLD works and the molecular bases of NAEs biosynthesis, recently our group determined the crystal structure of human membrane NAPE-PLD at a resolution of 2.65 Å (PDB ID: 4QN9) (Magotti et al., 2015), crystallized in the presence of the detergent sodium deoxycholate (DCA) (figure 1.4).

Our structural studies highlighted three structural features that distinguish NAPE-PLD. First, the enzyme formed a dimer with two interconnected protein subunits of ~42 kDa. Each subunit contains the four-layered αββα core typical of the MβL superfamily (Pettinati et al., 2016). However, various structural elements distinguish NAPE-PLD from other MβL proteins and allow this enzyme to interact with cell membrane phospholipids. These elements include an elongated N-terminal helix α0 and loop L0, which replace the β1 strand present in most MβL proteins, and a second extended loop (L1), which substitutes for the MβL α1 helix. Together with helices α0 and α2, L0 and L1 form at the dimer interface an internal channel with a diameter of ~9 Å (figure 1.4a).

Second, a hydrophobic nook facing the lipid bilayer provides a recognition filter for NAPEs and allows these negatively charged lipids to access the active site, where a dinuclear zinc center orchestrates their hydrolysis. Finally, specific pockets within this cavity tightly bind four bile acid (BA) molecules, creating a unique protein–lipid molecular architecture that promotes the biosynthesis of bioactive lipid amides (figure 1.4b).

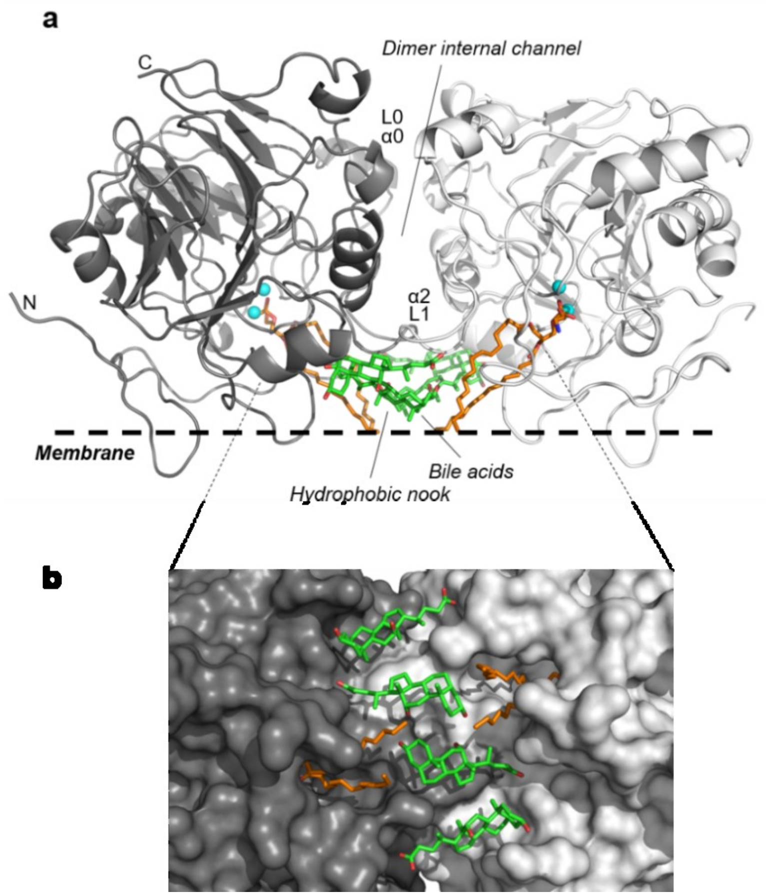

Figure 1.4. Structure of human NAPE-PLD. a) Ribbon trace of the NAPE-PLD dimer. Dimer subunits interact mainly through their loops L0 and L1, structural elements that distinguish NAPE-PLD from other MβL proteins. The subunit orientation produces a symmetric alignment of loops L1, which extend in the dimer the existing monomer binding faces. The active sites contain a binuclear zinc metal centre (spheres in cyan), which faces the lipid bilayer and binds a molecule of phosphatidylethanolamine (PE) (carbon atoms in orange). PE derives from the expression system used to produce NAPE-PLD and occupies the binding site reserved to the PE fragment of NAPE. Four molecules of the bile acid DCA (carbon atoms in green) bind to the enzyme, creating a lipid substructure at the interface with the membrane. N and C indicate the N-terminus and C-terminus of the protein, respectively. An internal channel with a diameter of ~9 Å partly separates the two subunits of NAPE-PLD and overlooks a hydrophobic nook to which PE and the bile acid DCA are bound. The predicted membrane boundary is shown as dotted line (Magotti et al., 2015). b) Expanded view of the membrane-interacting protein dimer surface in (a) with interposed molecules of the BA (carbons in green). The molecules of the bile acid DCA promote the association and formation of the protein-membrane complex, facilitating the incorporation of the phospholipidic substrate NAPE (carbon atoms in orange) into the active site of both dimeric subunits.

1.2.3 Bile acids modulation of NAPE-PLD

The crystal structure of human NAPE-PLD obtained recently in our laboratory disclosed how the dinuclear zinc active site of the enzyme recognizes NAPE and catalyzes the production of NAEs. Structural and functional analysis unveiled that the secondary bile acid deoxyxcholic acid (DCA) binds the protein dimer, in a specific cavity close to the active site (figure 1.4b). Results showed the interaction between NAPE-PLD and the steroid acid was a stimulus for the enzyme hydrolytic process (Magotti et al., 2015). In a recent study of our group, we demonstrate that in the presence of this secondary bile acid, the stiffness of the protein increases, and NAPE-PLD catalyzes the hydrolysis of more unsaturated substrates (Margheritis et al., 2016) at a 7 times higher rate. Overall, these findings provide important insights into the allosteric regulation of the enzyme mediated by bile acid cofactors, revealing that NAPE-PLD responds primarily to the number and position of their hydroxyl groups (Margheritis et al., 2016). The membrane dimeric enzyme is turned on by the interaction with bile acids at physiological concentrations (μM range), and the bound bile acid molecules act as structural cofactors at membrane interface. This unexpected important discovery brings together bile acid physiology and lipid amide signaling, linking major players in lipid homeostasis with major players in lipid signaling (Margheritis et al., 2016; Ahmad and Haeusler, 2019). The comprehensive exploration of NAPE-PLD at atomic level, from its molecular characteristics to its intricate structural features, has positioned this phospholipase D as a key player in lipid amide signaling and metabolism. The discovery of a specific modulation by bile acids has enhanced the complexity of this important protein system. The structural insights not only expand our understanding of its catalytic processes, but also present potential avenues for therapeutic interventions. The unique protein dimer architecture of NAPE-PLD provides structural bases for the design of small-molecule modulators, and exciting prospects for the development of targeted therapeutic applications.

1.3 Insights into protein-ligand interactions

Several proteins require interactions with small ligand molecules to effectively fulfill their biological roles. These protein-ligand interactions are crucial in enzymatic catalysis, signal transduction, and drug action. Protein-ligand binding occurs mainly through non-covalent interactions, which encompass hydrogen bonding, electrostatic attractions, hydrophobic associations, and van der Waals forces denoting the specific and reversible interaction between a protein and a ligand molecule. Gaining insights into the mechanisms and dynamics of interactions between proteins and ligands is crucial for structural biology, drug discovery and the rational development of therapeutic agents. Studying protein-ligand or protein-protein complexes can uncover intricate details about their interactions and how they regulate their complexes (Yuan et al., 2013).

There are several biophysical methods utilizing various physical and chemical principles to investigate the interactions between proteins and their ligands. Techniques like mass spectrometry (MS), isothermal titration calorimetry (ITC), surface plasmon resonance (SPR), nuclear magnetic resonance (NMR) spectroscopy and X-ray diffraction (XRD), provide valuable insights into binding affinity, kinetics, thermodynamics, and high-resolution structural information. Among these, SPR monitors real-time binding events by detecting changes in refractive index, providing information about binding constants, affinity, and stoichiometry. XRD allows obtaining the three-dimensional arrangement of a protein-ligand complex at atomic resolution (Zheng et al. 2014). In recent years, single particle cryo-electron microscopy (cryo-EM) has emerged as a complementary technique to crystallography.

Cryo-EM involves freezing the sample in vitreous ice and imaging it with an electron microscope. This technique allows the analysis of larger and more complex biological systems that cannot be crystalized. Additionally, cryo-EM permits the analysis of proteins in solution and the characterization of multiple conformational or compositional states from the same sample, thereby providing insights into states of the macromolecule closer to the native state (Nogales and Scheres, 2015; Frank et al., 2017; Scapin et al., 2018; Hoelzgen et al., 2021). Despite recent advancements in technology, such as the introduction of direct electron detectors and improved computational image analysis techniques are significantly enhancing the capabilities of cryo-EM. Obtaining high-resolution structural information for protein-ligand complexes with cryo-EM can be challenging, and X-ray crystallography continues to remain the gold standard for protein structure determination (Renaud et al., 2018; Scapin et al., 2018; García-Nafría and Tate, 2020; Robertson et al., 2021). Computational approaches can also contribute to the study of protein-ligand interactions. Molecular docking methodologies are useful to predict the optimal binding mode and affinity of a ligand to a protein by exploring the conformational space and scoring different poses (Anderson, 2003). Molecular dynamics simulations simulate the movement of atoms over time, allowing the exploration of the flexibility and dynamics of the protein-ligand complex.

In the next paragraphs, we will provide a concise overview of the two methodologies applied in this work to explore protein-ligand interactions: the surface plasmon resonance and X-ray diffraction.

1.3.1 Surface Plasmon Resonance

Besides all the techniques available for protein-ligand binding studies, the SPR detection method has been used as a "gold" standard technique to measure biomolecular interactions. SPR allows real-time monitoring of molecular interactions, enabling the characterization of binding kinetics and affinity between biomolecules, such as proteins and small molecules. This technique offers several advantages as a label-free method for studying ligand binding. It provides real-time, quantitative, and kinetic information without the need for labeling or modification of the molecules under investigation. Over the past two decades, we assisted in the implementation of SPR technology with a consequence broadening of its applications that cover fields like medicinal chemistry, environment, and food quality (Patching, 2014; Capelli et al., 2023).

SPR is a physical phenomenon that occurs when plane-polarized light hits a thin metal film, such as gold, under total internal reflection condition (TIR). A SPR biosensor chip consists in a glass slide coated with a thin gold layer functionalized using various chemistries and in fluid contact with a nanoliter-scale flow cell. When light is shone through a prism on a sensor chip coated with a thin metal film on top, the free electrons in the metal oscillate in response to the electric field of the light, producing a surface plasmon wave that propagates along the metal surface (figure 1.5a). The evanescent wave that enables the energy transfer into the metal film exhibits exponential decay with distance from the gold interface and is therefore sensitive to a penetration depth of ~300 nm from the sensor surface (Schasfoort, 2017). The resonance occurs when the angle of incidence of the light matches the angle at which the surface plasmon wave is excited. At this angle, the intensity of the reflected light drops to a minimum, resulting in a sharp dip in the reflectance spectrum. The angle at which the maximum loss of the reflected light intensity occurs is called resonance angle or SPR-dip (Homola et al., 2008; Schasfoort, 2017). The resonance angle is sensitive to changes in the refractive index of the dielectric material in contact with the metal film. When a target molecule binds to the immobilized biomolecules on the metal surface, it causes a change in the local refractive index leading to a shift in the

SPR angle (figure1.5b). By monitoring this shift in real-time, the binding events can be quantitatively analysed, providing information about the concentration, affinity, and kinetics of the molecular interactions. An SPR instrument typically combines a (i) sensor chip with a gold surface and a layer properly functionalized for ligand immobilization, integrated with a fluidics system enabling a flow-through operation and an (ii) optical detector for intensity shift measurement. In a typical SPR experiments, one molecule, the ligand (A), is immobilized on the sensor chip surface usually through covalent attachment or specific capture methods. The other molecule, the analyte or ligand-binding partner (B) is then passed over the sensor surface in a liquid flow system. As the analyte binds to the immobilized ligand on the sensor surface, it causes changes in the local refractive index, leading to a shift in the angle of incidence at which the surface plasmon resonance occurs (Schasfoort, 2017). This shift is detected as a change in the intensity of the reflected light. Association and dissociation are displayed in a graph called sensorgram (figure 1.5c). The response of the system is measured in RU (Response Unit. 1 RU = 1 x 10^{-6} change in refractive index = 1 pg/mm^2). A typical sensorgram is composed of five phases: baseline, association, equilibrium (or steady-state), dissociation, and regeneration. In the initial phase of the baseline a running or flow buffer is used to condition the sensor surface and check for any sensor system instability. The association phase of an analyte begins with their binding to an immobilized ligand, and it is indicated by the initial sharp rise of the SPR signal in the sensorgram. The steady-state phase occurs at the top flat portion of the sensorgram where the net rate of bound analytes is zero. The dissociation phase begins with replacement of the analyte solution with a wash buffer that leads to the disruption of specific analyte-ligand interaction, and it is represented by the downward-sloped curve after the steady-state phase. Finally, the regeneration phase consists of flowing a suitable buffer to re-establish the same stable SPR baseline signal of the beginning indicating that the sensor system is free of bound analytes and non-specifically adsorbed molecules. Regeneration of the surface is sometimes unnecessary if the analyte-ligand interaction has a fast dissociation rate (Schasfoort, 2017). Determining the kinetics of biomolecular interactions is the main advantage of direct detection using SPR biosensor technology. From a typical SPR experiments, reactions rates (k_{on}, k_{off}) and equilibrium constants (K_D) of interactions can be determined by fitting the data into a suitable binding model. For the simplest case where ligand-analyte binding happens at a 1:1 ratio (Langmuir binding), binding kinetics can be described by the following equation:

$$\mathrm{A} + \mathrm{B} \underset{k_{off}}{\overset{k_{on}}{\rightleftarrows}} \mathrm{AB}$$

The association rate constant (k_{on} or k_a) represents the reaction rate of the complex (AB) formation, giving the number of complexes formed per unit time at unit concentrations of A and B. The dissociation rate constant (k_{off} or k_d) expresses the number of AB complexes dissociating per unit time. When association of A and B starts, no product AB is yet present at the sensing surface and the rate of the association reaction is highest while the dissociation reaction is lowest. As the process progresses, more of the AB complex is produced enhancing the rate of dissociation. Equilibrium is reached when the rates of the association and dissociation reactions are equal. The equilibrium association constant ($K_A = k_{on} / k_{off}$, L mol^{-1}) and dissociation constant ($K_D = k_{off}/k_{on}$, mol L^{-1}) represent the affinity of an interaction. Rates constants and equilibrium constants of molecular interactions provide information on the strength of the association and the tendency of dissociation (Schasfoort, 2017).

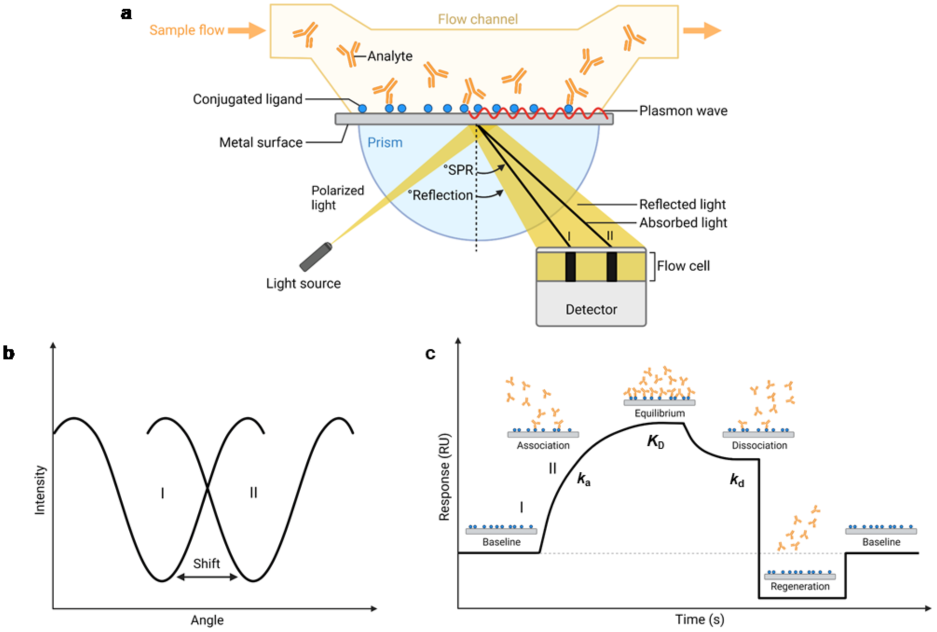

Figure 1.5. Surface plasmon resonance spectroscopy. a) Schematic representation setup for an SPR experiment. b) SPR curve shift toward angle I to angle II due to a change in the refractive index. In an SPR experiment, a dip or minimum in the reflectance spectrum (intensity of reflection in relation to the angle or wavelength), indicates the specific angle or wavelength at which the surface plasmons have absorbed the incident light. Once there is a change in refractive index at the sensing layer interface caused by the binding of molecules, the dip will shift, indicating a change in the resonance angle or wavelength. The observed variation in the reflected angle or wavelength directly corresponds to the quantity of bound analytes on the surface, which is directly related to an increase in mass. When this alteration in SPR response is graphed over time, it generates a sensorgram (Schasfoort, 2017). c) Response of the SPR experiment in the form of a sensogram which typical consists of five phases: baseline, association, equilibrium (or steady-state), dissociation and regeneration. k_{on}, association rate constant; k_{off}, dissociation rate constant; K_{D}, equilibrium dissociation constant. RU, resonance unit. Adapted from “Surface Plasmon Resonance (SPR)”, by BioRender.com (2024). Retrieved from https://app.biorender.com/biorender-templates.

1.3.2 X-ray crystallography

Structural biology plays a pivotal role in investigating protein-ligand interactions at the atomic level. It encompasses various techniques that provide detailed insights into the three-dimensional structures of proteins and their complexes with ligands. By visualizing the complex architecture of these interactions, structural biologists can unravel the fundamental principles governing protein-ligand recognition and binding. Among different approaches for the structural determination of protein targets and their complexes at atomic level, X-ray diffraction is the dominant and preferred method (Howard et al. 2014). In the last two decades, advancements in high-throughput structure determination using X-ray crystallography have resulted in a significant rise in the availability of three-dimensional protein structures in the protein database (PDB; http://www.pdb.org; (Berman et al., 2002). Among 216000 deposited structures so far, more than 180000 have been obtained by X-ray crystallography, including protein-protein complexes, protein-ligand complexes have been recorded in the PDB, encompassing a wide range of protein folds, and representing most protein classes. The structures deposited in the PDB often serve as initial models for determining the structures of unknown proteins through molecular replacement technique. Additionally, these structures are valuable for investigating protein-ligand interactions by means of soaking and co-crystallization experiments, providing insights into the relationships between structure and function. Importantly, crystallography strongly facilitates drug design and fragment screening programs that rely on structural information (Turnbull and Emsley, 2013).

1.3.2.1 Crystals and fundamental in crystal geometry

Crystallography is the science that study the formation, structure and properties of a crystal. Under specific conditions, many molecular substances, including proteins, can crystallize. The resulting crystal forms an orderly three-dimensional array of molecules held together by noncovalent interactions (Rhodes, 2006). In crystals, atoms, ions or molecules are packed to give rise to "motifs" repeated in three dimensions to form the crystal lattice. The motif consists of several such units, which may be converted into one another by symmetry operations (Hammond, 2008). The smallest repeating volume of the lattice is called unit cell, also known as the asymmetric unit. It is characterized by three lattice constants a,b,c (lengths of the basis vector) and by the three angles α, β, γ. The lengths of the edges of a unit cell and the angles between them are called lattice parameters or cell parameters (figure 1.6).

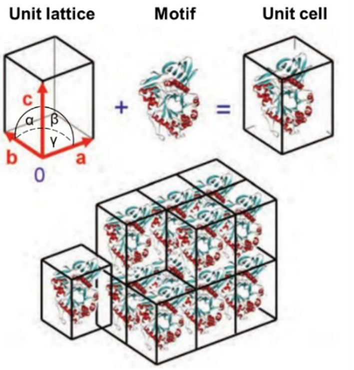

Figure 1.6. Crystal lattice and unit cell. Adapted from Rupp, 2009.

An important property of crystals is their symmetry and all the possible symmetries for the lattice give rise to the seven crystal systems (table 1.1), the broadest classification of unit cells (Rupp, 2009). The Bravais lattice system considers additional structural details to divide these seven systems into 14 unique Bravais lattices (figure 1.7).

Table 1.1. Classification of crystals: the seven crystal systems.

Crystal System	Lattice Centering	Axial Lengths	Axial Angles
Triclinic	P	a ≠ b ≠ c	α, β, γ ≠ 90°
Monoclinic	P C	a ≠ b ≠ c	β ≠ 90° and α, γ = 90°
Orthorhombic	P I C F	a ≠ b ≠ c	α, β, γ = 90°
Hexagonal	P	a = b ≠ c	α = β = 90° and γ = 120°
Trigonal	P R	a = b = c	α = β = γ ≠ 90°
Tetragonal	P I	a = b ≠ c	α, β, γ = 90°
Cubic	P I F	a = b = c	α, β, γ = 90°

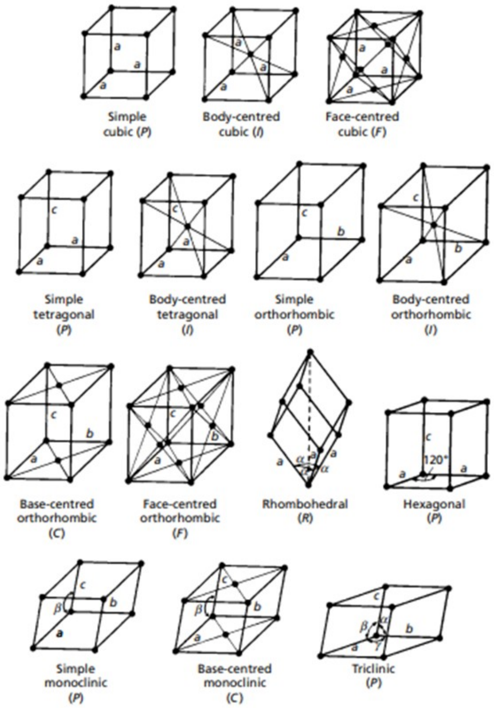

Figure 1.7. The fourteen Bravais Lattices. In a primitive lattice, lattice points are situated at the corners of the unit cells. Within space groups, primitive lattices are commonly denoted by the letter P. A body-centered crystal features a lattice point positioned at the center of the unit cell. In space groups, crystals with body-centered lattices are typically designated with the letter I. Body-centered lattices are found in the cubic, tetragonal, and orthorhombic crystal systems. A face-centered crystal incorporates a lattice point within each face of the unit cell. In space groups, crystals with face-centered lattices are typically represented with the letter F. Face-centered lattices are observed in the cubic and orthorhombic crystal systems. A base-centered crystal includes a lattice point solely in one set of opposing faces of the unit cell, conventionally designated as the ab face. In space groups, crystals with base-centered lattices are indicated by the capital letter of the axis opposite the centered faces, typically the c-axis, hence usually denoted by the letter C. Base-centered lattices are observed in the orthorhombic and monoclinic crystal systems. Adapted from Hammond, 2008.

When discussion symmetry operations, it is important to discern between 1) point symmetry elements and 2) translational symmetry. Point symmetry involves operations that leave at least one point unchanged and includes symmetry elements such as inversion centres (i), rotation axis (n, e.g., 2,3,4,6) and mirror planes (m). The set of point symmetry elements exhibited by an atomic or molecular arrangement is referred to as a point group. There are 32 point groups compatible with translational symmetry, encompassing all possible point symmetry elements present in finite molecules. To comprehensively describe the symmetry of crystal structures, it is necessary to incorporate two additional symmetry elements: screw axes (np) and glide planes (a, b, c), which combine rotation and reflection with the translational symmetry of the lattice, respectively. Groups that integrate both the point symmetry elements of finite molecules and the translational elements of a crystal lattice are known as space groups. Every crystal structure is assigned a space group based on the symmetry within the crystal, which can have any combination of these symmetry operations. By combining the point groups, Bravais lattices and translation symmetry elements, a total of 230 unique space groups are generated. Only 65 distinct ways exist to assemble 3-dimensional, periodic crystals from asymmetric, chiral molecule through combination of translational and rotational symmetry (65 space groups). A protein crystals structure must belong to one of these 65 chiral space groups (Rupp, 2009).

The three-dimensional images (the spot locations and their intensities) collected during an X-ray diffraction experiment contain a geometric pattern of peaks that derive directly from the lattice and the unit cell geometry of the crystal system. The position of the peaks (or their absence) is used to determine the symmetry of the unit cell. The "systematic absences" within the image represent positions where h, k, l reflections are absent due to destructive wave interference. These absent reflections play a critical role in space group assignment, because the omission of certain reflections in specific space symmetries present in a crystal. (Clegg, 2015).

1.3.2.2 X-ray diffraction basis: the Bragg's Law

When X-ray beams pass through a crystal, they interact with the numerous electron clouds present in the crystal. Following Bragg's Law, these interactions cause the X-ray beams to scatter and form a distinct diffraction pattern composed of spots (reflections), which are then captured and recorded as images (figure 1.8a) (Hammond, 2008).

Bragg showed that a set of parallel planes with interplanar spacing d produces a diffracted beam when X-rays of wavelength λ impinge upon the planes at an angle θ and they are reflected at the same angle only if θ meets the condition:

$$n\lambda = 2d\sin\theta$$

where n is an integer (diffraction order). In figure 1.8b is reported the geometric construction that demonstrates the conditions necessary for producing a strong diffracted ray.

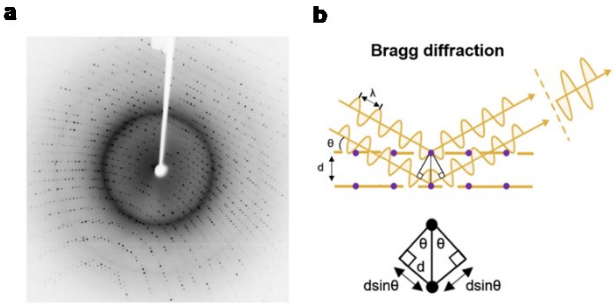

Figure 1.8. X-ray diffraction. a) X-ray diffraction pattern of a protein crystal. Adapted from Kermani, 2020. b) Schematic representation of Bragg's law conditions. When two beams with the same wavelength and phase interact with two separate atomic planes, constructive interference happens if the lower beam travels an additional distance of $2d\sin\theta$, and this extra distance is equal to a whole number (integer) multiple of the wavelength ($n\lambda=2d\sin\theta$). The dots represent two parallel planes of lattice points with interplanar spacing d and the two rays are reflected from them at angle θ (Hammond, 2008).

1.3.2.3 Protein crystallography workflow

Protein crystallography is a crucial technique in structural biology that enables scientists to unveil the three-dimensional structures of proteins at atomic resolution. This powerful method plays a pivotal role in understanding the functions of proteins and their interactions, paving the way for drug design and disease research.

The protein crystallography workflow typically involves key steps (figure 1.9): protein expression and purification, crystallization, data collection, data processing, model building and refinement. A brief description of each step is reported in this section.

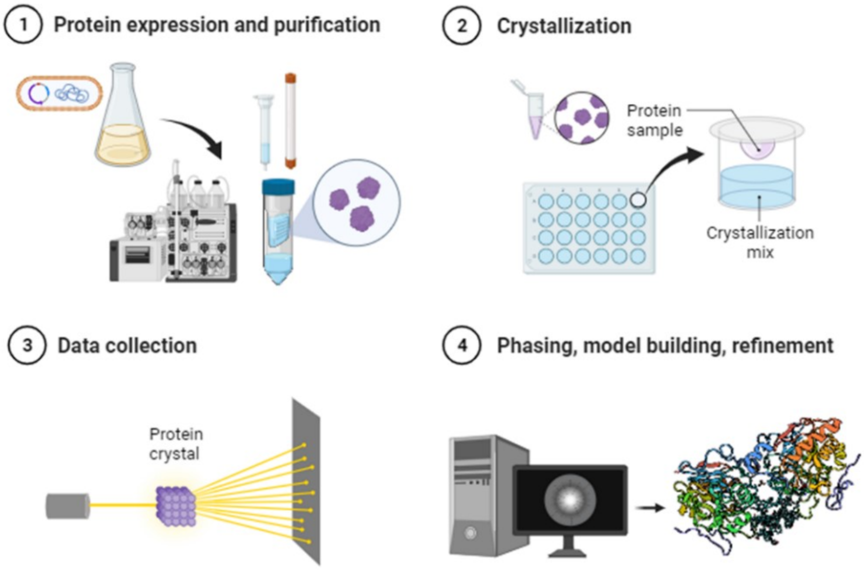

Figure 1.9. Protein crystallography workflow. Step 1 – Protein expression and purification, Step 2 – Crystallization, Step 3 – Data collection, Step 4 – Phasing, model building, refinement. Adapted from "X-Ray Crystallography Structure Determination Workflow", by BioRender.com (2024). Retrieved from https://app.biorender.com/biorender-templates

Step 1- Protein expression and purification: obtaining good quality crystals of the protein of interest is the initial step in protein crystallography. Established molecular biology techniques and several purification steps are employed to obtain sufficient amounts of the protein (in the order of milligrams), aiming for a high purity level of over 95% (Hammond, 2008; Rupp, 2009). Crystallographers commonly rely on Escherichia coli (E. coli) in molecular biology to produce ample protein quantities. This involves cloning the gene responsible for the desired protein into an expression plasmid, where its expression is controlled by an inducible promoter. After transforming the cells with the expression plasmid and inducing protein production, the cells are disrupted chemically or physically, and the protein is purified using several techniques like affinity chromatography. This process often requires several experiments to optimize protein yield (Rupp, 2009).

Step 2- Crystallization: protein crystallization is the process of growing crystals of a purified protein sample. The formation of high-quality protein crystals is a crucial challenge in crystallography and often involves a trial-and-error approach. The process of protein crystallization involves optimizing the conditions under which the protein will form a crystal, including the protein concentration, pH, temperature, ionic strength, and the presence of various chemical agents or precipitants (Rupp, 2009). The goal of crystallization is to create a supersaturated solution, in which the protein concentration is high enough that crystal nucleation and growth can occur. The crystal growth process can be illustrated by a two-dimensional phase diagram (figure 1.10) reporting which states (liquid, crystalline, precipitate) is stable under a variety of crystallization parameters (e.g. concentration of protein, precipitants, additives). A protein solution becomes supersaturated when its concentration is raised over the solubility limit. This zone of the diagram can be divided into three sections depending on the degree of supersaturation: extremely high supersaturation (precipitation zone), where molecules form amorphous aggregates, intermediate supersaturation (nucleation zone) where both growth and nucleation occur, and lower supersaturation (metastable zone), where only growth is supported (Chayen and Saridakis, 2008).

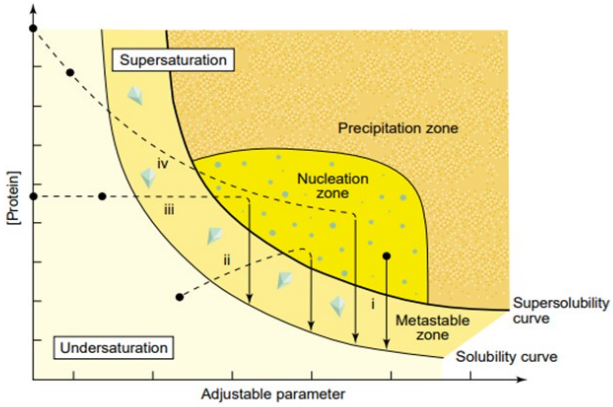

Figure 1.10. Schematic illustration of a protein crystallization phase diagram. The four major crystallization methods are reported: (i) Batch. (ii) Vapour diffusion. (iii) Dialysis. (iv) FID (free-interface diffusion). All these crystallization methods need to reach the nucleation zone and then the metastable zone to produce crystals. The routes to these zones, assuming precipitant concentration as adjustable parameter, are represented (black circles report the starting conditions). The solubility curve represents the condition where concentration of protein in the solution is in equilibrium with crystals. The supersolubility curve line separates conditions in which spontaneous nucleation (or phase separation, precipitation) takes place from conditions in which the crystallization solution stays clear. Adapted from Chayen and Saridakis, 2008.

Among the main techniques for achieving supersaturation the vapour diffusion technique is the most popular for macromolecules crystallization. Vapor diffusion occurs in a closed system and in protein crystallization is used to create a concentration gradient between a drop of protein solution and a reservoir containing a solution of precipitant that promotes crystal formation (Rhodes, 2006; Rupp, 2009). Usually, the drop has a lower concentration of precipitant than the reservoir. By sealing the container to prevent evaporation, the concentration of the protein and precipitant gradually increases in the drop as solvent diffuses from the drop into the reservoir and the sample undergoes an increase in relative supersaturation. As the concentration of the protein and precipitant reaches a critical point, nucleation occurs and crystals begin to form in the drop. Sitting drop/hanging drop vapor diffusion techniques are two kinds of experimentals set-up commonly used due to their simplicity, minimal sample requirement, and the substantial flexibility they offer during the screening and optimization processes. For the crystallization trials reported in this work, we used the classical hanging drop crystallization set-up showed in figure 1.11.

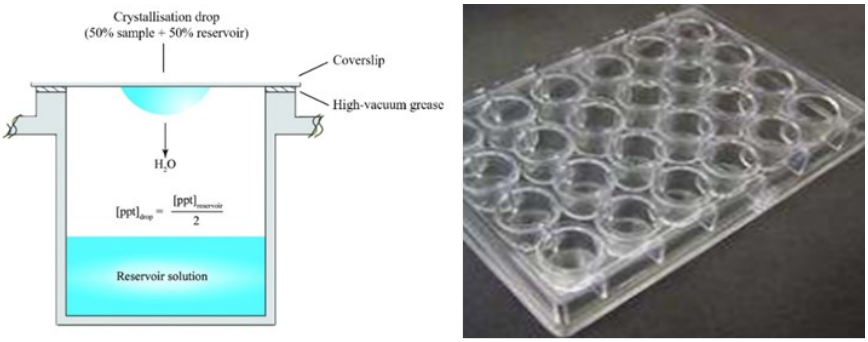

Figure 1.11. Hanging drop crystallization set-up and vapour diffusion process. Hanging drop vapor diffusion is a method commonly used in crystallography and structural biology to grow high-quality protein crystals for X-ray crystallography. In this technique, a small drop of protein solution is suspended from a cover slip over a reservoir solution, allowing it to hang within a sealed container. The drop is composed by half-stock protein solution and half reservoir solution, which contains salt or polymer precipitants in adequate proportions. As the solvent in the drop evaporates over time, the protein concentration increases, and it can lead to the formation of protein crystals within the drop. Adapted from McPherson & Gavira, 2014.

Step 3- Data collection: once suitable crystals are obtained, X-ray diffraction data is collected. Crystals are exposed to X-ray beams, and the resulting diffraction patterns are used to determine the position of atoms in the crystal lattice. The instrument used to record the X-rays diffracted is the X-ray diffractometer whose basic components are an X-ray source, X-ray optics, a goniometer to orient and rotate the crystal and an X-ray detector. All diffractometers used in macromolecular crystallography include a cryocooler that keeps crystals at cryogenic temperature (near liquid nitrogen temperature) to minimize radiation damage. X-rays used in biocrystallography are extremely intense and focused beams. Synchrotrons provide huge amounts of tunable (different wavelengths) X-ray radiation. In an experimental setup, a precisely directed X-ray beam is focused through a crystal, which is positioned on a goniometer head. To prevent non-diffracted X-rays from reaching the detector directly, a beam stop is placed between the crystal and the detector. The detector role is to record both the location and intensity of the diffracted X-ray beams. To aid in precise positioning, a video camera is employed to magnify the crystal, facilitating its alignment within the X-ray beam. To collect a data set, the crystal is suspended in aqueous solution containing a cryoprotectant and mounted on a loop placed at the end of a metal rod attached to a magnetic base (sample pin). The base will magnetically attach to the goniometer head of the diffractometer and the crystal can then be centered in the path of the X-ray beam. The most common data collection technique used in biocrystallography is the rotation method. The crystal is slightly rotated around a single axis by small successive increments during X-ray exposure and during each rotation increment, a diffraction image is recorded. In order to create a three dimensional picture of the crystal, a full data set needs to be recorded and this is done by recording images as the crystal is rotated stepwise through various orientations around three rotational angles, **Ω**, Χ, and Φ. When X-rays interact with electrons in the crystal, they are elastically scattered, generating secondary waves with the same wavelength but different directions (Rhodes, 2006). These scattered waves interfere constructively at a specific point on a circle drawn around the atom that caused the scattering. This point, described by Bragg's Law, appears as a dark spot on the detector. The recorded diffraction data are then subjected to computational analysis. The position and relative intensities of the reflections are used to determine the identity and arrangement of the atoms in the crystal. Each spot (reflection) in the diffraction images is indexed, integrated, merged, and scaled, resulting in a single text file from thousands of images. The intensity is simply a number that indicates how dark the reflection is in comparison to the others. The beam direction is specified by a set of three-dimensional coordinates h, k, and l for each reflection (Rhodes, 2006).

Step 4- Data processing, model building and refinement: this step describe all the computational work that a crystallographer need to undertake to resolve a crystal structure. In data collection, hundreds of images that contain many reflections are recorded. Each reflection has two numerical values associated with it: (1) the amplitude, $|F|$, equal to the height of the wave and (2) the phase, ø, of the diffracted wave, equal to a horizontal shift of the original wave by a displacement factor (Clegg, 2015). These values are represented by vectors and are converted into h, k, l coordinates (Miller indices). An electron density map of the molecule from a diffraction pattern involves the addition of numerous waves with their relative amplitudes and phases. For each reflection, the intensity of the diffracted X-ray beam at each h, k, l position can be measured. The intensity (I_{hkl}) of each measured spot is proportional to the square structure factor amplitude $|F_{hkl}|$ and is as a scalar value (Equation 1.2). The structure factor (Equation 1.1) is a complex number calculated from the amplitudes ($|F|$) and phases ($e^{i\Phi}$) of the diffracted wave and for a unit cell containing n atoms, the structure factor F_{hkl} is the sum of all the atomic fhkl values for individual atoms (Clegg, 2015).

$$\boldsymbol{F}_{\mathrm{hkl}} = |F_{\mathrm{hkl}}| \mathrm{e}^{\mathrm{i}\Phi} = \sum_{j=1}^{n} f_{\mathrm{j}}\, e^{2\pi i(hx_{\mathrm{j}}+ky_{\mathrm{j}}+lz_{\mathrm{j}})} \tag{1.1}$$

$$I_{\mathrm{hkl}} \propto |\boldsymbol{F}_{\mathrm{hkl}}|^2 \tag{1.2}$$

Data processing consists of several steps: 1) spot findings and autoindexing, 2) parameter refinement, 3) integration (measurement of spot intensities), 4) scaling and merging (Clegg, 2015; Powell, 2017). Integration is the process of intensity information extraction from the diffraction spots on the images. The initial step involves identifying a set of spots within a chosen selection of images to facilitate indexing. Throughout the indexing process, a 3D index is derived for each reflection in the dataset, defining them with the three indices h, k, l. Additionally, indexing yields accurate approximations of the crystal unit cell dimensions, its orientation concerning the diffractometer, and offers insights into the crystal symmetry. Another information obtained in this process is the mosaicity, a parameter related to the structure of the crystal that describe its quality. Data reported from the indexing process need to be optimized (parameter refinement step) for accurately locate spots on each image. In the next step of data processing, the integration step, spot intensities are measured. The scaling and merging process aligns the measured intensities onto a unified scale, accounting for imperfections in the experiment and combining 'symmetry-related' measurements. This step provides the initial reliable assessment of the data collection quality and resolution, as well as the data processing, offering valuable insights into the crystal true symmetry (Powell, 2017). Data reduction produces a list of h, k, l indices with their corresponding observed structure amplitude, $|F_{hkl}|$, and the error, σ (F_{hkl}), associated with the amplitude. Using this information an electron density map can be created and conversion of the list of h, k, l reflection positions into atom positions in x, y, z coordinates can be performed using equation 1.3:

$$\rho_{x,y,z} = \frac{1}{V}\sum_{hkl} |F_{\mathrm{hkl}}|\, e^{-2\pi i[(hx+ky+lz)-\phi_{\mathrm{hkl}}]} \qquad (1.3)$$

The electron density, $\varrho_{x,y,z}$ (in electrons per Å^3) is equal to the summation of the observed structure amplitudes multiplied by the phases of the waves from all of the reflections (h,k,l), multiplied by an extra phase correction (Clegg, 2015). The amplitudes are measured, and the phase correction can be calculated. Contrary to this, the phase cannot be directly recorded during the experiment or calculated using the information obtained in the data collection. The conversion of the crystal reciprocal space representation into an interpretable electron density map is known as 'phasing', and it represents a fundamental challenge in crystallography ('the phase problem') (Clegg, 2015). Crystallographers employ various methods to overcome this phase problem and recover phase information from diffraction data, including direct methods, molecular replacement, anomalous X-ray scattering, and multiple isomorphous replacement (Clegg, 2015).

Once initial phases are determined the initial structural model undergoes an iterative optimization process. During refinement, various parameters such as atomic coordinates, thermal vibrations, and occupancies are adjusted to minimize the disparity between the calculated and observed diffraction data. This process fine-tunes the model, ensuring that it is in optimal agreement with the experimental results. Iterative cycles of refinement, aided by mathematical algorithms and statistical analyses, contribute to enhancing the precision of the structural model.

There are several geometrical and statistical parameters used to assess the final protein structure quality and its link to data quality (Acharya and Lloyd, 2005; Karplus and Diederichs, 2012), including for example the resolution, redundancy, Rmerge, or the Rfactor (or simply R), Rfree, real-space correlation coefficients, Ramachandran violations, and others. Among these, the Rmerge is a statistical measure of how well the X-ray diffraction data scale together, while the redundancy (or multiplicity) is the average number of times each unique reflection is recorded. The Rfactor, defined as Σ|Fobs – Fcalc| / ΣFobs (equation 1.4), combines the error inherent in the experimental data and the deviation of the model from reality.

$$R = \frac{\Sigma|F_o - F_c|}{\Sigma|F_o|} \qquad (1.4)$$

It is typically expressed as a percentage, and the lower is, more accurate the model. Well-refined macromolecular structures are expected to have a Rfactor < 20%. The Rfree is calculated analogously to the Rfactor, but for only a (selected) fraction of reflections (e.g., 5% or 10% of them). Rfree is an important validation parameter and should set a warning if it exceeds R by more than ~ 7%, which may indicate over-fitting of the experimental data, or may result from structural model defects. The parameter rmsd from standard stereochemistry indicates how much the model departs from geometrical parameters that are considered typical. Good-quality structures are expected to have for example a rmsd(bond) of ~0.02 Å. The Ramachandran plot is a plot of angles around the rigid peptide bond (f–j) compared with those most favoured for protein structural elements.

1.4 Aim of the research

While our understanding of the ECS has significantly advanced, there is still much to learn about its intricate mechanism of regulation. Crystallographic studies have played a crucial role in providing structural insights into receptors (Hua et al., 2016; Li et al., 2019) and enzymes (Bracey et al., 2002, Bertrand et al., 2010; Magotti et al., 2015) of the ECS, including their interactions for ligand discovery and design (Mileni et al., 2008; Castellani et al., 2017; Xing et al., 2020; Li et al., 2023). Recently, our group has focused the attention on the human membrane enzyme NAPE-PLD that plays a key role in the direct biosynthesis of NAEs from NAPEs.

We solved the crystal structure of human membrane NAPE-PLD at resolution of 2.6 Å providing valuable insights into its catalytic mechanism and substrate binding (Magotti et al., 2015). The crystal structure has helped in understanding the molecular basis of NAPE-PLD role in endocannabinoid synthesis and regulation. X-ray diffraction analysis and molecular biophysics studies have revealed not only the mechanism of lipid amide biogenesis, but unexpectedly specific binding sites for bile acids, the natural detergents secreted by the liver to aid the digestion of dietary fats in the intestine. We demonstrated that the membrane enzyme is turned on by the interaction with bile acids, which act as structural cofactors at membrane interface (Margheritis et al., 2016). The unique protein dimer architecture of NAPE-PLD and the structural determinants of bile acid binding offer targets for pharmacological modulation. However, our understanding of its modulation and the potential of drug discovery targeting NAPE-PLD is limited by the lack of structural information of this membrane protein in complex with specific ligands.

My PhD research work aims to provide a structural and functional investigation of the human protein target NAPE-PLD in complex with small molecule modulators. These compounds might be useful to control the NAEs lipid signaling in diseases and might have therapeutic potential in several metabolic and neurological disorders.

In this work, we combined approaches of fragment- and small molecule-screening by SPR, with X-ray crystallography and synthetic chemistry. We successfully identified different ligands measuring their binding affinity and kinetics, characterizing for some of them their interactions with NAPE-PLD at atomic resolution. These are the first structures of the membrane-associated enzyme with synthetic compounds. Among these, the hydrochlorothiazide is one of the preferred and most used drugs in clinic for essential hypertension.

Chapter 2

Experimental methods

In this chapter the sample production methods and the experimental setups are reported.

2.1 Protein expression and purification

All reagents for protein expression and purification were purchased from Merck (Merck Millipore, Darmstadt, Germany) unless otherwise indicated. Protein expression and purification was performed as described before (Magotti et al. 2015; Margheritis et al. 2016). The region encoding a truncated protein form (Δ47) from the amino acid D47 to F393 was amplified and inserted into the expression vector pMAL c5x (New England Biolabs, Ipswich, MA, USA). The cloned gene in a pMAL™-5 vector is inserted downstream from the malE gene of E. coli, which encodes maltose-binding protein (MBP), resulting in the expression of an MBP fusion protein (Guana et al., 1988). The vector carries the lacI^q gene, which encodes for the Lac repressor that acts as a lactose sensor. It blocks generally transcription of the operon but in presence of lactose, it stops acting as a repressor and triggers transcription of the operon. Isopropyl β-D-1-thiogalactopyranoside (IPTG) is a molecular mimic of allolactose (an isomer of lactose, formed when lactose enter the cells) and it is used to induce *E.coli* protein expression when the gene is under the control of lac operator (Donovan et al, 1996). The pMAL-c5X vector also includes in the system encode the site for Factor Xa, a specific protease that allows MBP to be cleaved from the protein of interest (Nagai, 1987). For this work, the resulting vector harboring the gene of interest was transformed into E.Coli RosettagamiB (DE3) pLysS cells (Novagen, Merck Millipore, Darmstadt, Germany) to produce the encoded recombinant protein with an N-terminus MBP tag and a C-terminus hexahistidine tag. The large-scale purification for NAPE-PLD was performed inoculating 1 litre of Luria Broth (LB) medium with 5 ml of cell culture grown overnight at 37°C with 230 rpm shaking, in the presence of 50 μg/mL ampicillin, 17μg/mL chloramphenicol and 0.2% (v/v) glucose. Cells were first grown at 37°C to an optical density (OD_{600nm}) of 0.6-0.8 and protein expression was induced with 0.25 mM IPTG (Thermo Fisher Scientific, Waltham, MA, USA). After incubation for 16 h at 28°C, bacteria were harvested by centrifugation (4000 rpm, 20 min, 4°C, Beckman Avanti centrifuge, Beckman Coulter Inc, CA, USA) and frozen at -20°C. Cells were then thawed and resuspended in ice cold lysis buffer (20 mM Tris-HCl pH 8.0, 200 mM NaCl, EDTA-free protease inhibitor cocktail) in the presence (0.1% w/v) or absence of DCA. The lysis was performed in ice-bath by sonication (80% power for 5 min with a frequency of 1 pulse per second, Sonopuls Bandelin electronic, Berlin, Germany). The bacterial lysate was incubated with 5 μg/ml DNAseI and 1% (v/v) Triton X100 at 4°C for 1 hour and then was clarified by centrifugation (11000 rpm, 1h, 4°C, Beckman Avanti centrifuge, Beckman Coulter Inc, CA, USA). Cell lysates were sterile filtered through 0.22 μm filters and mixed with 5 mL of Amilose Sepharose resin (New England Biolabs, Ipswich, MA, USA). The resin was previously poured in a 2.5 x 10 cm column, washed with 5 column volumes (CV) of distilled water and equilibrated with 5 CV of column buffer (20 mM Tris pH 8.0, 200 mM NaCl) in presence (0.1% w/v) or absence of DCA. The loaded resin was incubated on a tube rotator for 4h at 4 °C, washed with 12 CV of column buffer and eluted using the column buffer added with 10 mM maltose. The MBP-tagged protein was then incubated with 1U/mg of eluted protein of the protease Factor Xa (FXa, Canvax Biotech, Cordoba, Spain) for 16 h at r.t to cleave the MBP fusion tag. Further purification steps were performed using ÄKTA™ fast protein liquid chromatography (FPLC) system (ÄKTA™ express, Cytiva, Marlborough, MA, USA). After the FXa cleavage, the protein with the C-terminus six-histidine tag was passed in HisTrap™ column previously washed with 5 CV of distilled water, and then equilibrated with 5 CV of binding buffer (20 mM Tris pH 8.0, 200 mM NaCl) in presence (0.1% w/v) or absence of DCA. Fractions corresponding to the flowthrough containing the MBP-fusion tag were collected and the column was then washed with binding buffer until the absorbance reached a steady baseline. Bound NAPE-PLD was eluted using a linear gradient from 0 to 100% of elution buffer (20 mM Tris pH 8.0, 200 mM NaCl, 500 mM imidazole) in presence (0.1% w/v) or absence of DCA. The final purification steps were performed by gel filtration size exclusion chromatography (GFSEC). The NAPE-PLD-containing fractions were pooled, concentrated using a centrifugal filter with a 50 KDa cut-off before being injected onto a Superdex 200 Increase 10/300 GL column (Cytiva, Marlborough, MA, USA) and eluted with gel filtration buffer (20 mM Tris pH 8.0, 200 mM NaCl) in presence (0.1% w/v) or absence of DCA. All the fractions collected during purification were analyzed by SDS-PAGE and only fractions with at least 95% protein purity were pooled together. Protein concentration for further analysis was estimated by measuring the UV absorbance at 280 nm with JASCO V-550 spectrophotometer (JASCO, Tokyo, Japan).

DCA is a water-soluble bile salt derivative with numerous applications in biochemistry and structural biology. Its notable ability to solubilize and extract membrane proteins addresses the challenge of purifying these proteins, which tend to aggregate due to their hydrophobic nature in aqueous solutions (Seddon et al., 2004). Acting as a detergent, sodium deoxycholate disrupts lipid-protein interactions and solubilizes the lipid bilayer, facilitating the release of membrane proteins into solution. This property makes it a valuable tool for isolating and studying membrane proteins across various biological samples (Choy et al., 2021). Additionally, DCA is often used with other detergents to enhance solubilization and maintain protein stability.

Previous studies by our group have highlighted the role of bile acids in stabilizing and modulating NAPE-PLD (Magotti et al., 2015; Margheritis et al., 2016). In this study, we maintained the presence of the detergent in all preparations involved in crystallization trials for X-ray structure determination of the protein in complex with ligands. The detergent protein solubilization and stabilization properties ensured a high protein yield and purity, essential for obtaining quality crystals.

Furthermore, protein samples purified in the presence or absence of DCA were used for binding assays via surface plasmon resonance to evaluate the modulation of protein-ligand binding by bile acids.

2.2 Surface Plasmon Resonance

2.2.1 Experimental setup for binding analysis

All the SPR experiments in this work were performed using a fully automated, three channel, surface plasmon resonance-based biosensing system, the SensiQ Pioneer 300 (ICx Technologies, Arlington, VA, USA), equipped with an Octet® SPR PCH sensor chip (Sartorius, Gottinga, Germany). SPR sensor chips can be classified based on several factors, including their immobilization matrix (2D or 3D), binding capacity, and the type of bond formed with the ligand. In 2D-planar sensors, functionalizations are directly linked to the gold layer, resulting in a flat surface without a matrix. This design allows for a lower binding capacity, making it suitable for studying interactions involving large molecules and molecular complexes. On the other hand, 3D sensors feature a matrix between the gold surface and the functionalizations, offering expanded surface area and increased capacity for binding compounds (Schasfoort, 2017). The PCH sensor chip has a high-capacity three-dimensional surface characterized by a non-dextran linear polycarboxylate hydrogel layer. These features make this type of sensor chip useful for studies involving analytes as small molecules and fragments. The SPR chip was functionalized with biotinylated NAPE-PLD, immobilized to the gold surface via the capturing molecule NeutraAvidin™ (immobilization by affinity capture strategy). NeutrAvidin™ was immobilized on the chip surface using the standard amine coupling chemistry. Protein sample was minimally biotinylated (Papalia and Myszka, 2010) on ice for 3h using an equimolar concentration of sulfo-NHS-LC-biotin (Thermo Fisher Scientific) and passed through a Superdex 200 Increase 10/300 GL (Cytiva) gel filtration column (buffer 20 mM HEPES pH 8.0, 200 mM NaCl, 0.1% w/v sodium deoxycholate) to remove the excess of free biotin. Protein solution was buffer-exchanged by centrifuge filtration (buffer 20 mM Tris pH 8.0, 200 mM NaCl). The entire immobilization step was performed in sodium acetate buffer SA_{10} (10 mM sodium acetate pH 5.0) at a flow rate of 20 μL/min and a temperature of 25 °C. SA_{10} was initially flowed along the SPR chip surface for 5 min. The surfaces of all three flow cells of the SPR system were activated for 7 min with a 1:1 mixture of 100 mM NHS (N-hydroxysuccinimide) and 200 mM EDC (3-(N,N-dimethylamino) propyl-N-ethylcarbodiimide). After surface activation, NeutrAvidin™ at a concentration of 1 mg/ml in SA_{10} was injected for 15 minutes to covalently attach the protein to the activated carboxylic groups of the chip surface (immobilization). Short injections of SA_{10} and PBS_{NaCl} (Phosphate Buffered Saline high concentration of NaCl, 750 mM NaCl, 10 mM Na_2HPO_4, 1.8 mM KH_2PO_4, 2.7 mM KCl) were performed to remove the non-covalently bound NeutrAvidin™, then 1 mM aqueous ethanolamine pH 8.0 was pumped along the surface for 5 min at a flow rate of 20 µl/min to deactivate the remaining carboxyl groups. This coupling method resulted in a density ~10,000 RU of NeutrAvidin™ on all flow cells. At the end of the NeutrAvidin™ immobilization, a run with running buffer was performed by switching to Tris buffer (20 mM Tris pH 8.0, 200 mM NaCl). Biotinylated NAPE-PLD at a concentration of 10 µM in running buffer was then injected for 10 min at a flow rate of 20 µl/min on flow cells 2 and 3 to densities of ~2000 RU, leaving flow cell 1 unmodified as a reference surface. The stability of the surface was demonstrated by the flat baseline achieved at the beginning of each sensorgram. For kinetic analysis, commercial and synthetized compounds, dissolved in running buffer, were tested for binding to NAPE-PLD using two experimental methods: standard multiple injection method and OneStep® kinetics. In the standard multiple injection method setup, experiments were performed with 5 concentrations of each analyte being studied, ranging from 0 µM to 250 µM. OneStep® Injections setup allows determining the kinetic and affinity parameters of a binding interaction using only a single sample of known concentration of analyte and one injection. This method, based on Taylor dispersion (Quinn, 2012), produces a sigmoidal concentration gradient of analyte in the capillary fluidic line. The top concentration of each analyte used for One step® experiment was 500 µM. As an internal control for the gradient dispersion process, an injection of 3% sucrose prepared in the same buffer as used for the analyte and running buffer is performed at least once in each OneStep® assay to ensure proper gradient formation is occurring and to calibrate for buffer viscosity. All SPR assays were carried out in Tris buffer. DCA injections was used as positive control. Prior to performing the assay, solutions were sterile filtered. All the experiments measurements were carried out at 25°C in triplicate. Each analyte injection was repeated three times and the responses are all overlaid to check the reproducibility of binding responses. Formation of the complex between NAPE-PLD and ligands was indicated by the increase in resonance units (RUs) relative to baseline upon injection of each compound at each concentration.

2.2.2 SPR Data Processing

The response data were processed in QDAT analysis software (SensiQ Technologies, Inc., Oklahoma City, OK, USA) using a reference surface to correct for any bulk refractive index changes and blank injections for double referencing (Myszka, 1999). The binding profiles were fit globally to a 1:1 (A + B = AB) or 1:2 (A + 2B = AB1 + AB2) binding model.

2.3 Synthesis of pyridoxal-5'-phosphate analogues

2.3.1 Chemistry

General Information. All solvents and chemicals were purchased from Sigma-Aldrich and used without further purification. Silica gel 60 RP-18 F_{254}s aluminium sheets (Merck, Darmstadt, Germany) were used in analytical thin-layer chromatography (TLC). LC chromatographic separation was performed on a Dionex preparative purification system. Evaporation was performed in vacuo (rotating evaporator). ^{1}H and ^{13}C NMR spectra were obtained on a Bruker Avance III 300 spectrometer (Bruker, Billerica, MA, USA) at 300 MHz in a solution of deuterium oxide (D_2O). Chemical shifts (δ) are reported in parts per million (ppm) from low to high field relative to residual solvent. Multiplicities are given as: singlet (s), doublet (d), triplet (t), doublet of doublets (dd), and multiplet (m). All synthetic compounds exhibited >95% purity, as determined by LC−MS analysis performed using a Kinetex PFP column (100 × 3.00 mm, 2.6 μm total particle size, 100 Å pore size) (Phenomenex, Torrance, CA, USA) on an Shimadzu Nexera UHPC (Shimadzu, Nakagyo-ku, Kyoto, Japan) high performance liquid chromatography system equipped with a diode array detector and interfaced with an ABSciex API 3200 QTRAP electrospray ionization (ESI) mass spectrometer (AB Sciex LLC, Framingham, MA, USA) run in the positive mode with a scan range of 100−1100 m/z. Liquid chromatography was carried out at a flow rate of 0.5 mL/min at 20 °C with a 5 µL injection volume, using the gradient elution with aqueous acetonitrile. The mobile phase consisted of (A) water with 10 mM ammonium acetate pH 8.0 and (B) acetonitrile/A (95:5). The gradient was adjusted based on the different polarities of different compounds.

2.3.2 General procedure for the synthesis of compounds 1-4

The compounds were synthetized according to the previously reported procedures with some modification (Ikawa, 1967; Rudd et al., 1979; Iskander et al., 1991). Pyridoxal-5'-phosphate (1 eq) were dissolved in methanol containing KOH (2 eq). To the resulting yellow solution, a mixture of the starting amine in methanol containing KOH (2 eq) was added dropwise. After the addition, the reaction mixture was stirred for an additional 30 min at room temperature, then sodium borohydride (1 eq) was added portion-wise at 0°C. The reaction mixture was stirred for further 10 min, then quenched by dropwise addition of water and concentrated *in vacuo*. The crude product was purified by liquid chromatography (RP-PFP column, 10 mM ammonium acetate pH 8.0 - acetonitrile gradient elution, gradient adjusted based on the different polarity of different compounds). The correct fractions were combined and concentrated to dryness *in vacuo* to provide the corresponding reductive amination product with >95% purity (Scheme 2.1).

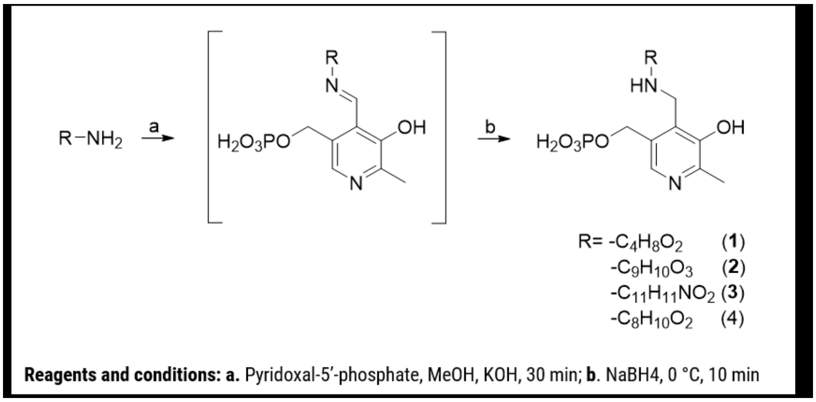

Scheme 2.1. General procedure for the synthesis of compounds 1-4

4-(((3-hydroxy-2-methyl-5-((phosphonooxy)methyl)pyridin-4-yl)methyl)amino)butanoic acid (1)

Reaction of gamma-amino-butyric acid with pyridoxal-5'-phosphate yielded 1 as a white solid (95%);^{1} H NMR (300 MHz, D_2O) δ 7.58 (s, 1H), 4.70 (s, 2H), 4.30 (s, 2H), 3.04 (t, *J* = 7.5 Hz, 2H), 2.39 (s, 3H), 2.21 (t, *J* = 7.3 Hz, 2H), 1.89 (m, 2H). ^{13}C NMR (75 MHz, D_2O) δ 175.95, 148.40, 147.64, 137.95, 131.85, 130.00, 63.35, 48.04, 46.07, 32.49, 24.61, 18.54. Mass spectrum (*m/z*), 335.04 $[M + H]^+$.

((3-hydroxy-2-methyl-5-((phosphonooxy)methyl)pyridin-4-yl)methyl)tyrosine (2)

Reaction of L-tyrosine with pyridoxal-5'-phosphate yielded 2 as a white solid (93%); ^{1}H NMR (300 MHz, D_2O) δ 7.54 (s, 1H), 7.02 (d, *J* = 9.0 Hz, 2H), 6.72 (d, *J* = 6.0 Hz, 2H), 4.70 (s, 2H), 4.20 (m, 2H), 3.80 (dd, *J* = 9.0, 6.0 Hz, 1H), 3.15 (dd, *J* = 15.0, 3.0 Hz, 1H), 2.96 (dd, *J* = 15.0, 6.0 Hz, 1H), 2.28 (s, 3H). ^{13}C NMR (75 MHz, D_2O) δ 154.39, 143.80, 134.59, 131.17, 130.45, 127.08, 116.11, 74.74, 63.90, 62.91, 61.46, 45.11, 34.84, 22.95, 14.70. Mass spectrum (*m/z*), 413.0 $[M + H]^+$.

((3-hydroxy-2-methyl-5-((phosphonooxy)methyl)pyridin-4-yl)methyl)tryptophan (3)

Reaction of L-tryptophan with pyridoxal-5’-phosphate yielded 3 as a white solid (47%); ^{1}H NMR (300 MHz, D2O)   7.33 (t, *J* = 9.0 Hz, 1H), 7.25 (s, 1H), 7.13 (t, *J* = 7.5 Hz, 1H), 7.03 (s, 1H), 6.96 (m, 2H), 4.70 (s, 2H), 4.44 (dd, *J* = 12.0, 3.0 Hz, 2H), 3.86 (dd, *J* = 9.0, 3.0 Hz, 1H), 3.38 (dd, *J* = 15.0, 3.0 Hz, 1H), 2.99 (dd, *J* = 15.0, 12.0 Hz, 1H), 1.82 (s, 3H). ^{13}C NMR (75 MHz, D_2O) δ 181.46, 173.77, 144.02, 136.33, 134.38, 134.16, 130.36, 125.85, 125.59, 121.96, 119.31, 117.80, 111.69, 107.29, 61.74, 43.09, 26.83, 23.24, 15.06. Mass spectrum (*m*/*z*), 435.8 $[M + H]^+$.

(4-(((3,4-dimethoxyphenyl)amino)methyl)-5-hydroxy-6-methylpyridin-3-yl)methyl dihydrogen phosphate (4)

Reaction of 3,4-dimethoxyaniline with pyridoxal-5’-phosphate yielded 4 as a white solid (80%); ^{1}H NMR (300 MHz, D2O) δ 7.67 (s, 1H), 6.88 (d, *J* = 6.0 Hz, 1H), 6.61 (s, 1H), 6.50 (s, 1H), 4.70 (s, 2H), 4.40 (s, 2H), 3.76 (s, 6H), 2.41 (s, 3H). ^{13}C NMR (75 MHz, D2O) δ 160.23, 148.92, 143.06, 142.09, 141.86, 137.97, 134.24, 125.36, 113.48, 113.38, 107.46, 101.68, 61.60, 56.33, 55.67, 41.96, 15.40. Mass spectrum (*m*/*z*), 385.0 $[M + H]^+$.

2.4 X-ray crystallography

2.4.1 Improving crystal growth: seeding

Obtaining high-quality protein crystals can be a challenging and time-consuming process, and it often requires extensive optimization and trial-and-error. Crystal seeding is a technique used in protein crystallization to promote the growth of high-quality protein crystals by adding homogeneous or heterogeneous crystals to a crystallizing solution allowing growing crystals in the metastable zone (Bergfors, 2003). In this study, we employed the streak-seeding method, a type of microseeding technique, to obtain larger and better diffracting crystals. Microseeding involves the transfer of microscopic crystals from a seed source to a no nucleated protein solution (Stura & Wilson 1990). Our approach to generating the microseed stock is a modified version of the method pioneered by D'Arcy et al. (2007), originally derived from the work of Luft and DeTitta (1999).

Outlined below is the protocol we followed for preparing crystal seeding samples:

1. Begin by identifying the suitable crystals in the crystallization plate under the microscope. Open the drop well and delicately crush the crystals using a probe.

2. Extract approximately 4 µl of reservoir solution from the reservoir and transfer it to the coverslip containing the crushed crystals. Thoroughly mix the contents by pipetting and transfer the mixture to a test tube chilled on ice.

3. Repeat the previous step until all crushed crystals have been transferred, resulting in approximately 24 µl of solution containing

crushed crystals in the tube. Ensure that no crystals are left adhering to the well by inspecting the coverslip after each transfer.

4. Centrifuge the tube and use the undiluted seed stock for streak seeding. To streak seed, immerse a clean cat cat whisker into the seed stock and carefully run it through the drop, starting from outside the drop and ending outside in a single smooth motion. Seal the drop to prevent evaporation.
5. Immediately after use, store the undiluted seed stock at -20 °C for future applications.

The newly formed crystals predominantly emerged along the path traced by the whisker through the drop, demonstrating the efficacy of seeding as a growth surface for crystals (Bergfors, 2003).

2.4.2 Crystallization of NAPE-PLD-ligand complexes

Human recombinant NAPE-PLD was produced as described before (Magotti et al., 2015, Margheritis et al., 2016). Prior to crystallization, the protein solution was concentrated in the elution buffer with centrifugal filter devices to ~60 mg/ml. Complexes were obtained by adding the solubilized selected ligand to the concentrated protein solution up to a final concentration of 0.1-10 mM. Co-crystallization experiments were performed using the hanging drop vapor-diffusion method in a 24-well plate at r.t. Crystallization drops were formed mixing 1 μL protein/ligand solution with 1 μL well solution. Small crystals appeared the day after in 1.0 M litium sulfate, 0.1 M Tris HCl pH 8 and they were used for seeding as described above to induce nucleation and better crystal growth. A screening of different crystallization condition was performed varying precipitant concentration and pH of the buffer. Crystals suitable for data collection grew from 0.8-1.2

M litium sulfate, 0.1 M Tris HCl pH 8. Best diffracting crystals grew from the drops with 0.9 M and 1.0 M of precipitant. Before X-ray data collection at cryogenic temperature (100 K), crystals were cryoprotected in mother liquor containing glycerol (20-25% v/v) and the selected ligand, and subsequently flash-cooled in liquid nitrogen for the diffraction experiments.

2.4.3 Data collection, structure determination and refinement for X-ray diffraction

Data collections were acquired on the DECTRIS PILATUS 6M detector at the beamline XRD2 of the synchrotron light source ELETTRA (Trieste, Italy). Diffraction images were indexed, integrated, and scaled using the CCP4i programs package (Agirre et al., 2023). The phase problem was solved by the method of molecular replacement using the PHENIX programs package (McCoy et al., 2007; Adams et al., 2010) starting from the atomic coordinates of the native protein structure having PDB ID accession number: 4QN9 (https://www.rcsb.org). The structures of the ligand complexes were refined by cycles of automatic and manual building and analyzed using COOT (Emsley et al., 2010) and the PHENIX programs package. The complexes were prepared with the software PyMol (www.pymol.org). The atomic coordinates and structure factors have been deposited in the Protein Data Bank (NAPE-PLD with HCTZ, accession code 8PC4; NAPE-PLD with PLP, accession code 8P90; NAPE-PLD with N3SA, accession code 8P96).

Chapter 3

Results

In this work, we focused on the structural and functional characterization of the human protein target NAPE-PLD in complex with small molecule ligands. We performed a wide screening of low molecular weight ligands by SPR. We selected the best hits showing the highest affinities and crystallized the membrane-associated enzyme in the presence of these potential ligands.

3.1 Surface Plasmon Resonance as a tool for ligand binding investigation of NAPE-PLD

3.1.1 Identification of protein-ligand interactions by binding kinetics studies

In this study, we employed SPR for ligand screening to identify potential modulators for NAPE-PLD. From a library of the Italian Institute of Technology containing commercially available compounds, we selectively chose fragments (with a molecular weight < 350 Da) and a diverse range of approved drugs to assess their ability to bind efficiently and stabilize the target. In all SPR experiments, we adopted a ligand capture approach to immobilize NAPE-PLD onto the sensor chip surface. This method involves the non-covalent capture of the ligand using a capture reagent typically covalently linked to the chip surface, resulting in the reversible binding of the ligand to the capture reagent. For this purpose, we utilized biotin as an affinity tag to facilitate ligand binding to a NeutrAvidin™-coated chip surface.

NeutrAvidin™, a deglycosylated avidin protein with a molecular weight of 60 kDa, contains four identical biotin subunits with high affinity for biotin (K_D = 10^{-15} M) (Green, 1963). It has a near-neutral isoelectric point (pI=6.3) and exhibits the lowest non-specific binding among known biotin-binding proteins (information obtained from Pierce, Rockford, IL, USA). NeutrAvidin™ was covalently attached to the chip surface using carbodiimide chemistry, and a minimally biotinylated NAPE-PLD (Papalia and Myzska, 2010) was flowed onto the surface for ligand capture.

In the initial step of ligand screening, we conducted all binding experiments using the SensiQ Pioneer OneStep® injection method, essentially employing Taylor dispersion to create a gradient injection for the quantification of biomolecular interactions (Quinn, 2012). In the Taylor dispersion method, the analyte concentration starts uniformly and gradually transforms into a sigmoidal gradient due to the combined effects of analyte diffusion and convective laminar flow within the dispersion capillary (Quinn, 2012). This method not only saves sample preparation time and reduces assay complexity but was also chosen for the ligand screening phase because, unlike the standard fixed concentration method, it allows the analyte to flow continuously over the surface in a slow gradient, equivalent to thousands of standard injection dilutions (Quinn, 2012). A panel of approximately 50 commercially available and pharmacologically active compounds (MW 200-400 Da) was screened at a single concentration, up to 500 μM, leading to the identification of three molecules, pyridoxal-5'-phosphate (PLP), hydrochlorothiazide (HCTZ), and 1,3,(6-7)-naphthalenetrisulfonic acid (N3SA) (Table 3.1), exhibiting the best binding kinetics parameters among all the screened compounds.

Table 3.1. Chemical structures, names, molecular weights and molecular formulas of investigated compounds.

Name	**Chemical Structure**	**Molecular Formula**	**Molecular Weight (g/mol)**	**Abbreviation**
Pyridoxal-5'-phosphate	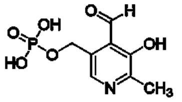	**$C_8H_{10}NO_6P$**	**247,14**	**PLP**
Hydrochlorothiazide	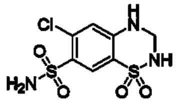	**$C_7H_8ClN_3O_4S_2$**	**297,73**	**HCTZ**
1,3,(6,7)-Naphthalenetrisulfonic acid trisodium salt	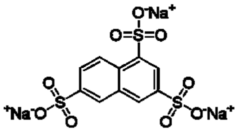	**$C_{10}H_5Na_3O_9S_3$**	**434,31**	**N3SA**

Each analyte was injected in triplicates and the resulting data were fitted using both a 1-site (1:1) and a 2-site (1:2) interaction model (Figure 3.1) to determine the binding constants (Table 3.2). The simple 1:1 model simultaneously fits the rate constants of association and dissociation and estimates binding affinity. The biomolecular interaction between a soluble analyte (A) and an immobilized ligand (B) can be interpreted in terms of pseudo-first-order kinetics, where the rate of complex formation is described by the following differential equation (QDAT user manual, Pioneer):

$$\frac{\mathrm{dAB}}{\mathrm{dt}} = k_a * \mathrm{A(t)} * \mathrm{B} - k_d * \mathrm{AB(t)}$$

$$\mathrm{AB}(0) = 0 \tag{3.1}$$

where:

AB(t) = molar concentration of complex at the interaction surface at time t
A(t) = molar concentration of analyte at the interaction surface at time t
B = molar concentration of available immobilized ligand
k_a = association rate constant ($M^{-1}s^{-1}$)
k_d = dissociation rate constant (s^{-1})

During the SPR experiments, we could monitor these surface interactions in real-time, where the rate of change of response is directly related to the formation of complex AB. Equation 3.1 can be rewritten in terms of response as:

$$\frac{\mathrm{dR}}{\mathrm{dt}} = k_{\mathrm{a}} * \mathrm{A(t)} * \mathrm{R_{max}} - k_{\mathrm{d}} * \mathrm{R(t)}$$

$$\mathrm{R}(0) = 0 \tag{3.2}$$

where:

t = biosensor response at time t
$\mathrm{R_{max}}$ = maximum response if all available ligand binding sites are occupied

This model is applicable to both fixed-concentration and time-varying concentration injections. The QDAT analysis software also allows the model to fit for multiple independent binding sites. While the 1-site fitting model is generally suitable for most SPR sensograms, other factors such as steric hindrance, or rebinding might be better represented by a 2-site model. We chose to report both fittings (Figure 3.1) to show how data obtained at high analyte concentrations could be better fitted using a 2-site model.

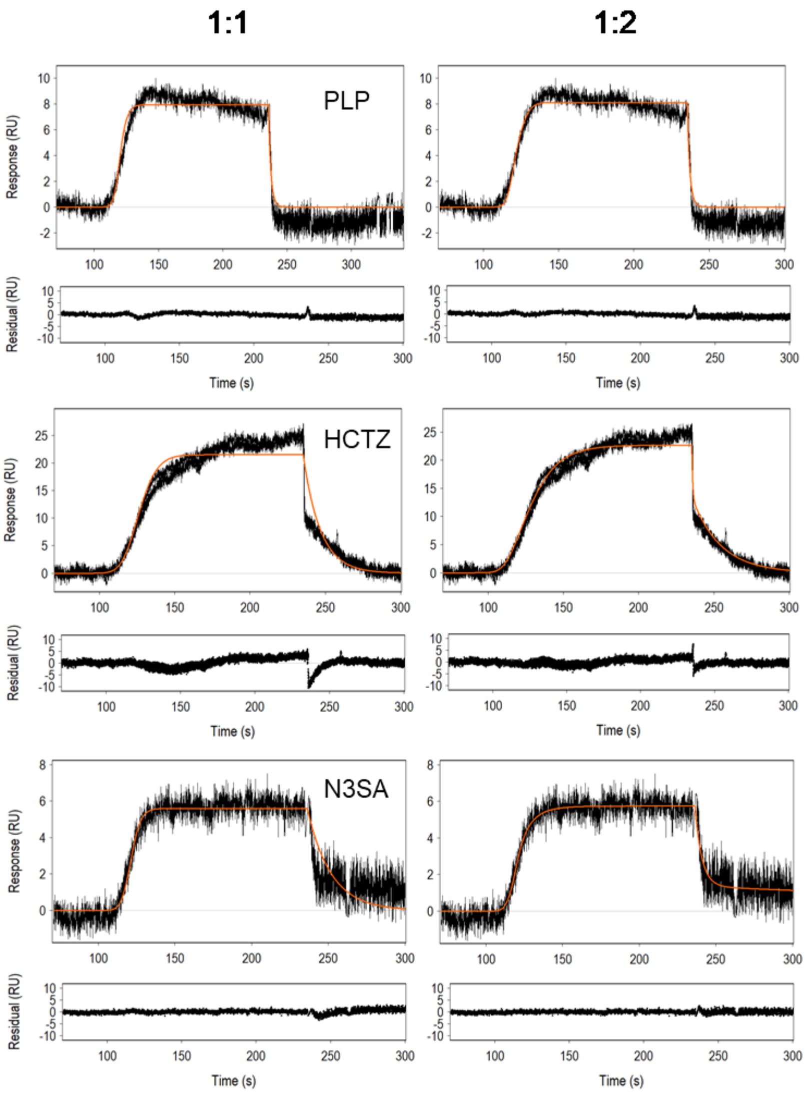

Figure 3.1. SPR analysis of novel ligands interacting with NAPE-PLD. Representative OneStep kinetics response profiles (and their replicates) for the three selected ligands, PLP, HCTZ and N3SA against NAPE-PLD, determined at 25 °C using surface plasmon resonance. The orange lines show global kinetic analysis of data with a 1:1 Langmuir model (left panel) and 1:2 model (right panel) for binding. The concentration range tested is 0-500 µM. The related residual plot is given below each sensorgram data set. The standard deviation of the residuals (resSD) for the reported representative data set for PLP are 0.98 RU and 0.94 RU for the 1:1 and 1:2 fitting, respectively. ResSD for the reported experimental data set for HCTZ are 1.64 RU and 1.11 RU for the 1:1 and 1:2 fitting, respectively. Finally, ResSD for the reported experimental data set for N3SA are 0.80 RU and 0.64 RU for the 1:1 and 1:2 fitting, respectively. The kinetic parameters obtained from each interaction are reported in Table 3.2.

Table 3.2. Affinity and rate constants for NAPE-PLD/ligand interactions

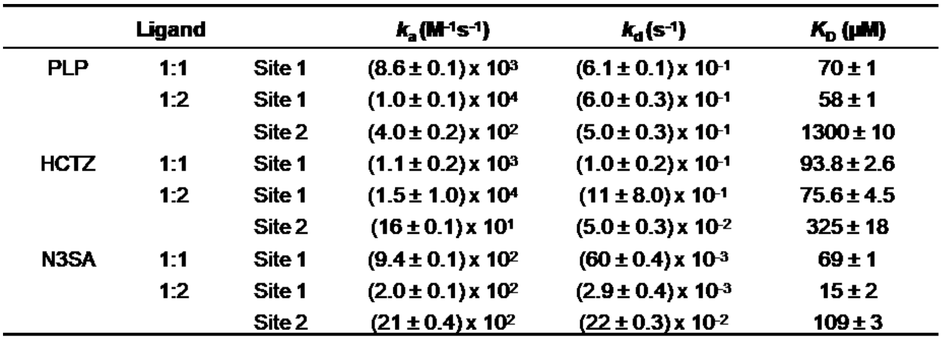

Ligand			k_a ($M^{-1}s^{-1}$)	k_d (s^{-1})	K_D (μM)
PLP	1:1	Site 1	$(8.6 \pm 0.1) \times 10^3$	$(6.1 \pm 0.1) \times 10^{-1}$	70 ± 1
	1:2	Site 1	$(1.0 \pm 0.1) \times 10^4$	$(6.0 \pm 0.3) \times 10^{-1}$	58 ± 1
		Site 2	$(4.0 \pm 0.2) \times 10^2$	$(5.0 \pm 0.3) \times 10^{-1}$	1300 ± 10
HCTZ	1:1	Site 1	$(1.1 \pm 0.2) \times 10^3$	$(1.0 \pm 0.2) \times 10^{-1}$	93.8 ± 2.6
	1:2	Site 1	$(1.5 \pm 1.0) \times 10^4$	$(11 \pm 8.0) \times 10^{-1}$	75.6 ± 4.5
		Site 2	$(16 \pm 0.1) \times 10^1$	$(5.0 \pm 0.3) \times 10^{-2}$	325 ± 18
N3SA	1:1	Site 1	$(9.4 \pm 0.1) \times 10^2$	$(60 \pm 0.4) \times 10^{-3}$	69 ± 1
	1:2	Site 1	$(2.0 \pm 0.1) \times 10^2$	$(2.9 \pm 0.4) \times 10^{-3}$	15 ± 2
		Site 2	$(21 \pm 0.4) \times 10^2$	$(22 \pm 0.3) \times 10^{-2}$	109 ± 3

k_a: Association rate constant; k_d: Dissociation rate constant; K_D: Equilibrium dissociation constant. Experimental error is reported in parentheses and was obtained from two independent analyses.

For PLP, the 2-site model provided a slightly better fit particularly in the association phase of the response, as observed from the fitting comparison and related residual plots reported in Figure 3.1. Residual plots show the residual difference between the experimental curves and the simulated curves at each time point. For HCTZ and N3SA, the 2-site model better fitted the experimental data, showing an improved fit curve in both the association and dissociation phases. Using this fitting model, PLP displayed a K_D of 58 ± 1 μM toward NAPE-PLD, HCTZ a K_D of 75.6 ± 4.5 μM, and N3SA a K_D of 15 ± 2 μM (table 3.2). Fitting results suggest the presence of another binding site of lower affinity for all the three ligands, which can appear at higher analyte concentrations.

In response to issues associated with non-specific binding related to the high analyte concentrations, we carried out additional experiments for the three ligands by reducing the maximum analyte concentration tested. To validate the outcomes derived from the OneStep® injection experiments, we employed the multi-cycle kinetic method (MCK). In a multi-cycle approach, experiments are performed in replicates, with different concentrations (minimum 3-5) of each analyte under evaluation. Each injection of an analyte was done in a separate sequence, and a single SPR curve was generated per analyte concentration.

In this work, each dilution series was injected in triplicate under similar buffer conditions as the OneStep® assay. The resulting data were exclusively analyzed using a 1:1 interaction model to determine the binding constants. Representative sensorgrams illustrating the interactions are presented in Figure 3.2 and kinetics parameters are displayed in table 3.3. The affinity (K_D) of PLP for NAPE-PLD was determined to be 35.0 ± 3.6 μM, HCTZ exhibited a K_D of 43.6 ± 11.2 μM, and N3SA of 24.2 ± 0.1 μM. The resulting ligand efficiency (LE = $-\Delta G/N$ heavy atoms, where $\Delta G = -RT \log K_D$) values of 0.38 kcal/mol, 0.35 kcal/mol and 0.29 kcal/mol, respectively, highlighted the high quality of these hit compounds.

Ligand efficiency is a concept in drug discovery and medicinal chemistry that assesses the efficiency of ligand in binding to its target protein and it is estimated by equation (Hopkins et al, 2014):

$$\mathrm{LE} = \left(-2.303 \times \left(\frac{\mathrm{RT}}{\mathrm{HA}}\right)\right) \times \log K_D \tag{3.3}$$

where:

R = ideal gas constant (1.987×10^{-3} kcal $K^{-1}mol^{-1}$)
T = analysis temperature in Kelvin (K)
HA = number of non-hydrogen (heavy) atoms in the molecule
K_D = equilibrium dissociation constant (M)

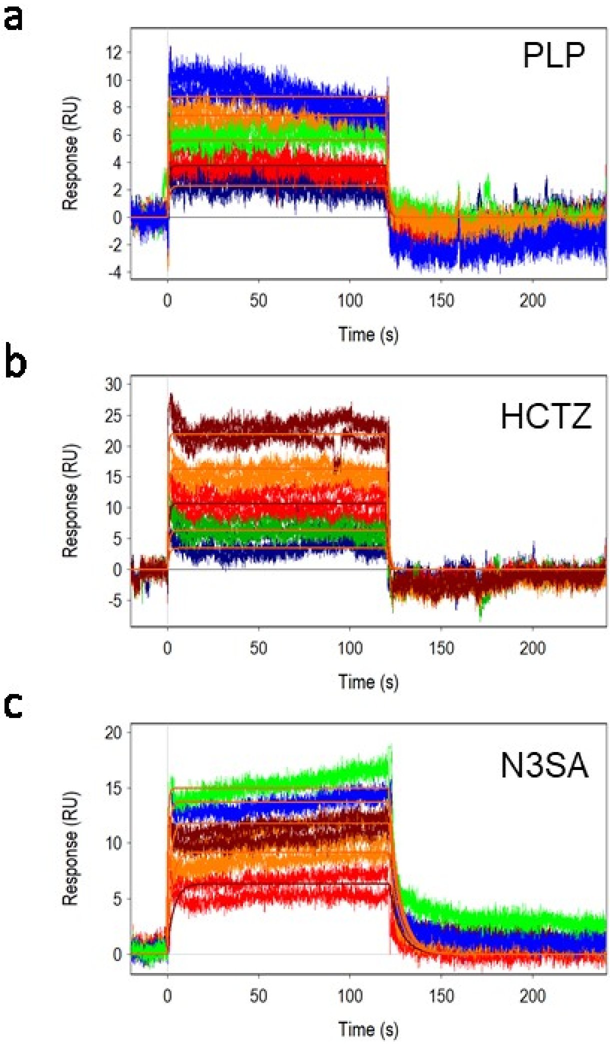

Figure 3.2. SPR analysis of novel ligands interacting with NAPE-PLD using the standard SPR injection method (multi-cycle kinetics experiments, MCK). a) Representative sensorgrams obtained from triplicate injections of PLP in a twofold dilution series starting at 125 µM. b) Representative sensorgrams obtained from triplicate injections of HCTZ in a twofold dilution series starting at 62,5 µM. c) Representative sensorgrams obtained from triplicate injections of N3SA in a twofold dilution series starting at 250 µM. Orange lines depict the global fit of the data to a simple 1:1 interaction model. The kinetic parameters obtained from each interaction are reported in Table 3.3.

Table 3.3. Affinity and rate constants for NAPE-PLD/ligand interactions

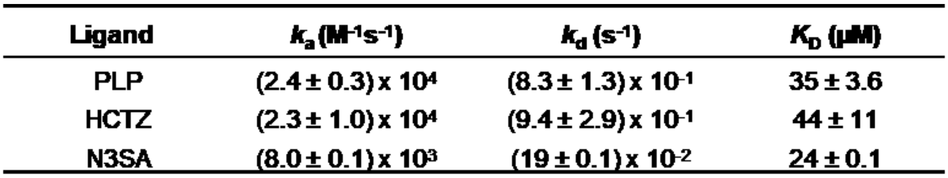

Ligand	k_a ($M^{-1}s^{-1}$)	k_d (s^{-1})	K_D (μM)
PLP	$(2.4 \pm 0.3) \times 10^4$	$(8.3 \pm 1.3) \times 10^{-1}$	35 ± 3.6
HCTZ	$(2.3 \pm 1.0) \times 10^4$	$(9.4 \pm 2.9) \times 10^{-1}$	44 ± 11
N3SA	$(8.0 \pm 0.1) \times 10^3$	$(19 \pm 0.1) \times 10^{-2}$	24 ± 0.1

k_a: Association rate constant; k_d: Dissociation rate constant; K_D: Equilibrium dissociation constant. Experimental error is reported in parentheses and was obtained from two or more independent analyses using different biosensors, sample preparations, and ligand densities on the flow cell surfaces.

The comparison of affinities between the OneStep® injection method and the multi-cycle kinetic method (MCK) offers valuable insights into the consistency and reliability of the experimental results. The OneStep® injection method is known for its efficiency in quickly capturing the binding kinetics in a single injection cycle, because of a sigmoidal concentration gradient of the analyte, whereas the MCK method allows for a more in-depth analysis through multiple injection cycles at different fixed concentrations and can offer a more thorough and reliable representation of the binding kinetics. Furthermore, it is not affected by the concentration gradient during the assay.

For PLP, the OneStep® method yielded an affinity, K_D, of about 70 μM, while the MCK method resulted in an affinity of 35 ± 3.6 μM. Similarly, the OneStep® method applied to HCTZ indicated an affinity of about 75 μM, whereas the MCK method showed an affinity of 44 ± 11 μM. Again, the MCK can capture a more accurate view of the interaction dynamics, contributing to the observed difference in affinity values. For N3SA, the OneStep® method yielded an affinity of about 15 μM, while the MCK method resulted in an affinity of 24 ± 0.1 μM. Despite differences in the K_D numerical values, both the experimental approaches provide a similar affinity trend among the distinct interacting compounds.

In summary, while the OneStep® injection method provided a quick overview of the binding kinetics, the multi-cycle kinetic method enhanced the depth of analysis. The application of both methods contributed to a more robust and reliable characterization of ligand-protein interactions. Overall, the congruence of outcomes from both methods confirmed the low micromolar affinities of PLP, HCTZ and N3SA for NAPE-PLD.

3.1.2 Modulation of protein-ligand binding by bile acids

In previous studies by our research group, the role of bile acids in regulating NAPE-PLD activity was discovered and explored (Magotti et al., 2015; Margheritis et al., 2016). We revealed that bile acids, such as sodium deoxycholate, modulate the protein flexibility, thereby allosterically influencing its activity. Thus, we wondered whether bile acids might also affect the interaction of selected ligands. Representative sensorgrams of the interaction between PLP and the target, or HCTZ and the target, in the presence of the bile acid DCA at 500 μM are reported in Figure 3.3. PLP displayed a K_D of 13.4 ± 5.2 μM and HCTZ a K_D of 8.8 ± 2.2 μM (table 3.4) and a ligand efficiency of 0.42 kcal/mol) and 0.41 (kcal/mol), respectively.

These preliminary results indicated that, in comparison with the analysis without the bile acid, the ligands affinity was indeed affected by bile acids. Specifically, the affinity for PLP increased approximately three-fold, and for HCTZ, it showed a five-fold improvement in the presence of DCA. This investigation highlights the notable impact of bile acids on ligand-protein interactions and provide valuable insights into their role in the membrane target modulation mechanisms.

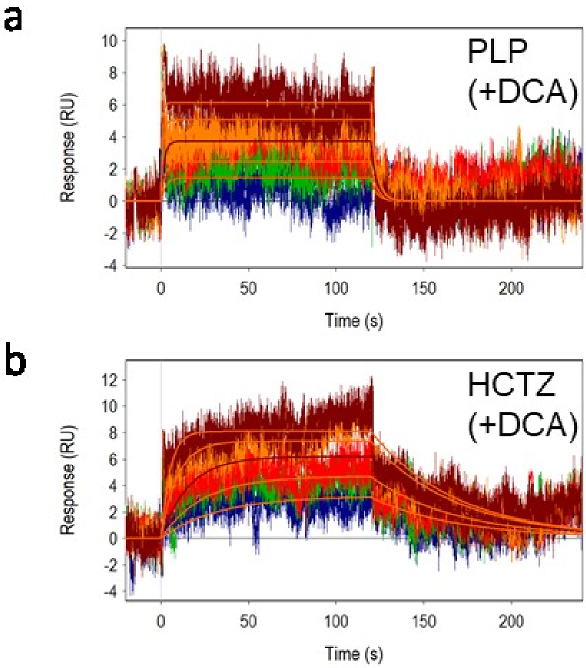

Figure 3.3. SPR analysis of PLP and HCTZ interacting with NAPE-PLD in presence of DCA using the standard SPR injection method (multi-cycle kinetics experiments, MCK). a) Representative sensorgrams obtained from triplicate injections of PLP in a two-fold dilution series starting at 62.5 μM in presence of 500 μM DCA. b) Representative sensorgrams obtained from triplicate injections of HCTZ in a two-fold dilution series starting at 62.5 μM. Orange lines depict the global fit of the data to a simple 1:1 interaction model. The kinetic parameters obtained from each interaction are reported in Table 3.4.

Table 3.4. Affinity and rate constants for NAPE-PLD/ligand interactions in presence of DCA

Ligand	k_a ($M^{-1}s^{-1}$)	k_d (s^{-1})	K_D (μM)
PLP	(2.7 ± 1.4) X 10^4	(3.3 ± 0.5) X 10^{-1}	13 ± 5.2
HCTZ	(2.8 ± 0.1) X 10^3	(2.4 ± 0.6) X 10^{-2}	8.8 ± 2.2

k_a: Association rate constant; k_d: Dissociation rate constant; K_D: Equilibrium dissociation constant. Experimental error is reported in parentheses and was obtained from two independent analyses.

Overall, these SPR studies confirmed that the three small molecules PLP, HCTZ and N3SA bind to NAPE-PLD with affinities in the low micromolar range. To validate the binding results obtained by SPR, we used X-ray crystallography as orthogonal method to investigate the interactions of the selected compounds with NAPE-PLD.

3.2 Structural investigation of NAPE-PLD interactions

To explore the interactions between NAPE-PLD and the selected compounds PLP, HCTZ and N3SA we successfully applied X-ray crystallography, which provided a deep understanding on how the target binds these ligands within a common structural site. All the crystal structures of NAPE-PLD/ligands complexes were obtained utilizing the co-crystallization technique. In co-crystallization, the protein and ligand are combined in a solution before initiating crystallization experiments. Co-crystallization offers several advantages in the study of protein–ligand complexes. One key benefit lies in its ability to capture more reliable binding poses, particularly for flexible proteins such as kinases and larger ligands (Wienen-Schmidt et al., 2021). The method provides a more comprehensive understanding of induced protein adaptations, enhancing the accuracy of structural information. Compared to alternative methods like soaking, co-crystallization can yield results with smaller geometrical discrepancies, especially when dealing with fragment-sized ligands. Its superiority in preserving the correct spatial arrangement of protein amino-acid side and main chain atoms makes co-crystallization the preferred approach (Wienen-Schmidt et al., 2021). All the structures were solved using the molecular replacement method. This method relies on the use of a known structure, often a homologous protein or a previously determined substructure, as a starting model. The unknown structure is solved by searching for the orientation and position of the known model within the unit cell of the crystal. The process involves mathematical algorithms that iteratively adjust the model until its predicted diffraction pattern closely matches the experimental data (Rupp, 2009).

3.2.1 Crystal structure of NAPE-PLD in complex with PLP

PLP plays a crucial role as a coenzyme in various biochemical reactions in the body. As the active form of vitamin B6, PLP participates in numerous enzymatic reactions involved in metabolism, neurotransmitter synthesis, and other essential processes. It has been reported to play a role in context with cardiovascular disease and blood pressure, diabetes, neurological activity and to exert potent antioxidant effect (Hellmann and Mooney, 2010; Parra et al., 2018).

The crystal structure of NAPE-PLD in complex with PLP (PDB ID: 8P90) at 2.80 Å of resolution confirmed the PLP interaction measured in vitro by SPR. The complex co-crystallized in lithium sulfate by adding the bile acid DCA (0.1%) to the purified protein. Diffraction data were collected at 100K at the XRD2 beamline of ELETTRA synchrotron of Trieste (Italy) (see Table 3.7 for data collection statistics). Data were processed using the MOSFLM software under the CCP4 suite interface. After integration, systematic absences were analyzed to identify the space group, using the Pointless software. Scaling in the correct space group was performed using the software Aimless of the CCP4 suite. The crystallographic data showed that the crystal belong to the $P6_522$ space group. The phase problem was solved by the molecular replacement method using the PHENIX software and the coordinates of the native protein structure having PDB ID accession number 4QN9 (Magotti et al., 2015). The final model (figure 3.4a) was refined using COOT and PHENIX software package to an R-factor of 0.271 (R-free= 0.295) (see Table 3.7 for data refinement statistics). Deviations (root mean square deviations) from ideal bond lengths and angles are 0.011Å and 1.45° respectively.

The overall complex structure showed, interestingly, the ligand bound to the dimer internal channel of the enzyme highlighting the subunits interface as interaction site of the protein for this natural compound (figure 3.4a).

The pyridine nitrogen of the complexed natural ligand interacted with Gln158 through a bridging water molecule. The reactive carbonyl acceptor was at hydrogen bond distance from the side chain of Ser152, together with the ring hydroxyl group. The phosphate group formed four hydrogen bonds, involving Ser151 side chain, Ile172 backbone nitrogen, and the side chains of Ser152 and Lys163 of the opposite subunit (Figure 3.4c). These specific interactions unveiled a specific interaction site for PLP at the interface of the NAPE-PLD homodimer.

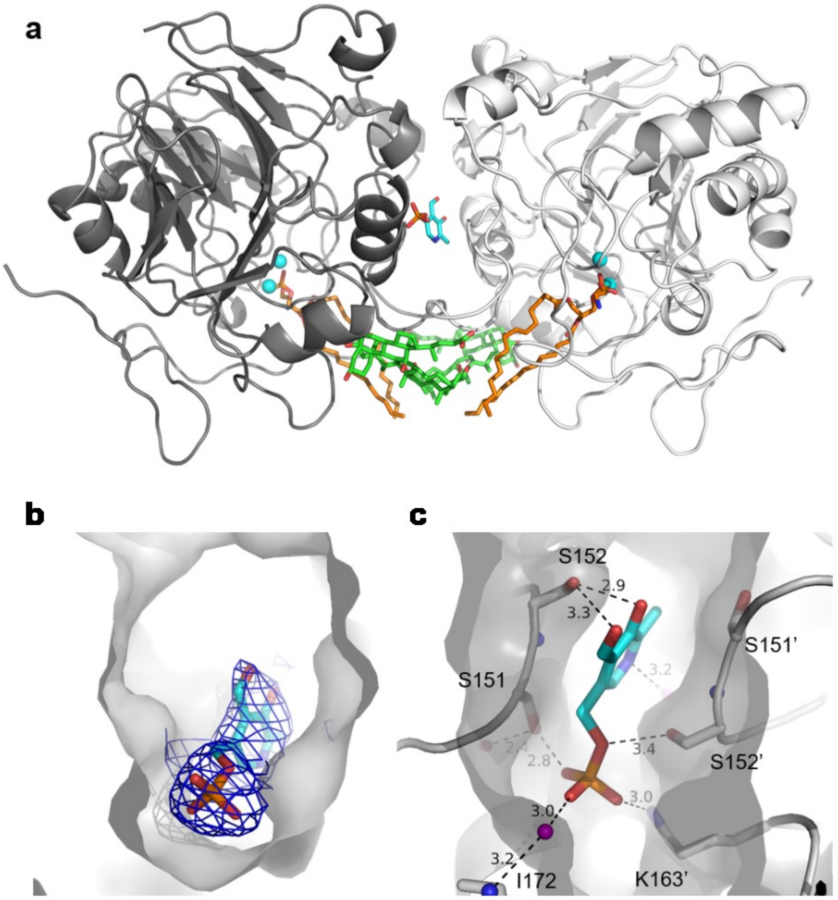

Figure 3.4. Structure of human NAPE-PLD in complex with PLP. a) View of the overall homodimeric architecture of the membrane phospholipase D, NAPE-PLD showing its ~9 Å-wide internal channel located at the interface of protein subunits (in light and dark gray) and along the non-crystallographic pseudo two-fold axis. Bound to the active site is a molecule of phosphatidylethanolamine (PE, carbons in orange), which indicates how the substrate NAPE goes in and binds the binuclear zinc-containing active site (zinc ions in cyan). The bound molecule of PLP (carbons in cyan) locates at the channel rim. Other elements are coloured as follows: oxygen, red; nitrogen, dark blue; phosphorus, orange. b) Expanded view of the internal channel of NAPE-PLD where the ligand binds. The $2Fo - Fc$ electron density map (shown in blue) is shown at the 1σ level. c) Close-up view of the binding site. Dashed lines with distances Å indicate hydrogen bonding. Purple spheres indicate water molecules involved in hydrogen bonding. The superscript comma indicates residues of the opposite dimer subunit. All the representations show the same orientation of the protein.

The PLP molecule positioned within the ~9 Å-wide dimer internal channel (figure 3.4a), along the non-crystallographic two-fold axis. Interesting, as observed in the apo-form, also the BA-binding sites were located between the two protein subunits (figure 3.5).

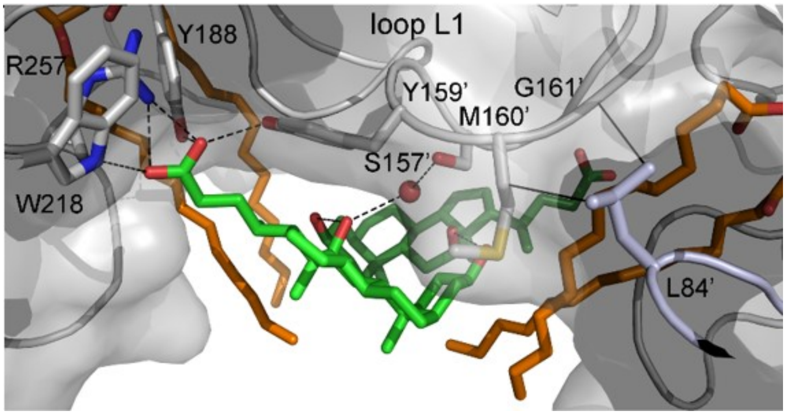

Figure 3.5. Expanded view of NAPE-PLD BA-binding site and selected side chain residues. The two central molecules of DCA (green carbons) form a micellar BA couple bound to the protein dimer interface. Each BA molecule established hydrogen bonds with the side chains of Tyr188, Trp218 and Arg257, with the steroid hydroxyl groups within the micellar BA couple, and with a water molecule that bridged Ser157 to the opposed protein subunit. Dashed and continuous lines indicate the hydrogen bond network and hydrophobic interactions, respectively. The superscript comma indicates residues of the opposite subunit. The BA-structured loop L1 is the sole secondary structural element connecting the two protein subunits. This image also shows the loop of L84 (light blue) covering the substrate upon binding.

When compared to the apo-form structure, the crystal structure of NAPE-PLD in complex with PLP provided a more detailed resolution of the loop spanning from Val80 to His90. This structural insight enabled the characterization of hydrophobic interactions involving Leu84 and loop L1, which proved crucial for recognizing substrate and bile acid (BA) molecules (figure 3.5). Consistent with the apo-form structure, residues in the first half of the sequence, along with unique structural elements rich in prolines, formed an extensive hydrophobic surface in the dimer for interacting with

BA molecules and membrane lipids (Magotti et al., 2015; Margheritis et al., 2016). This specific region of the protein encompassed the entire loop L1 (from Thr146 to Thr171), serving as the primary structural element for the symmetrical association of the two protein subunits (figure 3.5). The stabilization of the two L1 loops was facilitated by couples of BA molecules associated as dimeric micelles.

3.2.2 Synthesis of PLP analogues and SPR-screening

The active form of Vitamin B6, PLP, functions as a coenzyme in many enzymatic processes (Eliot and Kirsch, 2004). PLP-dependent enzymes are involved in many key cellular processes and metabolism and PLP is required for the synthesis of the neurotransmitters serotonin, dopamine, norepinephrine, epinephrine, and γ-aminobutyric acid (GABA). The wide variety of reactions catalysed by PLP enzymes is enabled by the ability of the covalent aldimine intermediate to stabilize carbanionic intermediates at Cα of the substrate (Toney, 2011).

The discovery of the interaction of PLP with NAPE-PLD using different structural biophysics approaches suggested ways of compound evolution to enhance affinity for the target, and a captivating physiological scenario where the process of lipid amide biogenesis in cells of different tissues (e.g. brain, heart, intestine, liver and immune system) might be linked directly by NAPE-PLD to the (i) biosynthesis neurotransmitters or their transport, and (ii) metabolism (i.e. of lipid), where vitamin B6 is well known to have a key role. To support this hypothesis, we designed and synthetized a series of aldimine analogues of PLP (table 3.5), in collaboration with Prof. Simona Rapposelli (Department of Pharmacy, University of Pisa). The X-ray crystal structure of PLP in complex with NAPE-PLD was used to guide the design of this small set of compounds (1-4) and probe the binding pocket formed by the internal channel at the interface between the two protein subunits.

Table 3.5. Chemical structures, molecular weights and molecular formulas of compounds 1-4.

Compound	Chemical Structure	Molecular Formula	Molecular Weight (g/mol)
1	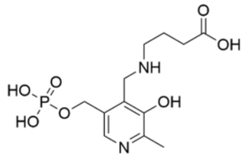	$C_{12}H_{19}N_2O_7P$	334,26
2	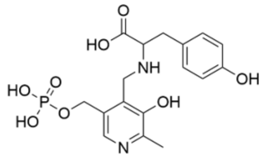	$C_{17}H_{21}N_2O_8P$	412,33
3	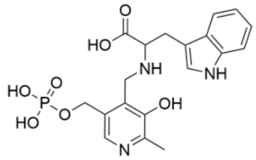	$C_{19}H_{22}N_3O_7P$	435,37
4	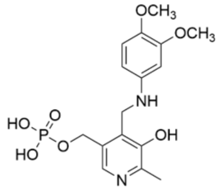	$C_{16}H_{21}N_20_7P$	384,32

PLP-catalyzed reaction types can be divided according to the position at which the net reaction occurs. Reactions at the α position include transamination, decarboxylation, racemization, and elimination and replacement of an electrophilic R group. Those at the β or γ position include elimination or replacement. Although the scope of PLP-catalyzed reactions initially appears to be diverse, there is a unifying principle. The cofactor in all cases functions to stabilize negative charge development at C_α in the transition state that is formed after condensation of the amino acid substrate with PLP to form a Schiff base. The fully formed carbanion is referred to as the quinonoid intermediate (Eliot and Kirsch, 2004) (figure 3.6).

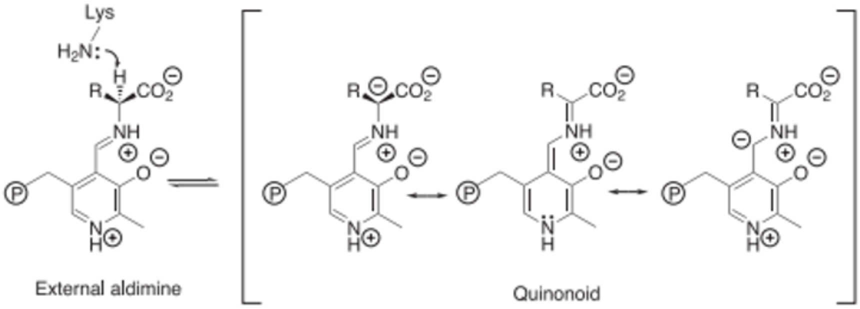

Figure 3.6. Stabilization of anions generated at Cα by PLP. The negative charge is delocalized by resonance in the aromatic system of the PLP in the quinonoid intermediate after loss of a proton from the external aldimine. Adapted from Eliot and Kirsch, 2004.

Compounds 1-4 were structurally non-hydrolysable analogues of the intermediate aldimine conjugated with γ aminobutyric acid, L-tyrosine, L-tryptophan and a catechol derivative. The transition-state analogues 1-4 were synthetized by reductive amination of the PLP moiety (Ikawa, 1967; Rudd et al., 1979; Iskander et al., 1991). Newly synthesized compounds were characterized using ^{1}H, ^{13}C NMR as well as MS analysis. The characterization data of target molecules were found to be compatible with their structure. Spectral data details are given in the experimental section.

The compounds were evaluated for their ability to bind NAPE-PLD by SPR. SPR analysis with these new ligands was performed to assess their affinity for the NAPE-PLD. Related sensorgrams of multi-cycle kinetics assay are reported in figure 3.7 and the binding kinetics are reported in table 3.6. One of the four ligands, cmpd4, displayed a binding affinity comparable to that of PLP (72.3 ± 0.5 μM). Cmpd2 exhibited a lower affinity (183 ± 1 μM), whereas the newly synthesized compounds, cmpd1 and cmpd3, showed an enhanced affinity for NAPE-PLD compared to PLP (11 ± 2 μM and 7.2 ± 0.1 μM, respectively), demonstrating that derivatives of PLP may be exploited as specific ligands.

These results suggested to explore the structural interaction between the synthesised compounds and the target protein. Anyhow, despite several attempts were made to crystallize compounds 1-4 in complex with the membrane-associated protein, we were unable to obtain good quality crystals for X-ray diffraction analysis.

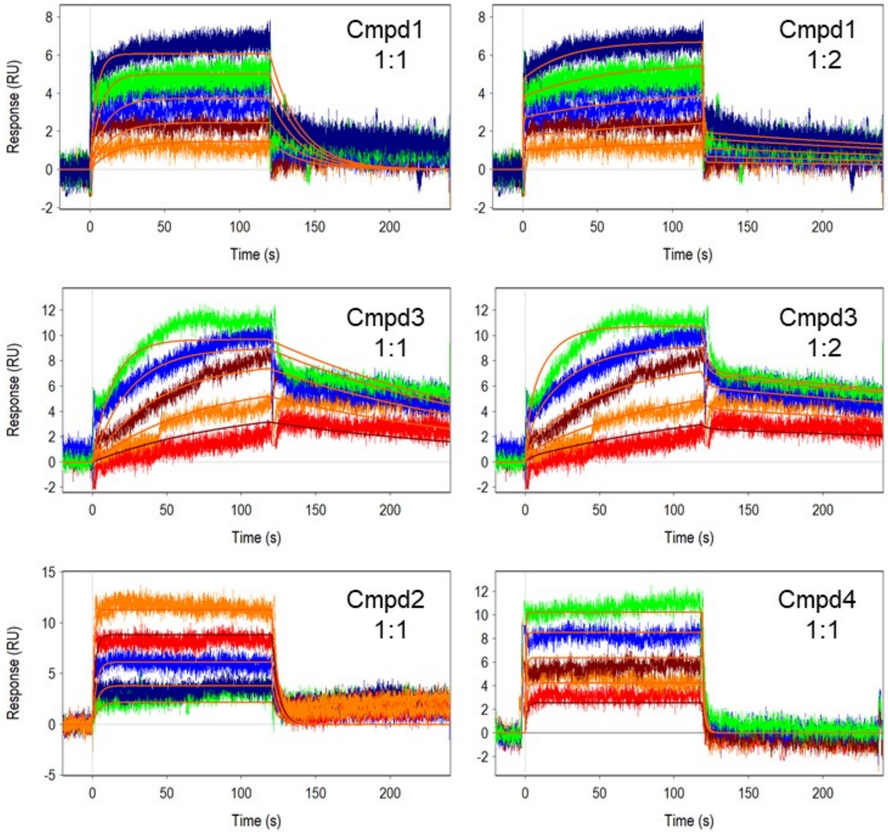

Figure 3.7. SPR analysis of PLP-analogues compounds interacting with NAPE-PLD determined at 25 °C using surface plasmon resonance by multi-cycle injection. Representative sensorgrams obtained from triplicate injections of compounds 1-4 in a two fold dilution series starting at 250 μM. Orange lines show a global fit to the response data used to extract the binding constants using a 1:1 model and a 1:2 model. The binding constants determined from the fits are listed in table 3.6.

Table 3.6. Affinity and rate constants for NAPE-PLD/PLP analogues interactions

Ligand			**k_a ($M^{-1}s^{-1}$)**	**k_d (s^{-1})**	**K_D (μM)**
Cmpd1	**1:1**	**Site 1**	**$(50 \pm 0.4) \times 10^1$**	**$(8.7 \pm 0.1) \times 10^{-2}$**	**176 ± 1**
	1:2	**Site 1**	**$(6.9 \pm 0.1) \times 10^1$**	**$(8 \pm 1) \times 10^{-4}$**	**11 ± 2**
		Site 2	**$(5.4 \pm 0.1) \times 10^3$**	**$(11 \pm 0.2) \times 10^{-1}$**	**199 ± 1**
Cmpd2	**1:1**	**Site 1**	**$(14 \pm 0.2) \times 10^2$**	**$(250 \pm 0.3) \times 10^{-3}$**	**183 ± 1**
Cmpd3	**1:1**	**Site 1**	**$(26 \pm 0.1) \times 10^1$**	**$(61 \pm 0.2) \times 10^{-4}$**	**29 ± 0.1**
	1:2	**Site 1**	**$(25 \pm 0.1) \times 10^1$**	**$(18 \pm 0.2) \times 10^{-4}$**	**7.2 ± 0.1**
		Site 2	**$(12 \pm 0.4) \times 10^2$**	**$(6.3 \pm 0.2) \times 10^{-1}$**	**510 ± 10**
Cmpd4	**1:1**	**Site 1**	**$(11 \pm 0.2) \times 10^3$**	**$(7.6 \pm 0.1) \times 10^{-1}$**	**72 ± 1**

k_a: Association rate constant; k_d: Dissociation rate constant; K_D: Equilibrium dissociation constant. Experimental error is reported in parentheses and was obtained from two independent analyses.

3.2.3 Crystal structure of NAPE-PLD in complex with HCTZ

Hydrochlorothiazide is a medication that belongs to a class of drugs called thiazide diuretics. It is primarily used alone or in combination with other drugs for the treatment of hypertension and edema (Messerli et al., 2011; Suchard et al., 2019).

Our herein reported SPR studies showed an effective interaction between the diuretic hydrochlorothiazide and our target protein NAPE-PLD. Given the pharmacological significance of HCTZ, we conducted crystallographic experiments to elucidate the structural basis of the interaction. This information could provide valuable insights for a possible use of the clinical compound to modulate NAPE-PLD.

We successfully determined the three-dimensional structure of NAPE-PLD in complex with the thiazide diuretic by X-ray crystallography (PDB ID: 8PC4) at 2.85 Å resolution. As for the PLP complex, the complex with HCTZ co-crystallized in lithium sulfate with the bile acid DCA (0.1%) to the purified protein. Diffraction data were collected at 100K at the XRD2 beamline of ELETTRA synchrotron of Trieste (Italy) (see Table 3.7 for data collection statistics). Data were processed using the MOSFLM software under the CCP4 suite interface. The crystal belongs to the same $P6_522$ space group observed for the complex with PLP and the phase problem of the structure was solved similarly. The final model (figure 3.8a) was refined using COOT and PHENIX software package to an R-factor of 0.267 (R-free= 0.301) (see Table 3.7 for data refinement statistics). Deviations (root mean square deviations) from ideal bond lengths and angles are 0.008Å and 1.26° respectively.

Interestingly, the complex structure exhibited a homodimeric architecture with the diuretic HCTZ bound to the interface of the two protomers, inside the ~9 Å-wide channel and along the non-crystallographic pseudo two-fold axis. Thus, the position of the bound HCTZ proved to be similar to that observed for PLP in its complex (figure 3.8a).

The electron density map showed the thiazide molecule located inside the space between the couples of residues Ser151-Ser152 of the two protein subunits. The specificity of the thiazide-binding site shined by different strong electrostatic interactions (figure 3.8c). The two oxygen of the sulphur dioxide of the drug formed two strong hydrogen bonds with the backbone nitrogen of the residue Ser152 of both subunits. On the other side, the sulfonamide group interacted strongly with the side chains of Ser151 of one subunit and Ser152 of the opposite one. The thiazide nitrogen at position 2 of the ring established another hydrogen bond with the side chain Ser152 of one of the two subunits. Finally, the chlorine at position 6 formed another strong interaction with the backbone nitrogen of Ile172 by a bridging water molecule.

Overall, the crystal structure of the HCTZ complex validated our SPR results and confirmed the interaction of the drug to NAPE-PLD.

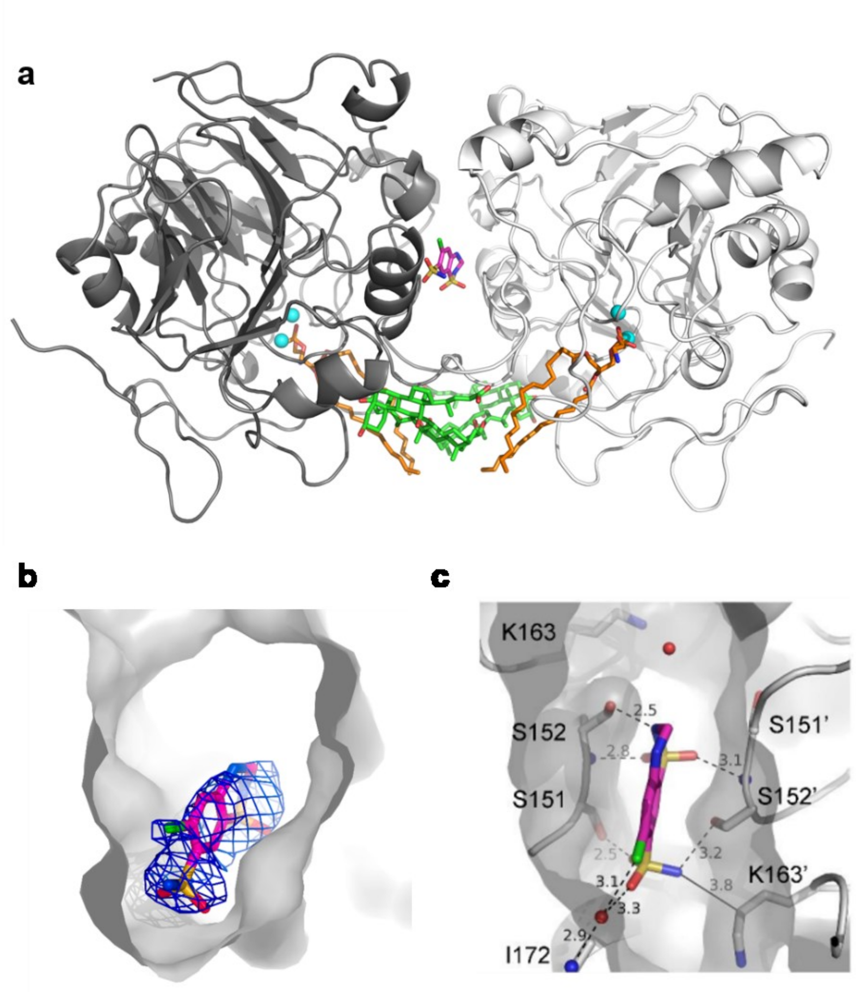

Figure 3.8. Structure of human NAPE-PLD in complex with the drug HCTZ. a) Overall structure of NAPE-PLD in complex with HCTZ (PDB ID: 8PC4). The homodimeric architecture of NAPE-PLD is indicated in light and dark gray. The bound molecule of HCTZ (carbons in magenta) locates ate the subunits interface inside the 9Å-wide channel. The bile acid molecules (green carbons) and PE molecules are reported (orange carbons). Other elements are coloured as follows: oxygen, red; nitrogen, dark blue; sulfur, yellow; chlorine, green. b) Electron density map of the ligand in the complex. The 2Fo − Fc map is shown at the 1σ level. c) Close-up view of the interaction site. Dashed and continuous lines with distances in Å indicate the hydrogen bond network and the hydrophobic interactions respectively. The presence of water molecules (red spheres) inside the channel illustrates a conduction pathway for solvent molecules. The superscript comma indicates residues of the opposite dimer subunit. All the representations show the same orientation of the protein.

3.2.4 Crystal structure of NAPE-PLD in complex with N3SA

As part of our validation efforts, aimed at evaluating the outcomes of binding studies utilizing SPR, we achieved another relevant result. We successfully managed to solve the crystal structure of NAPE-PLD in complex with the ligand 1,3,7-naphthalenetrisulfonic acid (N3SA). This compound bears a naphthalene moiety, extensively explored aromatic conjugated system used as substructure of different compounds with application in various pathophysiological conditions (e.g. cancer, infectious diseases, inflammation, hypertension, diabetes, neurodegenerative disorders) (Makar et al., 2019).

The complex co-crystallized in lithium sulfate in presence of the bile acid DCA (0.1%). The crystal structure was solved at a resolution of 2.86 Å (PDB ID: 8P96) by the method of molecular replacement using PDB 4QN9 as a search model. Diffraction data were collected at 100K at the XRD2 beamline of ELETTRA synchrotron of Trieste (Italy) (see Table 3.7 for data collection statistics). Data were processed using the MOSFLM software under the CCP4 suite interface. The crystal belongs to the same $P6_522$ space group observed for the complex with PLP and HCTZ and the phase problem of the structure was solved similarly. The final model (figure 3.9a) was refined using COOT and PHENIX software package to an R-factor of 0.257 (R-free= 0.284) (see Table 3.7 for data refinement statistics). Deviations (root mean square deviations) from ideal bond lengths and angles are 0.005Å and 1.02° respectively. The analysis of the crystal structure confirmed that also N3SA binds to the interface of NAPE-PLD subunits, tracing the interactions of PLP and HCTZ (figure 3.9a).

The interaction of N3SA was stabilized by strong hydrogen bonds with both subunits, which included Ser151, Ser152 and Ile172 of one, and Ser152, Lys163 and Arg167 of the other (figure 3.9c). Interesting, the co-crystal structure was obtained experimentally using a commercial isomeric mixture of (1,3,6) and (1,3,7) naphthalene-trisulfonic acid sodium salts (isomers ratio ≈ 80:20, respectively). The electron density map permitted a matching only for the 1,3,7- isomer, highlighting how the interacting residues at the interfacial subunit interface of NAPE-PLD are critical for compound recognition.

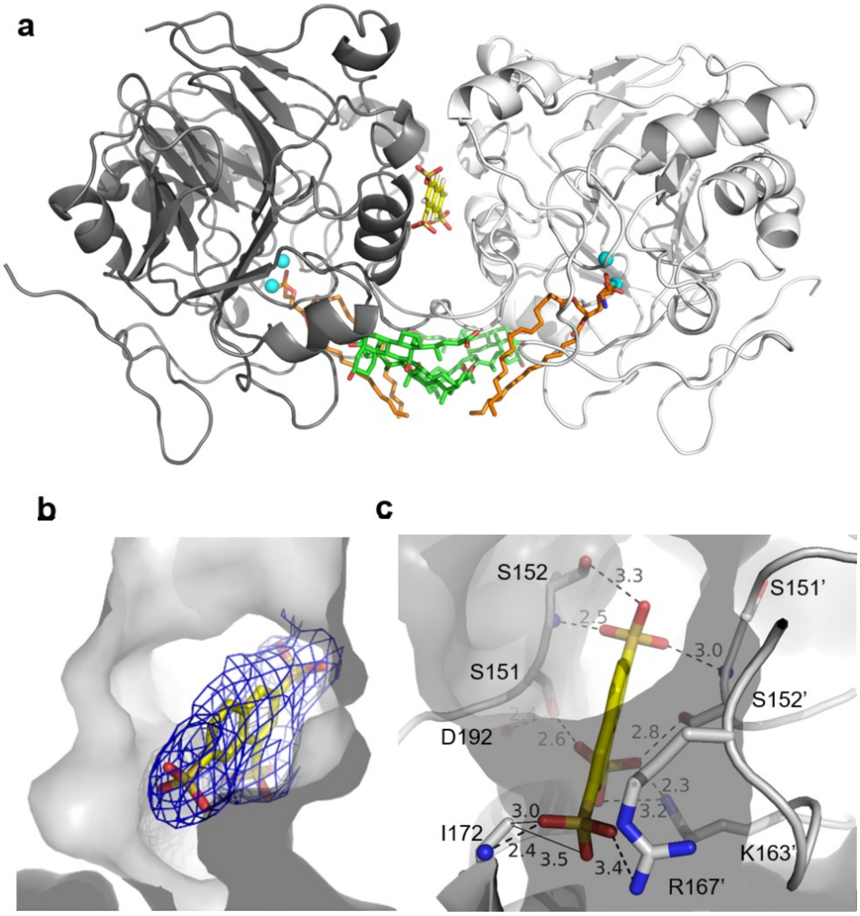

Figure 3.9. Structure of NAPE-PLD in complex with N3SA. a) Overall structure of the NAPE-PLD in complex with N3SA (PDB ID: 8P96). The dimer architecture of NAPE-PLD is indicated in light and dark gray. The bound molecule of N3SA (carbons in yellow) locates at the subunits interface inside the 9Å-wide channel. The bile acid molecules (green carbons) and PE molecules are reported (orange carbons). Other elements are coloured as follows: oxygen, red; nitrogen, dark blue; sulfur, yellow. b) Electron density map of the ligand in the complex. The 2Fo− Fc map is shown at the 1σ level. c) Close-up view of the interaction site. Dashed and continuous lines with distances in Å indicate the hydrogen bond network and the hydrophobic interactions respectively. The superscript comma indicates residues of the opposite dimer subunit. All the representations show the same orientation of the protein.

Table 3.7. Data collection and refinement statistics.

NAPE-PLD with	**HCTZ**	**N3SA**	**PLP**
PDB ID code	8PC4	8P96	8P90
Data Collection			
Synchrotron, Beamline	ELETTRA, XRD2	ELETTRA, XRD2	ELETTRA, XRD2
Wavelength (Å)	1.000	1.000	1.000
Space group	$P6_522$	$P6_522$	$P6_522$
Cell dimensions			
a, b, c (Å)	94.39, 94.39, 442.33	94.66, 94.66, 441.85	94.66, 94.66, 441.8
α, β, γ (deg)	90, 90, 120	90, 90, 120	90, 90, 120
Resolution (Å)	54.75 - 2.85 (2.95 - 2.85)	60.17 - 2.86 (2.96 - 2.86)	46.28 - 2.80 (2.90 - 2.80)
R_{merge}	0.036 (0.77)	0.060 (0.86)	0.0291 (1.15)
I / σI	11.5 (1.0)	5.06 (0.9)	13.4 (0.6)
Wilson B-factor	88.0	78.3	100.0
Completeness (%)	99.5 (98.5)	98.6 (95.6)	99.5 (96.9)
Muliplicity	2.0 (2.0)	2.0 (2.0)	2.0 (2.0)
No. Total reflections	57036 (5539)	56235 (5296)	60375 (5822)
No. Unique reflections	28536 (2771)	28144 (2660)	30188 (2911)
Refinement Statistics			
R_{work}	0.267 (0.468)	0.257 (0.432)	0.271 (0.401)
R_{free} [b]	0.301 (0.512)	0.284 (0.461)	0.295 (0.379)
No. atoms	5928	5946	5919
Protein	5501	5502	5501
Ligands	389	394	388
Solvent	38	50	30
B-factors (Å^2)	100.6	88.7	118.0
Protein	100.9	89.4	118.7
Ligands	96.8	84.3	109.0
Solvent	85.6	73.6	104.1
R.m.s. deviations			
Bond lengths (Å)	0.008	0.005	0.011
Bond angles (deg)	1.26	1.02	1.45
Ramachandran plot [c]			
favored (%)	85.7	86.0	83.0
allowed (%)	11.3	11.6	12.1
outliers (%)	3.0	2.4	5.0

The numbers in parentheses are for the highest resolution shell.

[a] Fig. of Merit (experimental phases) = <|ΣP(α)exp(iα)/ΣP(α)|> , where α is the phase and P(α) is the phase probability distribution.

[b] The R_{free} was calculated with a random 5% of the reflections.

[c] Values from Molprobity (http://molprobity.biochem.duke.edu).

Chapter 4

Discussion

Here we report the identification of different classes of novel ligands that bind NAPE-PLD in the low micromolar range. The ligands have been characterized by their affinity and binding kinetics, and by their mode of binding to the membrane target structurally, for the first time. They provide molecular basis for the evolution of compounds having potential to modulate the target.

During the initial screening via SPR, we observed that three ligands, PLP, HCTZ, and N3SA, interacted with NAPE-PLD. To characterize better their binding, in this work we conducted preliminary studies in presence of DCA, which showed to enhance their ligand affinity. The atomic coordinates reported herein revealed that the three ligands got in position similarly, at the interface of the two protein monomers and inside the ~9 Å-wide internal channel. The compounds and the interacting BA molecules bound to NAPE-PLD along the non-crystallographic pseudo two-fold axis, despite in distinct binding sites (Figure 3.4a). This finding may explain the ability of DCA to increase the affinity of the ligands, through strengthening the two subunits association.

The position of the bound ligands in the three structures suggested they may act as allosteric stabilizers the two protein subunits, as detected previously for bound BA molecules alone (Margheritis et al., 2016). This consideration was corroborated to the relative position of the binding sites of ligands and BAs, and by the structural analysis of the electron density map that, contrary to the apo-form coordinates (PDB ID: 4QN9) (Magotti et al., 2015), showed all secondary structural elements and loops of the protein well resolved, without any conformational variation in the protein backbone (figure 4.1).

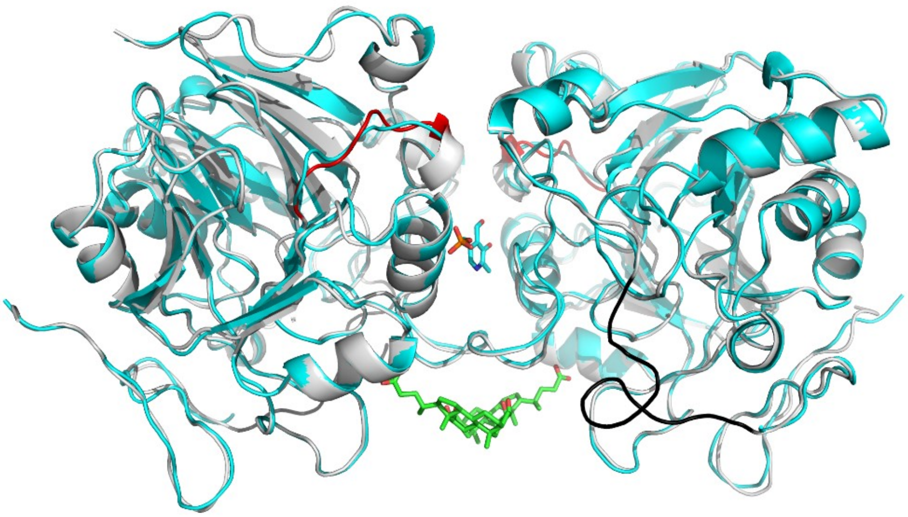

Figure 4.1. Stabilization of the NAPE-PLD structure in presence of PLP. Superposition of the apo-structure of NAPE-PLD (cyan) and the PLP-complex structure (grey) for structural comparison. The compared crystal structures have been obtained at similar resolution (2.6Å and 2.8Å, respectively). The loop coloured in black highlights residues resolved in the PLP-complex structure but missing in the apo-structure (Val80-His90). The loop coloured in red highlights residues observed in double conformation in the apo-structure but not in the PLP-complex structure (Glu174-Ala180).

The three crystal structures showed that the dimer internal channel of membrane NAPE-PLD was indeed a key interaction site for the subunit association and protein stabilization. Similarly, the two L1 loops of the homodimer contributed to promote the stabilization of the homodimer by means of couples of bound BA molecules (figure 4.1). The BA-binding site, as the ligands-binding site, located along the dimeric pseudo two-fold axis.

After these results we wondered a possible biological significance of the interaction between PLP with NAPE-PLD. To investigate this aspect, we examined in depth the interaction using selected synthetic non-hydrolysable PLP analogues, able to mimic a quinonoid intermediate and known to be a key intermediate in many PLP-dependent catalytic mechanisms. Among these, the serotonin-precursor tryptophan, the catecholamine-precursor tyrosine, and the inhibitory neurotransmitter GABA were conjugated to PLP. The measured affinities of these designed compounds by SPR suggested that the synthesised compounds might mirror the position occupied in the complex by PLP. Attempts to obtain their complexes with NAPE-PLD and characterized them by X-ray diffraction were unsuccessful.

Interestingly, literature widely reports the antihypertensive effect of PLP at high doses, as well as that of the thiazide drug HCTZ. Our results showed that both these molecules bound to NAPE-PLD in a common interaction site. We thus hypothesized that their interaction might be correlated with their profile in clinics.

The acute diuretic effect of thiazide drugs is believed to proceed mainly via inhibition of the sodium-chloride cotransporter (NCC) located in the luminal membrane of distal tubule cells (Beaumont et al., 1988; Fan et al., 2023). A low NCC function causes Gitelman syndrome, characterized by hypotension and electrolyte disorders (Fan et al., 2023). Anyhow, evidence regarding the importance of the kidney and NCC in the hypotensive effects of thiazides is contradictory, which provides evidence for the existence of an extrarenal target for these drugs (De Souza Goncalves et al., 2023). Apart from inhibiting the NCC and inducing diuresis, other mechanisms have also been suggested. These may encompass the reduction of peripheral resistance through both direct and indirect effects (Rapoport and Soleimani, 2019).

The discovery that NAPE-PLD showed affinity and displayed structurally specific interactions with the most used thiazide diuretic, HCTZ, suggested that NAPE-PLD might be a previously unknown systemic target of these essential class of drugs. To investigate this hypothesis, following investigations of the group focused on how the target associates with a lipid bilayer model of nanodiscs, using sp cryoEM experiments. Results of this initial study unveiled that NAPE-PLD could form pores in lipid bilayers, illustrating how NAPE-PLD might promote water permeation through membranes.

In addition, the compound N3SA discovered and characterized in this work for its binding to NAPE-PLD was tested in a young animal model of spontaneous hypertensive rats. Preliminary results indicated the efficacy of the compound N3SA bound to the thiazide binding site of NAPE-PLD in promoting antihypertensive action in vivo (figure 4.2). The hypotensive effect of the compound N3SA was never reported before our work.

Overall, the study reported herein and the above findings contribute to support the hypothesis that stabilizing NAPE-PLD at the dimer subunits interface might promote efficaciously reduction of blood pressure in animal model of hypertension. In line with this, also the supplementation of PLP and BAs at high doses has anti-hypertensive action in vivo, and we have characterized how these molecules can bind and stabilize NAPE-PLD at the subunits interface.

Importantly, the production of anandamide and other bioactive lipid mediators by NAPE-PLD is in line with the possible involvement of NAPE-PLD in the thiazide diuretics pharmacology. For instance, anandamide is well known to have direct vascular relaxing effects on vasculature, as well as indirect cardiovascular and metabolic actions through specific GCPR-mediated activation (Deutscg et al., 1997; Lake et al., 1997). Another lipid messenger from NAPE, oleoylethanolamine, modulates lipid metabolism, while palmitoylethanolamine serves as an early stop signal, beneficially counteracting inflammation and pain progression (Fu et al., 2003; Schwartz et al., 2008; Solorzano et al., 2009). These effects are consistent with some of the clinical profiles of thiazide diuretics, which include reduction of blood pressure by vascular resistance, and metabolic abnormalities (e.g., hyperlipidemia, hyperglycemia) (Cristino et al., 2019; Wardlaw et al., 2019; Piomelli and Tagne 2022).

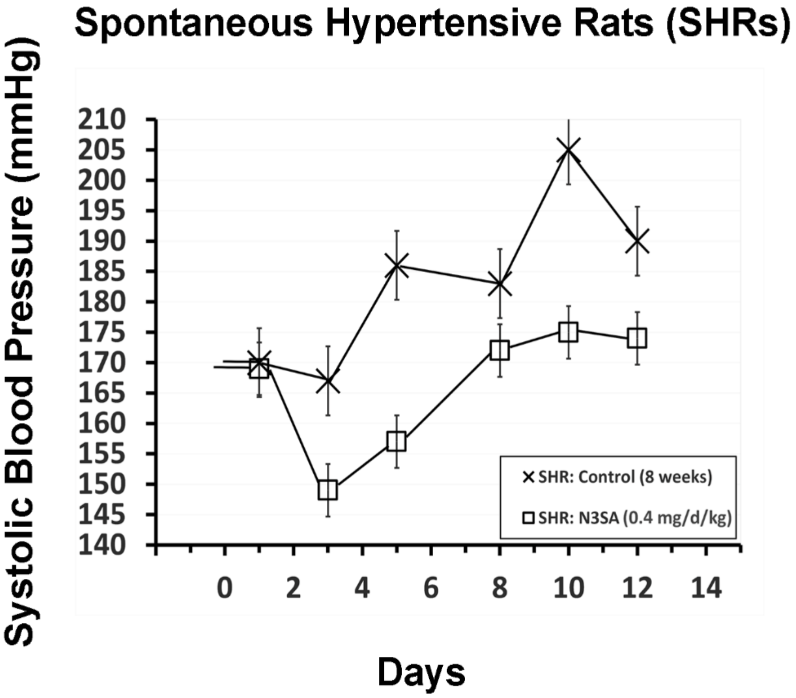

In conclusion of this work, the structural and biophysical results reported herein provide foundation for developing novel anti-hypertension agents that bind NAPE-PLD.

Figure 4.2. Preliminary time-course test of the effect of N3SA in SHRs of 8 weeks. After six days of treatment, the compound administration was interrupted to follow the blood pressure recovery.

Chapter 5

Conclusions and future perspectives

The study has uncovered novel ligands that bind to NAPE-PLD in the low micromolar range, with a dual focus on screening pharmaceutical relevant ligands and determining their structures when complexed with the target protein. Notable ligands identified in this context include PLP, HCTZ, and N3SA. Through structural investigations, insights into the position and interactions of these ligands have surfaced, hinting at a potential connection between NAPE-PLD, bile acids and the identified ligands. Additional structural and functional studies, together with ligand identification, hold the promise of providing a more comprehensive understanding of the target at molecular level. In this, the intricate molecular mechanism governing NAPE-PLD interactions merits further exploration to investigate their potential significance on the functional role of NAPE-PLD and its signalling pathways. Finally, the present study envisions possible clinical implications arising from the modulation of NAPE-PLD, especially in the realms of hypertension. Future translational studies will provide valuable insights into the effectiveness and safety of this therapeutic hypothesis.

Bibliography

Acharya, K. R. & Lloyd, M. D. The advantages and limitations of protein crystal structures. *Trends Pharmacol. Sci.* **26**, 10–14 (2005).

Adams, P. D. *et al.* PHENIX: A comprehensive Python-based system for macromolecular structure solution. *Acta Crystallogr. Sect. D Biol. Crystallogr.* **66**, 213–221 (2010).

Aggarwal, G. *et al.* Symmetrically substituted dichlorophenes inhibit N-acyl-phosphatidylethanolamine phospholipase D. *J. Biol. Chem.* **295**, 7289–7300 (2020).

Agirre, J. *et al.* The CCP4 suite: integrative software for macromolecular crystallography. *Acta Crystallogr. Sect. D, Struct. Biol.* **79**, 449–461 (2023).

Ahmad, T. R. & Haeusler, R. A. Bile acids in glucose metabolism and insulin signalling — mechanisms and research needs. *Nat. Rev. Endocrinol.* **15 (12)**, 701–712 (2019).

Anderson, A. C. The Process of Structure-Based Drug Design. *Chem. Biol.* **10**, 787–797 (2003).

Bátkai, S. *et al.* Endocannabinoids acting at cannabinoid-1 receptors regulate cardiovascular function in hypertension. *Circulation* **110**, 1996–2002 (2004).

Beaumont, K., Vaughn, D. A. & Fanestil, D. D. Thiazide diuretic drug receptors in rat kidney: Identification with [3H]metolazone. *Proc. Natl. Acad. Sci. U. S. A.* **85**, 2311–2314 (1988).

Beggiato, S., Cassano, T., Ferraro, L. & Tomasini, M. C. Astrocytic palmitoylethanolamide pre-exposure exerts neuroprotective effects in astrocyte-neuron co-cultures from a triple transgenic mouse model of Alzheimer's disease. *Life Sci.* **257**, 118037 (2020).

Beggiato, S., Tomasini, M. C. & Ferraro, L. Palmitoylethanolamide (PEA) as a potential therapeutic agent in Alzheimer's disease. *Front. Pharmacol.* **10**, 1–12 (2019).

Berger, C. *et al.* Massive accumulation of N-acylethanolamines after stroke. Cell signalling in acute cerebral ischemia? *J. Neurochem.* **88**, 1159–1167 (2004).

Bergfors, T. Seeds to crystals. *J. Struct. Biol.* **142**, 66–76 (2003).

Berman, H. M. *et al.* Biological Crystallography The Protein Data Bank. *Acta Cryst* **58**, 899–907 (2002).

Bertrand, T. *et al.* Structural Basis for Human Monoglyceride Lipase Inhibition. *J. Mol. Biol.* **396**, 663–673 (2010).

Bouchet, C. A. & Ingram, S. L. Cannabinoids in the descending pain modulatory circuit: Role in inflammation. *Pharmacol. Ther.* **209**, 1–29 (2020).

Bracey, M. H., Hanson, M. A., Masuda, K. R., Stevens, R. C. & Cravatt, B. F. Structural adaptations in a membrane enzyme that terminates endocannabinoid signaling. *Science* **298**, 1793–1796 (2002).

Calignano, A., La Rana, G., Giuffrida, A. & Piomelli, D. Control of pain initiation by endogenous cannabinoids. *Nature* **394**, 277–281 (1998).

Capelli, D., Scognamiglio, V. & Montanari, R. Surface plasmon resonance technology: Recent advances, applications and experimental cases. *TrAC - Trends Anal. Chem.* **163**, 117079 (2023).

Castellani, B. *et al.* Synthesis and characterization of the first inhibitor of: N - acylphosphatidylethanolamine phospholipase D (NAPE-PLD). *Chem. Commun.* **53**, 12814–12817 (2017).

Chayen, N. E. & Saridakis, E. Protein crystallization: From purified protein to diffraction-quality crystal. *Nat. Methods* **5**, 147–153 (2008).

Chiurchiù, V. & Maccarrone, M. Bioactive lipids as modulators of immunity, inflammation and emotions. *Curr. Opin. Pharmacol.* **29**, 54–62 (2016).

Chiurchiù, V., van der Stelt, M., Centonze, D. & Maccarrone, M. The endocannabinoid system and its therapeutic exploitation in multiple sclerosis: Clues for other neuroinflammatory diseases. *Prog. Neurobiol.* **160**, 82–100 (2018).

Choy, B. C., Cater, R. J., Mancia, F. & Pryor, E. E. A 10-year meta-analysis of membrane protein structural biology: Detergents, membrane mimetics, and structure determination techniques. *Biochim. Biophys. Acta - Biomembr.* **1863**, 183533 (2021).

Clapper, J. R. *et al.* Anandamide suppresses pain initiation through a peripheral endocannabinoid mechanism. *Nat. Neurosci.* **13**, 1265–1270 (2010).

Clegg, W. X-ray crystallography, third edition (Oxford University Press, 2015).

Correa, F., Wolfson, M. L., Valchi, P., Aisemberg, J. & Franchi, A. M. Endocannabinoid system and pregnancy. *Reproduction* **152**, R191–R200 (2016).

Cota, D. The endogenous cannabinoid system affects energy balance via central orexigenic drive and peripheral lipogenesis. *J. Clin. Invest.* **112**, 423–431 (2003).

Cravatt, B. F. *et al.* Supersensitivity to anandamide and enhanced endogenous cannabinoid signaling in mice lacking fatty acid amide hydrolase. *Proc. Natl. Acad. Sci. U. S. A.* **98**, 9371–9376 (2001).

Cravatt, B. F. *et al.* Molecular characterization of an enzyme that degrades neuromodulatory fatty-acid amides. *Nature* **384**, 83–87 (1996).

Cristino, L., Bisogno, T. & Di Marzo, V. Cannabinoids and the expanded endocannabinoid system in neurological disorders. *Nat. Rev. Neurol.* **16**, 9–29 (2020).

Dalle Carbonare, M. *et al.* A saturated N-acylethanolamine other than N-palmitoyl ethanolamine with anti-inflammatory properties: A neglected story... *J. Neuroendocrinol.* **20**, 26–34 (2008).

D'Arcy, A., Villard, F. & Marsh, M. An automated microseed matrix-screening method for protein crystallization. *Acta Crystallogr. Sect. D Biol. Crystallogr.* **63**, 550–554 (2007).

de Souza Goncalves, L., Yottasan, P. & Cil, O. Structure of human NCC: insights into the inhibition mechanism of thiazides. *Signal Transduct. Target. Ther.* **8**, 1–2 (2023).

Devane, W. a *et al.* Isolation and Structure of a Brain Constituent That Binds to the Cannabinoid Receptor. *Science* **258**, 1946–1949 (1992).

di Guana, C., Lib, P., Riggsa, P. D. & Inouyeb, H. Vectors that facilitate the expression and purification of foreign peptides in Escherichia coli by fusion to maltose-binding protein. *Gene* **67**, 21–30 (1988).

Di Marzo, V. Targeting the endocannabinoid system: To enhance or reduce? *Nat. Rev. Drug Discov.* **7**, 438–455 (2008).

Di Marzo, V. & Matias, I. Endocannabinoid control of food intake and energy balance. *Nat. Neurosci.* **8**, 585–589 (2005).

Di Marzo, V., Stella, N. & Zimmer, A. Endocannabinoid signalling and the deteriorating brain. *Nat. Rev. Neurosci.* **16**, 30–42 (2015).

Diep, T. A. *et al.* Dietary fat decreases intestinal levels of the anorectic lipids through a fat sensor. *FASEB J.* **25**, 765–774 (2011).

Donovan, R. S., Robinson, C. W. & Click, B. R. Review: Optimizing inducer and culture conditions for expression of foreign proteins under the control of the lac promoter. *J. Ind. Microbiol.* **16**, 145–154 (1996).

Egertovà, M., Simon, G. M., Cravatt, B. F. & Elphick, M. R. Localization of N-Acyl Phosphatidylethanolamine Phospholipase D (NAPE-PLD) Expression in Mouse Brain: A New Perspective on N- Acylethanolamines as Neural Signaling Molecules. *J. Comp. Neurol.* **506**, 604–615 (2008).

Eliot, A. C. & Kirsch, J. F. Pyridoxal phosphate enzymes: Mechanistic, structural, and evolutionary considerations. *Annu. Rev. Biochem.* **73**, 383–415 (2004).

Emsley, P., Lohkamp, B., Scott, W. G. & Cowtan, K. Features and development of Coot. *Acta Crystallogr. Sect. D Biol. Crystallogr.* **66**, 486–501 (2010).

Esposito, E., Cordaro, M. & Cuzzocrea, S. Roles of fatty acid ethanolamides (FAE) in traumatic and ischemic brain injury. *Pharmacol. Res.* 1–6 (2014).

Everard, A. *et al.* Intestinal epithelial N-acylphosphatidylethanolamine phospholipase D links dietary fat to metabolic adaptations in obesity and steatosis. *Nat. Commun.* **10**, 1–17 (2019).

Fahy, E., Cotter, D., Sud, M. & Subramaniam, S. Lipidomics NIH Public Access. *Biochim Biophys Acta.* **1811**, 637–647 (2012).

Fan, M., Zhang, J., Lee, C. L., Zhang, J. & Feng, L. Structure and thiazide inhibition mechanism of the human Na–Cl cotransporter. *Nature* **614**, 788–793 (2023).

Frank, J. Advances in the field of single-particle cryo-electron microscopy over the last decade. *Nat. Protoc.* **12**, 209–212 (2017).

Fu, J. *et al.* Food intake regulates oleoylethanolamide formation and degradation in the proximal small intestine. *J. Biol. Chem.* **282**, 1518–1528 (2007).

Fu, J. *et al.* Oleylethanolamide regulates feeding and body weight through activation of the nuclear receptor PPAR-α. *Nature* **425**, 90–93 (2003).

Gabrielsson, L., Mattsson, S. & Fowler, C. J. Palmitoylethanolamide for the treatment of pain: pharmacokinetics, safety and efficacy. *Br. J. Clin. Pharmacol.* 932–942 (2016).

Garau, G. *et al.* A metallo-β-lactamase enzyme in action: Crystal structures of the monozinc carbapenemase CphA and its complex with biapenem. *J. Mol. Biol.* **345**, 785–795 (2005).

García-Nafría, J. & Tate, C. G. Cryo-electron microscopy: Moving beyond X-ray crystal structures for drug receptors and drug development. *Annu. Rev. Pharmacol. Toxicol.* **60**, 51–71 (2020).

Garg, P. *et al.* functional outcome in a rodent model for stroke. **492**, 134–138 (2012).

Geurts, L. *et al.* Adipose tissue NAPE-PLD controls fat mass development by altering the browning process and gut microbiota. *Nat. Commun.* **6**, (2015).

Gonzalez-Aparicio, R. *et al.* The systemic administration of oleoylethanolamide exerts neuroprotection of the nigrostriatal system in experimental Parkinsonism. *Int. J. Neuropsychopharmacol.* **17**, 455–468 (2014).

Green, N. M. Avidin. *Adv. Protein Chem.* **29**, 85–133 (1975).

Hammond, C. *The Basics of Crystallography and Diffraction*. (Oxford University Press, 2008).

Hansen, H. S. Palmitoylethanolamide and other anandamide congeners. Proposed role in the diseased brain. *Exp. Neurol.* **224**, 48–55 (2010).

Hansen, H. S. Role of anorectic N-acylethanolamines in intestinal physiology and satiety control with respect to dietary fat. *Pharmacol. Res.* **86**, 18–25 (2014).

Hansen, H. S. & Diep, T. A. N-acylethanolamines, anandamide and food intake. *Biochem. Pharmacol.* **78**, 553–560 (2009).

Hellmann, H. & Mooney, S. Vitamin B6: A molecule for human health? *Molecules* **15**, 442–459 (2010).

Hoelzgen, F. *et al.* Neutralization of the anthrax toxin by antibody-mediated stapling of its membrane-penetrating loop. *Acta Crystallogr. Sect. D Struct. Biol.* **77**, 1197–1205 (2021).

Homola, J. Surface plasmon resonance sensors for detection of chemical and biological species. *Chem. Rev.* **108**, 462–493 (2008).

Howard, J. A. K. & Probert, M. R. Cutting-edge techniques used for the structural investigation of single crystals. *Science* **343**, 1098–1102 (2014).

Hua, T. *et al.* Crystal Structure of the Human Cannabinoid Receptor CB1. *Cell* **167**, 750-762.e14 (2016).

Hussain, Z., Uyama, T., Tsuboi, K. & Ueda, N. Mammalian enzymes responsible for the biosynthesis of N-acylethanolamines. *Biochim. Biophys. Acta - Mol. Cell Biol. Lipids* **1862**, 1546–1561 (2017).

Iannotti, F. A., Di Marzo, V. & Petrosino, S. Endocannabinoids and endocannabinoid-related mediators: Targets, metabolism and role in neurological disorders. *Prog. Lipid Res.* **62**, 107–128 (2016).

Iannotti, F. A. & Vitale, R. M. The endocannabinoid system and ppars: Focus on their signalling crosstalk, action and transcriptional regulation. *Cells* **10**, 1–22 (2021).

Igarashi, M. *et al.* Dietary oleic acid contributes to the regulation of food intake through the synthesis of intestinal oleoylethanolamide. *Front. Endocrinol.* **13**, 1–12 (2023).

Ikawa, M. Synthesis and Properties of Some N-Pyridoxyl-L-Amino Acids and N-(5-Phosphopyridoxyl)-L-Amino Acids. *Arch. Biochem. Biophys.* **118**, 497–500 (1967).

Iskander, M. *et al.* Transition-state analogues as inhibitors for GABA-aminotransferase. *Eur. J. Med. Chem.* **26**, 129–136 (1991).

Karplus, A. & Diederichs, K. Linking crystallographic model and data quality. *Science* **336**, 1030–1033 (2012).

Kasatkina, L. A., Rittchen, S. & Sturm, E. M. Neuroprotective and immunomodulatory action of the endocannabinoid system under neuroinflammation. *Int. J. Mol. Sci.* **22**, (2021).

Kathuria, S. *et al.* Modulation of anxiety through blockade of anandamide hydrolysis. *Nat. Med.* **9**, 76–81 (2002).

Katona, I. & Freund, T. F. Europe PMC Funders Group Multiple Functions of Endocannabinoid Signaling in the Brain. 529–558 (2014).

Kim, H. Y. & Spector, A. A. N-Docosahexaenoylethanolamine: A neurotrophic and neuroprotective metabolite of docosahexaenoic acid. *Mol. Aspects Med.* **64**, 34–44 (2018).

Kuipers, E. N. *et al.* High fat diet increases circulating endocannabinoids accompanied by increased synthesis enzymes in adipose tissue. *Front. Physiol.* **10**, 1–10 (2019).

Laleh, P. *et al.* Oleoylethanolamide increases the expression of PPAR-A and reduces appetite and body weight in obese people: A clinical trial. *Appetite* **128**, 44–49 (2018).

Lambert, D., Vandevoorde, S., Jonsson, K.-O. & Fowler, C. The Palmitoylethanolamide Family: A New Class of Anti-Inflammatory Agents ? *Curr. Med. Chem.* **9**, 663–674 (2002).

Landolfo, E., Cutuli, D., Petrosini, L. & Caltagirone, C. Effects of Palmitoylethanolamide on Neurodegenerative Diseases: A Review from Rodents to Humans. *Biomolecules* **12**, 1–17 (2022).

Leung, D., Saghatelian, A., Simon, G. M. & Cravatt, B. F. Inactivation of N-Acyl phosphatidylethanolamine phospholipase D reveals multiple mechanisms for the biosynthesis of endocannabinoids. *Biochemistry* **45**, 4720–4726 (2006).

Leuti, A. *et al.* Bioactive lipids, inflammation and chronic diseases. *Adv. Drug Deliv. Rev.* **159**, 133–169 (2020).

Li, L., Peng, X., Batliwala, M. & Bouvier, M. Crystal structures of MHC class I complexes reveal the elusive intermediate conformations explored during peptide editing. *Nat. Commun.* **14**, 5020 (2023).

Li, X. *et al.* Crystal Structure of the Human Cannabinoid Receptor CB2. *Cell* **176**, 459-467.e13 (2019).

Liu, J. *et al.* Multiple pathways involved in the biosynthesis of anandamide. *Neuropharmacology* **54**, 1–7 (2008).

Liu, Q., Tonai, T. & Ueda, N. Activation of N-acylethanolamine-releasing phospholipase D by polyamines. *Chem. Phys. Lipids* **115**, 77–84 (2002).

Luft, J. R. & DeTitta, G. T. A method to produce microseed stock for use in the crystallization of biological macromolecules. *Acta Crystallogr. Sect. D Biol. Crystallogr.* **55**, 988–993 (1999).

Lutz, B., Marsicano, G., Maldonado, R. & Hillard, C. J. The endocannabinoid system in guarding against fear, anxiety and stress. *Nat. Rev. Neurosci.* **16**, 705–718 (2015).

Maccarrone, M. Endocannabinoid signaling at the periphery: 50 years after THC. *Trends Pharmacol Sci* **35**, 277–296 (2015).

Maccarrone, M., Pauselli, R., Di Rienzo, M. & Finazzi-Agrò, A. Binding, degradation and apoptotic activity of stearoylethanolamide in rat C6 glioma cells. *Biochem. J.* **366**, 137–144 (2002).

Magotti, P. *et al.* Structure of human n-acylphosphatidylethanolamine-hydrolyzing phospholipase D: Regulation of fatty acid ethanolamide biosynthesis by bile acids. *Structure* **23**, 598–604 (2015).

Makar, S., Saha, T. & Singh, S. K. Naphthalene, a versatile platform in medicinal chemistry: Sky-high perspective. *Eur. J. Med. Chem.* **161**, 252–276 (2019).

Marchioni, C. *et al.* Recent advances in LC-MS/MS methods to determine endocannabinoids in biological samples: Application in neurodegenerative diseases. *Anal. Chim. Acta* **1044**, 12–28 (2018).

Margheritis, E. *et al.* Bile Acid Recognition by NAPE-PLD. *ACS Chem. Biol.* **11**, 2908–2914 (2016).

Marrone, M. C. *et al.* TRPV1 channels are critical brain inflammation detectors and neuropathic pain biomarkers in mice. *Nat. Commun.* **8**, (2017).

Marsicano, G. *et al.* CB1 cannabinoid receptors and on-demand defense against excitotoxicity. *Science* **302**, 84–88 (2003).

Martins, D., Tavares, I. & Morgado, C. 'hotheaded': The role of TRPV1 in brain functions. *Neuropharmacology* **85**, 151–157 (2014).

Matias, I., Belluomo, I. & Cota, D. The Fat Side of the Endocannabinoid System: Role of Endocannabinoids in the Adipocyte. *Cannabis Cannabinoid Res.* **1**, 176–185 (2016).

Mazier, W., Saucisse, N., Gatta-Cherifi, B. & Cota, D. The Endocannabinoid System: Pivotal Orchestrator of Obesity and Metabolic Disease. *Trends Endocrinol. Metab.* **26**, 524–537 (2015).

McCoy, A. J. *et al.* Phaser crystallographic software. *J. Appl. Crystallogr.* **40**, 658–674 (2007).

McPherson, A. & Gavira, J. A. Introduction to protein crystallization. *Acta Crystallogr. Sect. FStructural Biol. Commun.* **70**, 2–20 (2014).

Messerli, F. H. *et al.* Antihypertensive efficacy of hydrochlorothiazide as evaluated by ambulatory blood pressure monitoring: A meta-analysis of randomized trials. *J. Am. Coll. Cardiol.* **57**, 590–600 (2011).

Mileni, M. *et al.* Structure-guided inhibitor design for human FAAH by interspecies active site conversion. *Proc. Natl. Acad. Sci. U. S. A.* **105**, 12820–12824 (2008).

Minor, K. M. *et al.* Canine NAPEPLD-associated models of human myelin disorders. *Sci. Rep.* **8**, 1–11 (2018).

Mock, E. D., Gagestein, B. & van der Stelt, M. Anandamide and other N-acylethanolamines: A class of signaling lipids with therapeutic opportunities. *Prog. Lipid Res.* **89**, 101194 (2023).

Mock, E. D. *et al.* Structure-Activity Relationship Studies of Pyrimidine-4-Carboxamides as Inhibitors of N-Acylphosphatidylethanolamine Phospholipase D. *J. Med. Chem.* **64**, 481–515 (2021).

Montecucco, F. & Di Marzo, V. At the heart of the matter: The endocannabinoid system in cardiovascular function and dysfunction. *Trends Pharmacol. Sci.* **33**, 331–340 (2012).

Morena, M. & Hill, M. N. Buzzkill: the consequences of depleting anandamide in the hippocampus. *Neuropsychopharmacology* **44**, 1347–1348 (2019).

Morena, M. *et al.* Endogenous cannabinoid release within prefrontal-limbic pathways affects memory consolidation of emotional training. *Proc. Natl. Acad. Sci. U. S. A.* **111**, 18333–18338 (2014).

Myszka, D. G. Improving biosensor analysis. *J. Mol. Recognit.* **12**, 279–284 (1999).

Controlling reaction specificity in pyridoxal phosphate enzymes. Biochim Biophys Acta. 2011 Nov;1814(11):1407-18. doi: 10.1016/j.bbapap.2011.05.019. Epub 2011 Jun 6. PMID: 21664990; PMCID: PMC3359020.

Toney, M. D. Controlling reaction specificity in pyridoxal phosphate enzymes. *Biochim Biophys* Acta. **11**, 1407–1418 (2012).

Nagai, K. & Thøgersen, H. C. Synthesis and Sequence-Specific Proteolysis of Hybrid Proteins Produced in Escherichia Coli. *Methods Enzymol.* **153**, 461–481 (1987).

Natarajan, V., Schmid, P. C., Reddy, P. V. & Schmid, H. H. O. Catabolism of N-Acylethanolamine Phospholipids by Dog Brain Preparations. *J. Neurochem.* **42**, 1613–1619 (1984).

Nogales, E. & Scheres, S. H. W. Cryo-EM: A Unique Tool for the Visualization of Macromolecular Complexity. *Mol. Cell* **58**, 677–689 (2015).

Okamoto, Y., Morishita, J., Tsuboi, K., Tonai, T. & Ueda, N. Molecular Characterization of a Phospholipase D Generating Anandamide and Its Congeners. *J. Biol. Chem.* **279**, 5298–5305 (2004).

Okamoto, Y., Tsuboi, K. & Ueda, N. Chapter 1 Enzymatic Formation of Anandamide. *Vitam. Horm.* **81**, 1–24 (2009).

Osei-Hyiaman, D. *et al.* Endocannabinoid activation at hepatic CB1 receptors stimulates fatty acid synthesis and contributes to diet-induced obesity. *J. Clin. Invest.* **115**, 1298–1305 (2005).

O'Sullivan, S. E. Endocannabinoids and the Cardiovascular System in Health and Disease. in *Endocannabinoids* (ed. Pertwee, R. G.) 395–422 (Springer International Publishing, 2015).

O'Sullivan, S. E. An update on PPAR activation by cannabinoids. *Br. J. Pharmacol.* **173**, 1899–1910 (2016).

Oveisi, F., Gaetani, S., Eng, K. T. P. & Piomelli, D. Oleoylethanolamide inhibits food intake in free-feeding rats after oral administration. *Pharmacol. Res.* **49**, 461–466 (2004).

Pacher, P., Bátkai, S. & Kunos, G. The Endocannabinoid System as an Emerging Target of Pharmacotherapy. *Pharmacol. Rev.* **58**, 389–462 (2006).

Parra, M., Stahl, S. & Hellmann, H. Vitamin B6 and its role in cell metabolism and physiology. *Cells* **7**, (2018).

Patching, S. G. Surface plasmon resonance spectroscopy for characterisation of membrane protein-ligand interactions and its potential for drug discovery. *Biochim. Biophys. Acta - Biomembr.* **1838**, 43–55 (2014).

Pérez-Martín, E. *et al.* Oleoylethanolamide Delays the Dysfunction and Death of Purkinje Cells and Ameliorates Behavioral Defects in a Mouse Model of Cerebellar Neurodegeneration. *Neurotherapeutics* **18**, 1748–1767 (2021).

Petersen, G., Chapman, K. D. & Hansen, H. S. A rapid phospholipase D assay using zirconium precipitation of anionic substrate phospholipids: Application to N-acylethanolamine formation in vitro. *J. Lipid Res.* **41**, 1532–1538 (2000).

Petersen, G. & Hansen, H. S. N-acylphosphatidylethanolamine-hydrolysing phospholipase D lacks the ability to transphosphatidylate. *FEBS Lett.* **455**, 41–44 (1999).

Pettinati, I., Brem, J., Lee, S. Y., McHugh, P. J. & Schofield, C. J. The Chemical Biology of Human Metallo-β-Lactamase Fold Proteins. *Trends Biochem. Sci.* **41**, 338–355 (2016).

Piazza, P. V., Cota, D. & Marsicano, G. The CB1 Receptor as the Cornerstone of Exostasis. *Neuron* **93**, 1252–1274 (2017).

Piomelli, D. A fatty gut feeling. *Trends Endocrinol. Metab.* **24**, 332–341 (2013).

Piomelli, D. & Tagne, A. M. Endocannabinoid-Based Therapies. *Annu. Rev. Pharmacol. Toxicol.* **62**, 483–507 (2022).

Powell, H. R. X-ray data processing. *Biosci. Rep.* **37**, 1–14 (2017).

Quinn, J. G. Modeling Taylor dispersion injections: Determination of kinetic/affinity interaction constants and diffusion coefficients in label-free biosensing. *Anal. Biochem.* **421**, 391–400 (2012).

Rakotoarivelo, V., Sihag, J. & Flamand, N. Role of the endocannabinoid system in the adipose tissue with focus on energy metabolism. *Cells* **10**, 1–28 (2021).

Rapoport, R. M. & Soleimani, M. Mechanism of Thiazide Diuretic Arterial Pressure Reduction: The Search Continues. *Front. Pharmacol.* **10**, 1–23 (2019).

Renaud, J. P. *et al.* Cryo-EM in drug discovery: Achievements, limitations and prospects. *Nat. Rev. Drug Discov.* **17**, 471–492 (2018).

Rhodes, G. *Crystallography Made Crystal Clear A Guide for Users of Macromolecular Models*. (Elsevier Inc, 2006).

Robertson, M. J., Meyerowitz, J. G. & Skiniotis, G. Drug discovery in the era of cryo-electron microscopy. *Trends Biochem. Sci.* **47**, 124–135 (2022).

Rodríguez De Fonseca, F. *et al.* An anorexic lipid mediator regulated by feeding. *Nature* **414**, 209–212 (2001).

Romano, A. *et al.* "To brain or not to brain": evaluating the possible direct effects of the satiety factor oleoylethanolamide in the central nervous system. *Front. Endocrinol.* **14**, 1–12 (2023).

Rudd, E. A., Cunningham, W. C. & Thanassi, J. W. Coenzyme-Substrate Adducts as Inhibitors of Mouse Liver 3, 4-Dihydroxyphenylalanine Decarboxylase. *J. Med. Chem.* **22**, 233–237 (1979).

Rupp, B. Biomolecular Crystallography. (Garland Science, 2009).

Scapin, G., Potter, C. S. & Carragher, B. CryoEM for small molecules discovery, design, understanding and application. *Cell Chem Biol* **15**, 1318–1325 (2018).

Schasfoort, R. B. M. *Handbook of Surface Plasmon Resonance.* (Royal Society of Chemistry, 2017).

Schmid, H. H. O., Schmid, P. C. & Natarajan, V. N-Acylated glycerophospholipids and their derivatives. *Prog. Lipid Res.* **29**, 1–43 (1990).

Schmid, P. C., Reddy, P. V., Natarajan, V. & Schmid, H. H. Metabolism of N-acylethanolamine phospholipids by a mammalian phosphodiesterase of the phospholipase D type. *J. Biol. Chem.* **258**, 9302–9306 (1983).

Schmid, P. C., Zuzarte-Augustin, M. L. & Schmid, H. H. O. Properties of rat liver N-acylethanolamine amidohydrolase. *J. Biol. Chem.* **260**, 14145–14149 (1985).

Schwartz, G. J. *et al.* The Lipid Messenger OEA Links Dietary Fat Intake to Satiety. *Cell Metab.* **8**, 281–288 (2008).

Seddon, A. M., Curnow, P. & Booth, P. J. Membrane proteins, lipids and detergents: Not just a soap opera. *Biochim. Biophys. Acta - Biomembr.* **1666**, 105–117 (2004).

Simon, G. M. & Cravatt, B. F. Characterization of mice lacking candidate N-acyl ethanolamine biosynthetic enzymes provides evidence for multiple pathways that contribute to endocannabinoid production in vivo. *Mol. Biosyst.* **6**, 1411–1418 (2010).

Stanley, C. P., Hind, W. H., Tufarelli, C. & O'Sullivan, S. E. The endocannabinoid anandamide causes endothelium-dependent vasorelaxation in human mesenteric arteries. *Pharmacol. Res.* **113**, 356–363 (2016).

Stuckey, J. A. & Dixon, J. E. Crystal structure of a phospholipase D family member. *Nat. Struct. Biol.* **6**, 278–284 (1999).

Stura, E. A. & Wilson, I. A. Analytical and production seeding techniques. *Methods* **1**, 38–49 (1990).

Suardíaz, M., Estivill-Torrús, G., Goicoechea, C., Bilbao, A. & Rodríguez de Fonseca, F. Analgesic properties of oleoylethanolamide (OEA) in visceral and inflammatory pain. *Pain* **133**, 99–110 (2007).

Suchard, M. A. *et al.* Comprehensive comparative effectiveness and safety of first-line antihypertensive drug classes: a systematic, multinational, large-scale analysis. *Lancet* **394**, 1816–1826 (2019).

Sugiura, T. *et al.* Enzymatic synthesis of anandamide, an endogenous cannabinoid receptor ligand, through N-Acylphosphatidylethanolamine pathway in testis: Involvement of Ca2+-dependent transacylase and phosphodiesterase activities. *Biochem. Biophys. Res. Commun.* **218**, 113–117 (1996).

Terrazzino, S. *et al.* Stearoylethanolamide exerts anorexic effects in mice via downregulation of liver stearoyl-coenzyme A desaturase-1 mRNA expression. *FASEB J.* **18**, 1580–1582 (2004).

Tóth, A., Blumberg, P. M. & Boczán, J. Chapter 15 Anandamide and the Vanilloid Receptor (TRPV1). *Vitam. Horm.* **81**, 389–419 (2009).

Tsuboi, K. *et al.* Biosynthetic Pathways of Bioactive N-Acylethanolamines in Brain. *CNS Neurol. Disord. - Drug Targets* **12**, 7–16 (2013).

Tsuboi, K. *et al.* Enzymatic formation of N-acylethanolamines from N-acylethanolamine plasmalogen through N-acylphosphatidylethanolamine-hydrolyzing phospholipase D-dependent and -independent pathways. *Biochim. Biophys. Acta - Mol. Cell Biol. Lipids* **1811**, 565–577 (2011).

Tsuboi, K. *et al.* Molecular characterization of N-acylethanolamine-hydrolyzing acid amidase, a novel member of the choloylglycine hydrolase family with structural and functional similarity to acid ceramidase. *J. Biol. Chem.* **280**, 11082–11092 (2005).

Turcotte, C., Chouinard, F., Lefebvre, J. S. & Flamand, N. Regulation of inflammation by cannabinoids, the endocannabinoids 2-arachidonoyl-glycerol and arachidonoyl-ethanolamide, and their metabolites. *J. Leukoc. Biol.* **97**, 1049–1070 (2015).

Turnbull, A. P. & Emsley, P. Studying Protein-Ligand Interactions Using X-Ray Crystallography. *Methods Mol Biol.* **1008**, 457-77 (2013).

Ueda, N., Liu, Q. & Yamanaka, K. Marked activation of the N-acylphosphatidylethanolamine-hydrolyzing phosphodiesterase by divalent cations. *Biochim. Biophys. Acta - Mol. Cell Biol. Lipids* **1532**, 121–127 (2001).

Ueda, N., Tsuboi, K. & Uyama, T. Enzymological studies on the biosynthesis of N-acylethanolamines. *Biochim. Biophys. Acta - Mol. Cell Biol. Lipids* **1801**, 1274–1285 (2010).

Ueda, N., Tsuboi, K. & Uyama, T. Metabolism of endocannabinoids and related N-acylethanolamines: Canonical and alternative pathways. *FEBS J.* **280**, 1874–1894 (2013).

Van Der Stelt, M. *et al.* Exogenous anandamide protects rat brain against acute neuronal injury in vivo. *J. Neurosci.* **21**, 8765–8771 (2001).

Van Der Stelt, M. *et al.* Anandamide acts as an intracellular messenger amplifying Ca2+ influx via TRPV1 channels. *EMBO J.* **24**, 3026–3037 (2005).

Wang, J. *et al.* Functional analysis of the purified anandamide-generating phospholipase D as a member of the metallo-β-lactamase family. *J. Biol. Chem.* **281**, 12325–12335 (2006).

Wang, X., Miyares, R. L. & Ahern, G. P. Oleoylethanolamide excites vagal sensory neurones induces visceral pain and reduces short-term food intake in mice via capsaicin receptor TRPV1. *J. Physiol.* **564**, 541–547 (2005).

Wardlaw, J. M., Smith, C. & Dichgans, M. Small vessel disease: mechanisms and clinical implications. *Lancet Neurol.* **18**, 684–696 (2019).

Wienen-Schmidt, B., Oebbeke, M., Ngo, K., Heine, A. & Klebe, G. Two Methods, One Goal: Structural Differences between Cocrystallization and

Crystal Soaking to Discover Ligand Binding Poses. *ChemMedChem* **16**, 292–300 (2021).

Williams, C. M. & Kirkham, T. C. Anandamide induces overeating: Mediation by central cannabinoid (CB1) receptors. *Psychopharmacology (Berl).* **143**, 315–317 (1999).

Xing, C. *et al.* Cryo-EM Structure of the Human Cannabinoid Receptor CB2-Gi Signaling Complex. *Cell* **180**, 645-654.e13 (2020).

Zarrow, A. J. E. *et al.* Small Molecule Activation of NAPE-PLD Enhances Efferocytosis by Macrophages. *ACS Chem. Biol.* **18**, 1891–1904 (2023).

Zheng, H., Hou, J., Zimmerman, M. D., Wlodawer, A. & Minor, W. The future of crystallography in drug discovery. *Expert Opin. Drug Discov.* **9**, 125–137 (2014).

Zhou, J. *et al.* Structure-Activity Relationship Studies of α-Ketoamides as Inhibitors of the Phospholipase A and Acyltransferase Enzyme Family. *J. Med. Chem.* **63**, 9340–9359 (2020).

Zhou, J. *et al.* Activity-Based Protein Profiling Identifies α-Ketoamides as Inhibitors for Phospholipase A2 Group XVI. *ACS Chem. Biol.* **14**, 164–169 (2019).

Zygmunt, P. M. *et al.* Vanilloid receptors on sensory nerves mediate the vasodilator action of anandamide. *Nature* **400**, 452–457 (1999).